

Modeling and Control of an Offshore Wind Turbine with Hydraulic Drivetrain and Regenerative Power System

Rens Daan Windeij

Master of Science Thesis

Modeling and Control of an Offshore Wind Turbine with Hydraulic Drivetrain and Regenerative Power System

MASTER OF SCIENCE THESIS

For the degree of Master of Science in Systems and Control at Delft
University of Technology

Rens Daan Windeij

May 13, 2019

Faculty of Mechanical, Maritime and Materials Engineering (3mE) · Delft University of
Technology



The work in this thesis was supported by Delft Offshore Turbine. Their cooperation is hereby gratefully acknowledged.



Copyright © Delft Center for Systems and Control (DCSC)
All rights reserved.



DELFT UNIVERSITY OF TECHNOLOGY
DEPARTMENT OF
DELFT CENTER FOR SYSTEMS AND CONTROL (DCSC)

The undersigned hereby certify that they have read and recommend to the Faculty of Mechanical, Maritime and Materials Engineering (3mE) for acceptance a thesis entitled

MODELING AND CONTROL OF AN OFFSHORE WIND TURBINE WITH
HYDRAULIC DRIVETRAIN AND REGENERATIVE POWER SYSTEM

by

RENS DAAN WINDEIJ

in partial fulfillment of the requirements for the degree of
MASTER OF SCIENCE SYSTEMS AND CONTROL

Dated: May 13, 2019

Supervisor(s):

ir. S.P. Mulders

prof.dr.ir. J.W. van Wingerden

Reader(s):

dr.ir. R. Delfos

ir. T. van Dijk



Abstract

Climate change is an inevitable fact and governments worldwide have started to recognize this by expanding the contribution of renewable energy sources to our global energy production. Wind energy is currently one of the most attractive solutions for the transition to a more sustainable energy future. Since wind energy is not the only competitor in this journey towards a greener earth, reduction of the Levelized Cost of Energy (LCoE) is an important indicator to stay competitive. The wind industry pursues this goal primarily by increasing the size of wind turbines. As a result, the increased rotor size also comes with a significant increase in static and fatigue loading on the wind turbine's rotating and fixed structure.

To address this problem, the industry continues to investigate the application of alternative and economically more viable drivetrain technologies. An interesting development highlights that the implementation of robust compact hydraulic wind turbine drivetrains presents such an alternative. Hydraulic transmission systems are typically employed in high-load systems and form an excellent opportunity for application in multi-megawatt turbines. The Delft Offshore Turbine (DOT) is a hydraulic wind turbine concept which replaces conventional drivetrain components with more robust hydraulic components. It substitutes the conventional power-train inside the nacelle with a single seawater pump. Pressurized seawater is directed through the high-pressure discharge line to a combined Pelton turbine, connected to an electrical generator on a central multi-megawatt electricity generation platform.

Moreover, the low-pressure feed line, directing seawater to the seawater pump, also has to maintain a certain pressure to prevent cavitation in the pump cylinders. This requires energy, which forms an issue since the availability of electrical energy is not self-evident on offshore locations. The goal of the DOT concept is to be completely self-sustainable and independent of external power sources. One solution for this problem is the extraction of hydraulic energy from the pressurized seawater inside the high-pressure discharge line before it is harvested by the Pelton turbine. This mechanism is referred to as the turbine's Regenerative Power System (RPS), and adds up to the challenge of hydraulic turbine control.

This thesis presents the modeling, control design and control evaluation for this intermediate version of the DOT concept. Besides rotor speed control, also the feed line pressure and the regenerative power system have to be regulated. Decentralized gain scheduled SISO controllers are employed and evaluated in below-rated conditions. Using off-the-shelf components, it is shown that the overall drivetrain efficiency and controllability are increased for operation at maximum rotor torque in the below-rated (partial load) operational region.

Contents

Acknowledgements	v
Table of Symbols	vii
1 Introduction	1
1-1 State-of-the-art	2
1-2 Alternatives	4
1-2-1 Bendix SWT-3	4
1-2-2 Orbital2 Ltd.	5
1-2-3 WinDrive	5
1-2-4 ChapDrive AS	6
1-2-5 Artemis Intelligent Power	6
1-3 Delft Offshore Turbine	7
1-3-1 In depth description of the DOT drivetrain	9
1-4 Control problem	10
1-5 Related research on hydraulic drivetrain control	11
1-6 Problem Statement & Objectives	13
1-7 Report Structure	14
2 Drivetrain Modeling	15
2-1 Drivetrain component specification	16
2-2 Rotor model	18
2-3 Hydraulic pump and motor	22
2-3-1 Rotor pump	22
2-3-2 Internal water motor	25
2-3-3 Pre-pressure pump	25
2-4 Modeling of Fluid Dynamics in Hydraulic Pipe Lines	28
2-5 Spear Valve Modeling	33
2-6 Combined Drivetrain and Component Implementation	35
2-6-1 Simscape Component Implementation	35
2-6-2 Defining model inputs and outputs	38
3 Control Strategy & Design	39
3-1 Control of Conventional Wind Turbines	40
3-2 Optimal Pressure Control Strategy	43
3-2-1 Power generation of the Regenerative Power System	44
3-2-2 Drivetrain Efficiency	47
3-3 Future Improvements	49
3-3-1 Decreasing transmission ratio between rotor and rotor pump	49
3-3-2 Increased volumetric displacement of the water motor	49
3-4 Control strategy and specifications	51
3-5 System linearization	52
3-6 Rotor stall stability analysis	54

3-6-1	The effect of incorporating drivetrain dynamics	56
3-7	Relative Gain Array analysis	59
3-8	SISO Control Design using Interpolated Gain Scheduling	62
3-8-1	Operation point specification	64
3-8-2	Controller synthesis	64
3-8-3	Modulus margin	67
3-8-4	Gain scheduling with linear interpolation	69
4	Control Results & Evaluation	71
4-1	Time domain step response	72
4-1-1	Results scenario A	72
4-1-2	Results scenario B	75
4-2	Time domain wind simulation	77
4-2-1	Actuator limits	79
5	Conclusions & Recommendations	81
5-1	Conclusion	81
5-2	Recommendations	83
A	Appendix A	85
A-1	Particle Swarm Optimization	85
A-2	Simplified SimScape model for Simulink	87
	Glossary	89
	List of Acronyms	89
	Bibliography	91



Acknowledgements

First and foremost, I would like to express my sincere gratitude to my supervisor, ir Sebastiaan P. Mulders, for his continuous support and guidance during all the time of writing this thesis. Furthermore, his friendly attitude, engagement and insightful comments encouraged and motivated me throughout the whole learning process of this master thesis.

Secondly, I would like to thank Prof. dr. ir. Jan-Willem van Wingerden for his guidance and open attitude throughout the period in which I wrote this thesis.

My sincere thanks also goes to Tobias van Dijk, and thereby Delft Offshore Turbine b.v., who provided me with the opportunity to join their team as an intern. Their cooperation is hereby gratefully acknowledged.

I thank my study mates for all the fun we had and the cozy coffee breaks. I am grateful for having shared this graduating experience together with you guys.

Last but not least, I would like to thank my family: my girlfriend for her continued support and encouragement and my parents for always supporting me in everything I have accomplished so far.

Delft, University of Technology
May 13, 2019

Rens Daan Windeij



Table of Symbols

Description	Accent
Time derivative	$\dot{(\cdot)}$
Value at operation point of linearization	(\cdot)
Deviation from linearization point	$\hat{(\cdot)}$
Estimated value or function	$\hat{(\cdot)}$

Description	Symbol	Value	Unit
Density	ρ	-	kg m ⁻³
Density of air	ρ_a	1.225	kg m ⁻³
Density of water	ρ_w	998	kg m ⁻³
Kinematic viscosity seawater (10 °C)	ν	1.3063	mm ² s ⁻¹
Dynamic viscosity seawater (10 °C)	μ	1.3059	mPa s
Gravitational constant	g	9.8	m s ⁻²
mass (general)	m	-	-
Bulk modulus of seawater	K_{bulk}	$2.29 \cdot 10^9$	Pa
Fluid velocity entry control volume	V_1	-	m s ⁻¹
Fluid velocity exit control volume	V_2	-	m s ⁻¹
Pressure entry control volume	p_1	-	Pa
Pressure exit control volume	p_2	-	Pa
Elevation entry entry control volume	z_1	-	m
Elevation entry exit control volume	z_2	-	m
Spear valve	S_i	-	-
Spear valve nominal nozzle diameter	D_{nz}	26	mm
Spear valve coning angle of spear	α	50	deg
Spear valve discharge coefficient	C_d	0.98	-
Spear valve opening area	A_{nz}	0 - 530.9	mm ²
Spear valve 1 spear position	s_1	0 - 27.9	mm
Spear valve 2 spear position	s_2	0 - 27.9	mm
Spear valve 3 spear position	s_3	0 - 27.9	mm
Spear valve 1 reference spear position	$s_{1,\text{ref}}$	0 - 27.9	mm
Spear valve 2 reference spear position	$s_{2,\text{ref}}$	0 - 27.9	mm
Spear valve 3 reference spear position	$s_{3,\text{ref}}$	0 - 27.9	mm

Spear valve actuator time constant	t_s	1.69	s
Spear valve maximum spear position	s_{\max}	27.9	mm
Spear valve flow	Q_{nz}	-	$\text{m}^3 \text{s}^{-1}$
General pump rotational speed	ω_p	-	-
General pump volumetric displacement	V_p	-	-
General pump flow	Q_p	-	-
General pump pressure differential	Δp_p	-	-
General pump mechanical efficiency	$\eta_{m,p}$	-	-
General pump volumetric efficiency	$\eta_{v,p}$	-	-
General pump slip coefficient	$C_{s,p}$	-	-
General pump slip flow	$Q_{s,p}$	-	-
Rotor pump	P_r	-	-
Rotor pump pressure differential	Δp_r	0 - 95	bar
Rotor pump mechanical efficiency	$\eta_{m,r}$	0.5 - 0.81	-
Rotor pump volumetric efficiency	$\eta_{v,r}$	0.93	-
Rotor pump volumetric displacement	V_r	2.3	L rev^{-1}
Rotor torque	τ_r	-	-
Rotor inertia	J_r	$6.6 \cdot 10^5$	kg m^2
Rotor radius	R	22	m
Rotor swept area	A_r	1521	m^2
Rotor rotational speed	ω_r	0 - 31	rev min^{-1}
Rotor power coefficient	C_p	0 - 0.48	-
Rotor max. power coefficient	$C_{p,\max}$	0.48	-
Rotor torque coefficient	C_τ	$0 - 7.2 \cdot 10^{-2}$	-
Rotor max. torque coefficient	$C_{\tau,\max}$	$7.2 \cdot 10^{-2}$	-
Rotor tip-speed ratio	λ	-	-
Rotor blade pitch angle	β	-	-
Rotor blade fine pitch angle	β_0	-2	degrees
Rotor thrust force	T	-	-
Rotor power extraction	P	-	-
Wind power	P_{wind}	-	-
Pre-pressure pump	P_{pp}	-	-
Pre-pressure pump mechanical efficiency	$\eta_{m,pp}$	1	-
Pre-pressure pump volumetric efficiency	$\eta_{v,pp}$	function	-
Pre-pressure pump flow (single pump)	Q_{pp}	0 - 500	l min^{-1}
Pre-pressure pump rotational speed	ω_{pp}	0 - 3600	rev min^{-1}
Pre-pressure pump max. rotational speed	ω_{\max}	3600	rev min^{-1}
Pre-pressure pump discharge pressure	p_{pp}	0 - 20	bar
Pre-pressure pump volumetric displacement	V_{pp}	0.1399	L rev^{-1}
Internal water motor	M_1	-	-
Internal water motor mechanical efficiency	$\eta_{m,M1}$	0.90	-
Internal water motor volumetric efficiency	$\eta_{v,M1}$	0.95	-
Internal water motor torque	τ_{M1}	0 - 250	Nm
Internal water motor rotational speed	ω_{M1}	1540-1570	rev min^{-1}
Internal water motor volumetric displacement	V_{pp}	0.225	L rev^{-1}
System torque	τ_{sys}	-	-
Wind speed upstream of rotor	U	-	-
Wind speed at rotor	U_r	-	-
Wind speed downstream of rotor	U_e	-	-

Hydraulic pipe line diameter	D_p	0.1	m
Hydraulic pipe line surface roughness	ϵ	$45 \cdot 10^{-6}$	m
Hydraulic pipe segment length	$L_{(e)}$	15	m
Hydraulic pipe segment control volume	$V_{(e)}$	0.118	m^3
Hydraulic pipe segment entry flow	$Q_{(e),1}$	-	$\text{m}^3 \text{s}^{-1}$
Hydraulic pipe segment exit flow	$Q_{(e),2}$	-	$\text{m}^3 \text{s}^{-1}$
Hydraulic pipe segment net flow	$Q_{(e),C}$	-	$\text{m}^3 \text{s}^{-1}$
Hydraulic pipe segment pressure diff.	$\Delta p_{(e)}$	-	Pa
Hydraulic pipe segment entry pressure	$p_{(e),1}$	-	Pa
Hydraulic pipe segment exit pressure	$p_{(e),2}$	-	Pa
Hydraulic pipe segment accumulated pressure	$p_{(e),C}$	-	Pa
Hydraulic pipe segment resistance	$R_{(e)}$	-	Pa s m^{-3}
Hydraulic pipe segment inductance	$I_{(e)}$	-	kg m^{-4}
Hydraulic pipe segment capacitance	$C_{(e)}$	-	$\text{m}^3 \text{Pa}^{-1}$
Hydraulic pipe segment Darcy friction factor	f_f	-	-
Hydraulic pipe segment shape factor	K_s	-	-
Reynolds number	Re	-	-
Vector with estimation coefficients	\vec{a}	-	-
Vector with estimation coefficients	\vec{b}	-	-
Volumetric displacement Janus	$V_{d,J}$	0.19	L rev^{-1}
Volumetric displacement pre-pressure pump	$V_{d,P}$	1.45	L rev^{-1}



Chapter 1

Introduction

This chapter introduces the subject of, and motivation for this thesis. Section 1-1 presents the state-of-the-art and introduces the reader to the difficulties and challenges that the wind industry currently faces. A brief overview of alternative technologies across history are explained in Section 1-2. The main subject of this thesis, the Delft Offshore Turbine (DOT), is introduced and explained in further detail in Section 1-3. The control problem as foundation of this thesis is presented in Section 1-4. Related research on hydraulic drivetrain control for wind turbines is described in Section 1-5. The actual problem statements and objectives for this master thesis are outlined in Section 1-6, followed by the further structure of this report in Section 1-7.

1-1: State-of-the-art	2
1-2: Alternatives	4
1-3: Delft Offshore Turbine	7
1-4: Control problem	10
1-5: Related research on hydraulic drivetrain control	11
1-6: Problem Statement & Objectives	13
1-7: Report Structure	14

1-1 State-of-the-art

Horizontal-axis wind turbines (HAWTs) are currently characterized by high installation and maintenance costs [1][2]. The costs are largely determined by the method of wind energy conversion to electricity. Conventional wind turbines convert wind power to rotating mechanical power in the form of torque and rotation speed of the rotor. Conventional offshore wind turbines generally employ a gearbox to lower the torque and increase the rotation speed, suited for the electrical generator in the nacelle. Before the generated electricity can be fed to the grid, voltage and frequency have to be regulated by power electronics [3].

Climate change is an inevitable fact, and governments worldwide have started to recognize this by expanding the contribution of renewable energy sources to our global energy production. Both the rapidly-growing demand for sustainable power production and the urge to reduce the Levelized Cost of Energy (LCoE) lead to a notable trend of offshore wind turbines becoming larger over the past few decades. Figure 1-2 illustrates that this trend is forecasted to continue in the foreseeable future.

However, Burton et al. [4] states that rotation speed of the rotor decreases asymptotically and torque increases exponentially with increasing blade length and power ratings. Scaling up offshore wind turbine drivetrains will therefore inevitably result in design challenges of

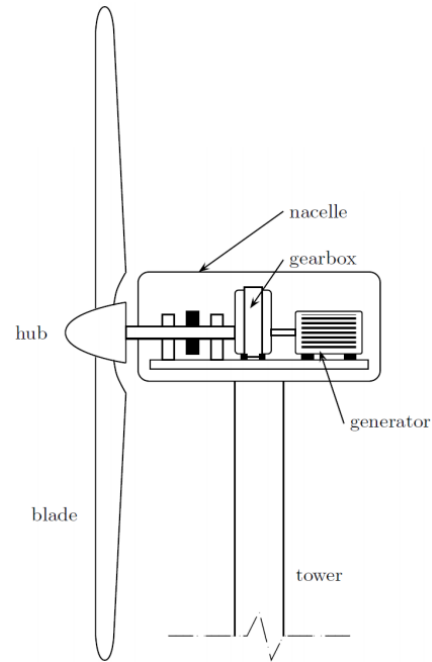


Figure 1-1: Simplified cross-section of a conventional wind turbine.

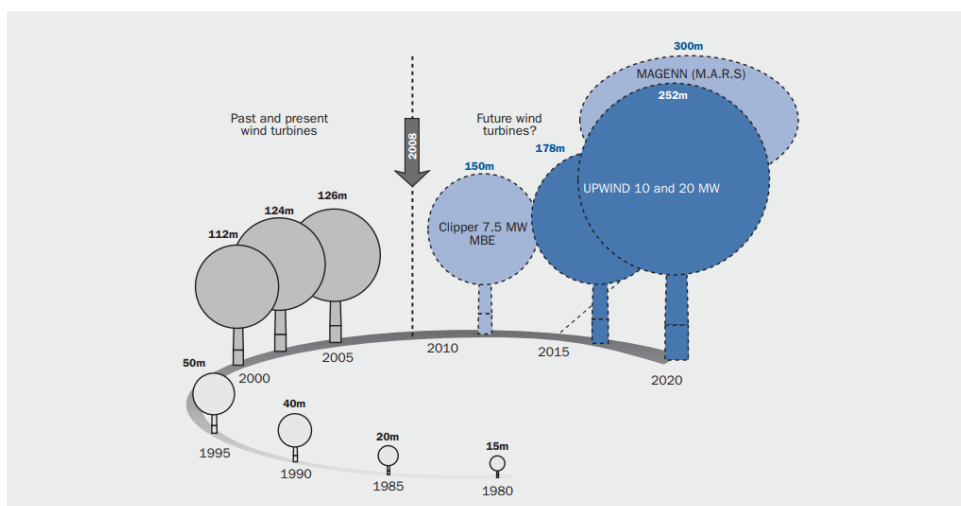


Figure 1-2: An overview of the history of the size of wind turbines as well as the forecast for the foreseeable future [54].

the high-load subsystems [5]. Increased loads such as vibrations and asymmetric loading predominantly affect components inside the nacelle such as the generator, gearbox and bearings. Since these components are heavy, replacement or repair after premature failing of these components becomes a costly and challenging task [1][2], especially at offshore locations. Crabtree [6] shows that gearboxes both have the biggest annual failure frequency and result in the longest downtime after failure with respect to other drivetrain components. Spinato et al. [1] shows that especially gearboxes have failure rates of 3 to 5 times bigger than other components. Figure 1-3 shows the result of a failure data study based on two databases: one from the Wissenschaftliches Mess- und Evaluierungsprogramm (WMEP) and the other of the Landwirtschaftskammer (LWK). Both databases show that especially the downtimes after failure of the gearbox is significant with respect to that of other components. The LWK database shows an average of 14 days that a wind turbine is out of operation after failure of the gearbox.

Based on the aforementioned studies, it can be concluded that the gearbox is the main source of high-maintenance costs for offshore wind farms. Unplanned maintenance and component replacement, a hassle at offshore locations, directly contribute to the high turbine life-cycle costs. J.K. Lee et al. [7] shows that almost half of all maintenance costs for offshore wind turbines are attributed to the gearbox and generator. However, turbine unavailability due to failure also results in a lower annual energy production and indirectly increases the turbine operational costs, thus the LCoE.

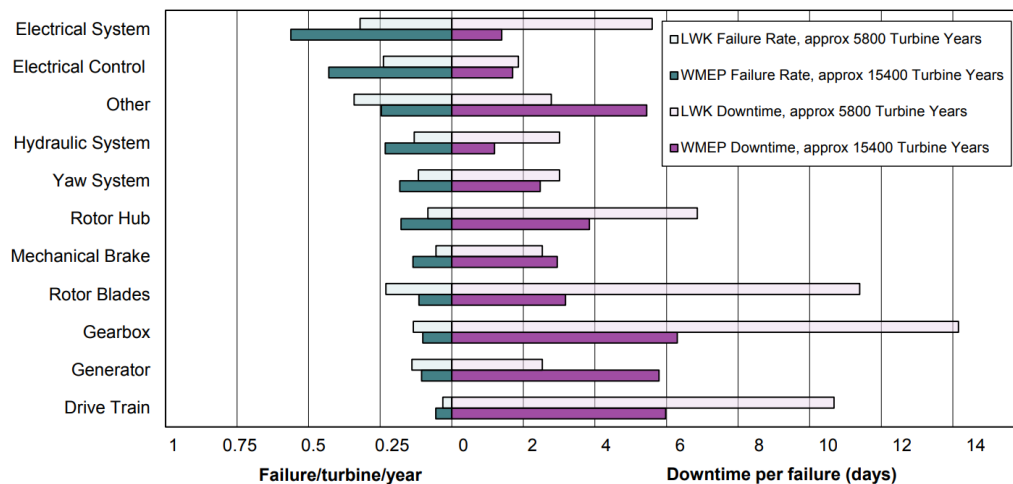


Figure 1-3: Breakdown of failure rates and downtimes per failure for different components of a conventional wind turbine drivetrains [75]

Furthermore, drivetrain components that are installed in nacelles of conventional wind turbines are heavy and add up to the total nacelle mass. The support structure (tower) and foundation have to be designed such that it can carry this weight for the entire expected lifetime, which consequently leads to extra material and weight of the tower construction and foundation [8].

The demand to improve overall performance and durability of a wind turbine to decrease the LCoE, forces many research fields to innovate towards lighter and more reliable alternatives. This allows for continuation of the trend of increasing wind turbine sizes, making wind energy a more sustainable alternative to traditional oil-based energy production.

1-2 Alternatives

An alternative technology to the conventional geared drivetrain set-up, is the direct drive technology [9][10]. This technology omits the use of a gearbox by direct coupling of the electrical generator to the rotor shaft [2]. In contrast to what one might expect, production costs cannot be reduced this way because of the more complex generator that is required [11]. Mass reduction and increase of reliability became of increased importance as the increasing rotor sizes led to increasing loads working on drivetrain component. As a consequence, the direct drive technology became too heavy to implement at offshore sites and was only applied at onshore locations. Recently however, Siemens has shown regained interest in the direct drive technology for offshore wind turbines [12].

A wide variety of industries apply compact hydraulic transmission systems in their high-load systems. Hydraulics have the advantage of high power-to-weight ratios [13], so the application of hydraulic transmissions in multi-megawatt wind turbine drivetrains could be an interesting opportunity. A hydraulic pump could convert rotational energy from the rotor to hydraulic energy in the form of pressurized fluid. The conversion from hydraulic energy back to rotational energy could be achieved by using a hydraulic motor [14]. Besides their characteristic higher power density, application of hydraulic transmission systems can decrease and increase drivetrain stiffness and damping, respectively, which might reduce the impact caused by fluctuations of the wind [15].

The idea of implementing hydraulic transmission systems as a substitute for mechanical gearboxes however, is not particularly new. Various initiatives attempted to implement different hydraulic transmission concepts in wind turbine drivetrains over the past couple decades.

1-2-1 Bendix SWT-3

One of the earliest attempts was the result of a privately funded experimental joint venture between the Bendix Corporation and the Southern California Edison (SCE) Company. The company developed the SWT-3 wind turbine between the years 1976 and 1980 [16]. The hybrid SWT-3 concept had a one-stage mechanical gearbox coupled to a hydrostatic power transmission. The hydraulic set-up included 14 fixed-displacement oil pumps in the nacelle and 18 variable-displacement motors located at the tower base. The Bendix SWT-3 was rated at 3 MW and served as a proof of concept for implementing hydraulic drivetrains in wind turbines. However, the overwhelming amount of subsystems made the overall system overly complex, inefficient and unreliable. Besides this already decisive reason, the oil crisis passed, environmental awareness was already forgotten and the existence of the Bendix SWT-3 came to an end [11].



Figure 1-4: Picture of the Bendix SWT-3 in San Giorgio, CA, USA

1-2-2 Orbital2 Ltd.

As a potential solution to the oil crisis in the 1980's, the mishmash of experimental ventures was expanded with the Orkney LS1, named after the Orkney Islands in Britain where it was constructed first [17]. The 3 MW LS1 was a 2-bladed wind turbine on a concrete tower and incorporated an innovative, 2-stage variable ratio transmission. The LS1 consisted of a mechanical gearbox and an electric reaction motor, both connected to a by Hicks [18] patented Super Positioned Gear (SPG), as shown in Figure 1-5. The gearbox is connected to the input carrier of the differential and the electrical reaction motor to the sun wheel. On the right in Figure 1-5, the generator is connected to the annulus of the SPG.

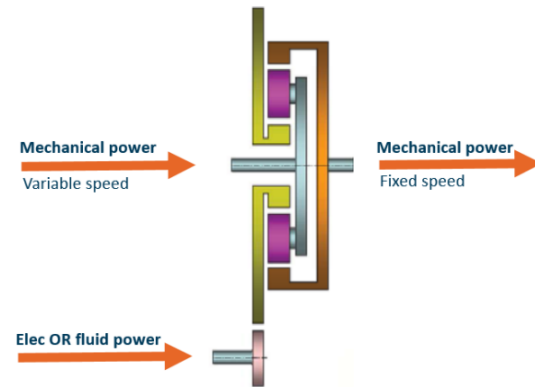


Figure 1-5: Super Positioned Gear (SPG), with input carrier in blue, sun wheel in purple and output annulus in orange [77]

The installation was designed and built by the Wind Energy Group (WEG), a joint venture of Taylor Woodrow Construction, British Aerospace and GEC Energy Systems Ltd, under contract of the UK Department of Energy. The LS1 technology resulted in the company Orbital2 Ltd. and was in 2006 licensed to Wikov Wind, a Czech wind turbine manufacturer. Wikov Wind replaced the electrical reaction motor at the sun wheel with a hydrostatic transmission in their Wikov W2000 2MW turbine.

The mechanical input power from the turbine rotor shaft is split by a parallel shaft. The largest part is passed through the mechanical gearbox to the SPG input carrier, whereas a smaller part is now passed through the hydrostatic transmission to the sun wheel. When a wind gust increases the torque on the parallel shaft, the variable hydrostatic transmission is adjusted such that the generator speed remains constant. This enables variable rotor speed while maintaining constant speed of the generator shaft. As a result, a high voltage electrically excited synchronous generator can be directly connected to the grid.

1-2-3 WinDrive

The aim on completely eliminating power electronic components by application of a synchronous generator lead to the WinDrive concept [19][20]. The WinDrive technology was developed by Voith and was based on a superimposed planetary gear drive, controlled by a hydrodynamic torque converter. When the concept was conceived in 2003, Voith partnered with DeWind. The companies developed the first 2MW prototype in 2005. The WinDrive can be considered as a variable-speed hydrodynamic gearbox that is located between the gearbox and generator. The WinDrive technology converts variable speeds of the rotor to a fixed speed of the generator input shaft. Therefore, a synchronous generator can be applied without the involvement of components as power electronic converters and step up transformers.

In 2008, several 2MW prototypes incorporating the WinDrive technology were constructed in Texas and Argentina. The WinDrive proved to be a commercial success as the wind

turbines were later installed in various wind farms in both the USA and Canada.

As in the Orbital2 method, the product is an addition to the existing main gearbox instead of a replacement. The main difference between the two concepts is the use of a hydrodynamic implementation in the Windrive concept versus the Orbital2 hydrostatic transmission.

1-2-4 ChapDrive AS

In 2004, ChapDrive AS developed an innovative drivetrain concept with the aim to drive a synchronous generator by a fixed-displacement oil pump and a variable-displacement oil motor [21][22]. The variable displacement volume of the hydraulic motor was used for controlling its rotational speed which allowed direct coupling to the synchronous generator. This concept eliminated both the need for a mechanical gearbox and for power electronic components. Although ChapDrive AS acquired funding from Statoil for constructing a 5 MW concept, the company ceased operations.

Statoil however, started cooperating with Hägglunds and modeled a drivetrain with a hydrostatic transmission consisting of a single oil pump coupled to the rotor, driving six motors located at ground level. Each motor is enabled or disabled separately, resulting in a discrete variable transmission ratio for driving a synchronous generator. By placing the oil motors at ground level, the nacelle's weight decreased significantly which allowed for down-sizing of the support structure. The downside of this concept however, is that the discrete variable transmission ratio tend to reduce transmission efficiency, particularly at low wind speeds [23][24].

1-2-5 Artemis Intelligent Power

In 2005, Artemis Ltd. developed the Digital Displacement Pump (DDP) which enabled adjustment of the pump's volumetric displacement in a digital way by enabling or disabling individual pump cylinders [25][26]. Mitsubishi acquired Artemis Intelligent Power in 2010 after which they started testing a 7 MW wind turbine, equipped with this hydraulic power drive technology in 2014, the 'SeaAngel' [27]. The SeaAngel is installed at the Hunterston, Schotland, test site in 2014, and is the largest capacity hydrostatic transmission currently built. The company claims that the heaviest component in the DDP system is just 25kg, and states that most of the parts are small enough to be carried by a single technician.

1-3 Delft Offshore Turbine

Almost none of the concepts described in the previous section made it to commercial application due to implementation of overly complex systems, resulting in inefficient and unreliable wind turbines. Aiming on the employment of synchronous generators, without involvement of power electronics, mostly directed to the development of mechanisms that allow adjustments of the hydraulic gear ratio. All described concept used oil as the hydraulic medium due to its favorable fluid properties and component compatibility, but it required them to be closed-circuit in order to minimize the risk of environmental pollution and the need for continuous supply of fresh oil. In addition to that, closed circuits often require active cooling as convection to the surroundings mostly is insufficient [28].

A novel and patented, open-circuit hydraulic wind turbine concept having seawater as the hydraulic medium is the Delft Offshore Turbine (DOT) [29], illustrated in Figure 1-6. With the aim on lowering the maintenance frequency, DOT tackles earlier mentioned failure rate problems of gearboxes and power electronics in a smart way by replacing these high-maintenance components by more robust hydraulic components. As illustrated in Figure 1-7, the DOT concept only requires a single positive displacement water pump in the nacelle, directly coupled to the turbine rotor and replaces conventional components as the gearbox, generator and converter. Seawater as hydraulic medium enables the use of an open circuit configuration. Since fresh seawater is continuously supplied to and drained from the hydraulic drivetrain, cooling measures may no longer be necessary. Diepeveen [9] states that the nacelle weight, if configured this way, will reduce with approximately two thirds of the weight of a conventional turbine, resulting in lower support structure requirements.

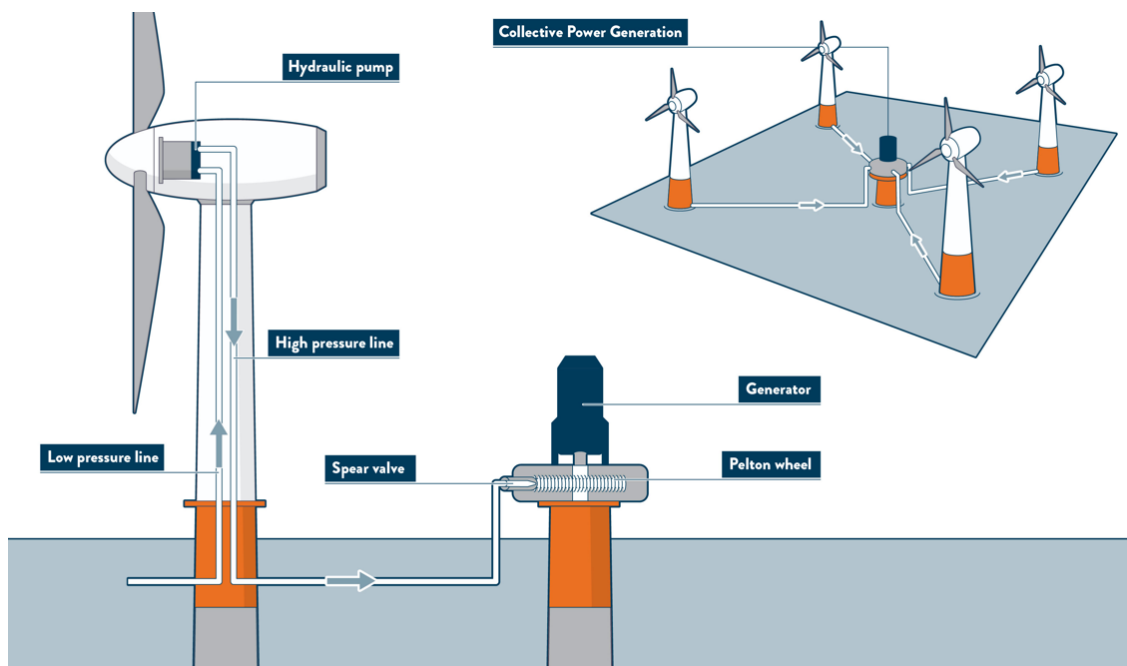


Figure 1-6: Schematic overview of the DOT configuration. The rotor is coupled to a radial piston water pump in the nacelle. The flow is converted to a high-velocity water jet by a spear valve. A Pelton turbine-generator configuration harvests the hydraulic energy and converts it into electrical energy. Multiple turbines can be connected to the central power generator platform [28].

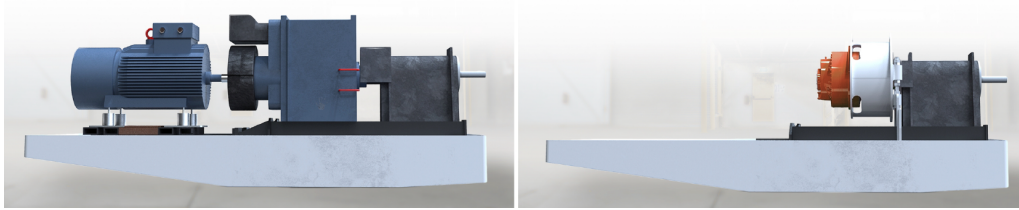


Figure 1-7: The high power-to-weight ratio of hydraulic components and the possibility to abandon power electronics from the nacelle, make the advantages of mass and space reductions in the nacelle self-evident [28].

As depicted in Figure 1-6, the more maintenance demanding components are located at foundation level where a centralized generator is driven by a Pelton turbine that captures hydraulic energy from multiple wind turbines. Using this set-up minimizes the amount of generators and improves the accessibility of maintenance demanding components. In Pusha et al. [30], it is concluded that the application of a centralized hydraulic power unit increases overall drivetrain efficiency significantly compared to applying multiple hydraulic power units for individual wind turbines. The main goal of the hydraulic DOT concept is to radically reduce weight and complexity to increase reliability and decrease maintenance costs such that the LCoE is reduced. A feasibility study of an in-field 500 kW hydraulic wind turbine based on the DOT concept (DOT500) is performed in Mulders et al. [28].

The DOT concept is based on pressurizing seawater with energy harvested from the wind. Seawater comes in through the low-pressure feed line and arrives at the hydraulic rotor pump. The displaced water flows through the high pressure line to foundation level and arrives at the centralized hydraulic power unit, as illustrated in Figure 1-6. The pressurized hydrostatic water flow is converted to a hydrodynamic water jet by means of a spear valve, a type of variable orifice nozzle. Two spear valves (e.g. derived from two separate wind turbines) mounted on a Pelton turbine are illustrated in Figure 1-8. The high-speed jets exert a force on the buckets of the Pelton turbine, causing it to start rotating since hydraulic energy is converted to mechanical rotational energy. The Pelton turbine is coupled to an electrical generator which converts the rotational energy to electrical energy which can be fed to the grid.

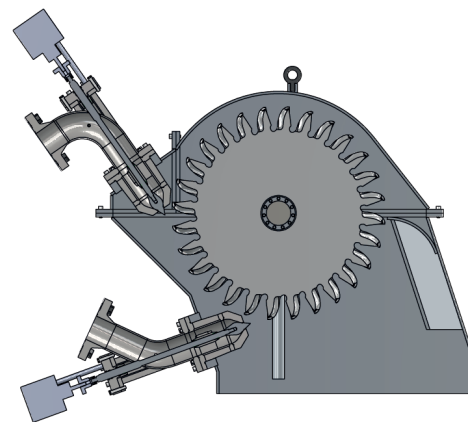


Figure 1-8: The pressurized hydrostatic water flow is converted to a hydrodynamic water jet using spear valves. The high-speed jets exert a force on the buckets of the Pelton turbine which is mechanically coupled to a generator for centralized power generation [28].

1-3-1 In depth description of the DOT drivetrain

A global overview of the DOT concept was described in the previous section. However, the DOT is designed for operation at offshore locations, which brings a couple of difficulties.

To prevent cavitation in the pump cylinders of the rotor pump, the low pressure line needs to be pressurized. Therefore, pre-pressure pumps are employed at foundation level of the tower and provide the low pressure feed line with a sufficient amount of water flow. However, these pre-pressure pumps need electrical energy in order to operate. Since the DOT concept is designed for offshore locations, availability of electrical energy is not self-evident. With the aim on self-sustainability, a Regenerative Power System (RPS) was designed by DOT. Figure 1-9a illustrates a schematic of the DOT drivetrain with the regenerative power system. The rotor pump, coupled to the rotor, is denoted by P_r , the pre-pressure pump by P_{pp} and the RPS is accentuated by the orange dashed line. The dark blue (left-hand side) and orange (right-hand side) fat lines represent the low-pressure feed line and high-pressure discharge line, respectively.

The RPS allows a small part of the pressurized water to flow back from the high pressure discharge line to the low pressure feed line. This flow drives a small water motor M_1 , coupled to an electrical generator G . The electrical energy that is produced by this generator is used for powering the pre-pressure pump. Employment of spear valve S_1 in series with water motor M_1 is used for control of the water motor speed. Spear valve S_3 leads to the Pelton wheel at the Centralized Hydro Power Unit, but is also used for control of the pressure in the discharge line, which is useful for rotor speed control.

This drivetrain eliminates the gearbox between rotor shaft and hydraulic rotor pump. The hydraulic rotor pump should therefore be able to handle low rotational speeds and high pressures. However, such a pump is not yet commercially available, so DOT is in the

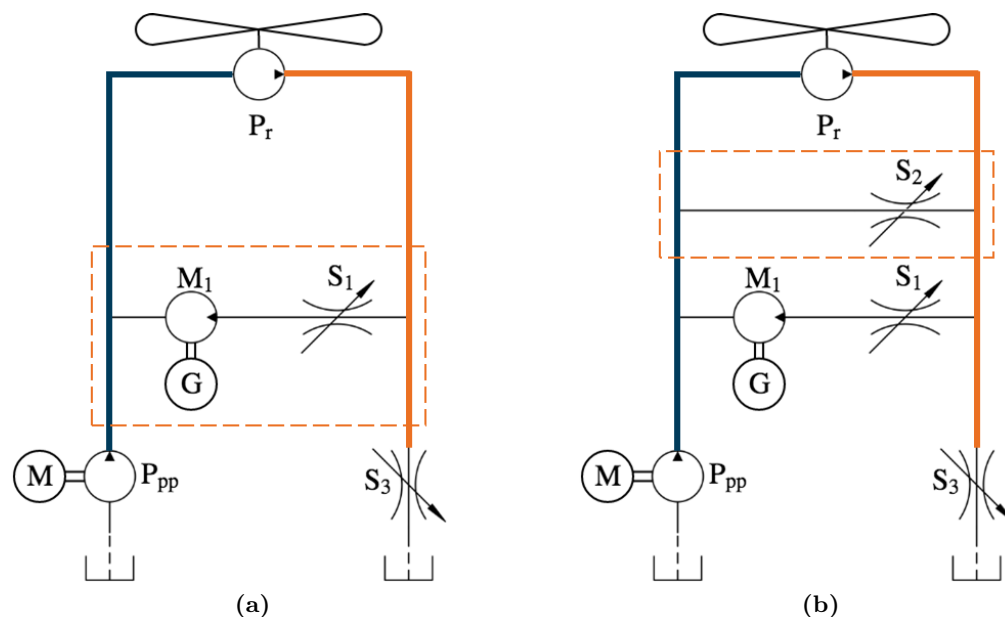


Figure 1-9: (a) Schematic of the DOT hydraulic drivetrain including the regenerative power system, accentuated by the orange dashed line; (b) Schematic of the preliminary DOT hydraulic drivetrain including the extra internal nozzle S_2 , accentuated by the orange dashed line.

process of developing such a device. As this pump is still in the design phase, a preliminary drivetrain concept, with another off-the-shelf hydraulic water pump, was designed for early offshore testing of the concept.

Figure 1-9b illustrates the preliminary drivetrain concept. The pump that is used in this concept needs higher rotational speeds (thus a gearbox) and higher flow rates of seawater. The issue here is that the pre-pressure pump cannot deliver enough flow to maintain sufficient flow in the feed line. The flow supplied by the pre-pressure pump is already supplemented by the flow going through the regenerative power system. This flow however, is limited by the rotational speed of water motor M_1 . Since the maximum attainable flow supplied by the pre-pressure pump and RPS together is not sufficient for higher rotational speeds of the rotor, another internal spear valve S_2 is added, indicated by the orange dashed line. This spear valve allows additional sea water to flow back from the high pressure discharge line the low pressure feed line, and compensates for the flow shortage.

This thesis sets out on the modeling and control design for the preliminary drivetrain concept of Figure 1-9b.

1-4 Control problem

In the below-rated (partial load) operational region of conventional wind turbines, the rotational speed of the rotor is controlled by adjusting the generator torque demand. This is possible since the generator is directly coupled to the rotor shaft. A more extensive description of conventional wind turbine control is presented in Section 3-1, the introduction to the control chapter. However, the DOT drivetrain mechanically decouples the rotor shaft of the generator shaft which makes generator torque control inconsequential for rotor speed control. The rotor speed can now only be controlled by regulating the pressure differential across the rotor pump. If this pressure differential can be controlled by actuation of the three spear valves and the pre-pressure pump (Figure 1-9b), the rotor speed can be controlled.

Mulders et al. [31] already proposed a top-level control strategy for start-up and below-rated operation of the DOT wind turbine including the regenerative power system. During start-up, spearvalve 2 and 3 are closed and the feed line is pressurized by an accumulator filled with seawater. After reaching nominal speed of the water motor M , torque can be demanded by the generator as spearvalve S_1 regulates the water motor to its nominal speed. Spear valve S_3 opens and controls the pressure in the high pressure discharge line. Since the amount of flow through the regenerative system is limited, spear valve S_2 opens to supply sufficient flow to the rotor pump.

This top-level control strategy for the below-rated operational domain will be the foundation for this thesis report. Because of the highly complex system, and the vast amount of in- and outputs to be controlled compared to conventional wind turbines, a dynamical model is derived to perform an analysis on the system coupling. This analysis results in an assessment of the feasibility for a decentralized Single-Input Single-Output (SISO) control solution, or a more advanced Multiple-Input Multiple-Output (MIMO) control algorithm for below-rated operation of the wind turbine.

1-5 Related research on hydraulic drivetrain control

Earlier research on control of the DOT wind turbine was performed by Mulders et al. [28]. Control design, implementation and evaluation of an intermediate DOT500 concept is described, based on real-world experiments with a 500 kW hydraulic prototype. The drivetrain of the considered wind turbine consists of a closed-loop oil circuit in series with an open-loop water circuit, equivalent to the high-pressure line between the rotor pump and spear valve S3 illustrated in Figure 1-1. The internal spear valves, water motor and dynamics of the low-pressure feed line were not incorporated in the model. An active spear valve and pitch controller were designed for rotor speed regulation in, respectively, the near-rated and rated operating region. For the below-rated operational domain, a passive torque control strategy was described. Due to higher complexity of the drivetrain considered in this thesis, passive torque control is expected to be no longer applicable.

Buhagiar [24] illustrates a novel variable-orifice controller implementation, simulated in a dynamic open-loop hydraulic drivetrain model of a wind turbine. In contrast to the DOT concept, a variable displacement rotor pump was employed. The goal was to maintain a fixed nozzle pressure for optimum Pelton wheel operation at synchronous generator speed. It was observed that pressure control of the open-loop hydraulic circuit presents an interesting control challenge due to the highly fluctuating wind speed dependent flow rate along with the non-linear behavior of the variable-area orifice used by the pressure controller. Two nozzle controllers were proposed. One controller only consisted of a feed-forward control strategy, utilizing a model of the orifice and spear valve as a compensator. An improvement of this controller was to include an additional feedback loop to account for any deviations from the behavior predicted by the feed-forward compensator. In this case, the orifice controller can use the compensator for the nonlinear part of the system and the feedback loop for regulating the pressure to the required value. A Monte-Carlo analysis was carried out to evaluate the controller performance for a wide range of conditions. Cost error function distributions were used to rank the controllers and a significant difference was observed between the two. It turned out that the inclusion of a feedback loop clearly resulted in a more advantageous controller when compared to a sole feed-forward implementation.

In Dolan et al. [32], performance of a gain scheduled Linear Quadratic Regulator (LQR) with feed-forward controller is investigated. The wind turbine drivetrain consisted of a hydrostatic transmission, consisting of a fixed-displacement hydraulic pump and a variable displacement hydraulic motor. A schematic of the drivetrain is illustrated in Figure 1-10. By varying the relative displacement of the hydraulic components, any desired transmission ratio can be attained within a certain predefined boundary which is dependent upon the relative sizes and physical limitations of the hardware. Using this strategy, the pressure differential across the pump is controlled such that maximum rotor efficiency is assured in the below-rated operational domain. The controller has been verified through simulation, and has shown a satisfactory

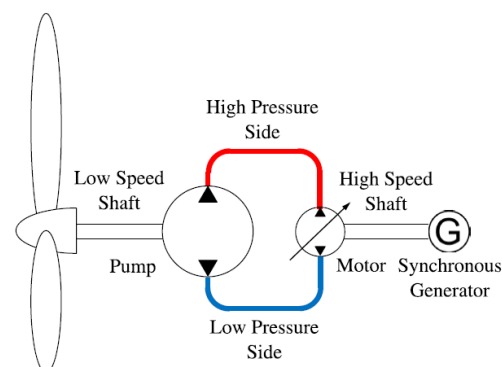


Figure 1-10: Schematic of the hydraulic drivetrain concept, described in Dolan et al. [32].

performance in controlling the wind turbine throughout its entire operating range.

Vaezi et al. [33], describes the development of a control system for a nonlinear model of hydraulic wind power transfer systems. The hydraulic wind power transfer system is comprised of various parts such as hydraulic pumps and motors, proportional valves, check valves and pressure relief valves. The proportional valves are used to regulate and control the hydraulic flow to manage the electric power generation. The generator rotational speed should remain constant to maintain a fixed voltage frequency. Fluctuating speed of the upstream wind causes significant disturbances on the system. It was concluded that a simple Proportional Integral (PI) controller was sufficient under low wind speed and high wind speed fluctuations. In addition to this conclusion however, it was stated that increasing the number of hydraulic components would exert more non-linearities onto the system such that a more advanced controller would be required.

Bianchi et al. [34] presents a new design methodology of gain scheduled controllers for conventional wind turbines. The proposed methodology is intended to deal with multi-variable and high-order models as those produced by high-fidelity aeroelastic simulators. The methodology consists in interpolating the local H_∞ -controller outputs and does not require an uniform state definition either of the local controllers or of the linear models. It is assumed that the only available information about the nonlinear system is a set of linear models describing its local behavior at a set of operating points. This allows the design of each controller independently, an essential point in cases of high order models, and then interpolated to construct a gain scheduled controller. In general, interpolation is a fairly simple solution in case of SISO problems or fixed structure controllers. This is due to the fact that only certain fixed parameters are interpolated (fixed structure of controller parameters/states). However, in more general cases where the set of controllers have been designed independently and they are MIMO, the implementation of the parameter interpolation is not as simple. The option of interpolating (unstructured) controller state-space realisations is not available since the non-uniform definition of the controller states may cause unexpected results. A possible solution in this case is the interpolation of the outputs or the inputs of the controllers.

Conclusion: In related research, only fluid dynamics of the discharge line between rotor pump and discharge nozzle is considered for modeling and control design. However, addition of the regenerative power system and extra internal nozzle results in a more complex drivetrain. As stated by Vaezi et al. [33], an increasing number of hydraulic components would exert more non-linearities onto the system, what could possibly ask for a more complex control strategy. A dynamical model should be used to analyze this and an analysis of the coupling between the vast amount of in- and outputs (compared to conventional wind turbines) will result in an assessment of the feasibility for a decentralized SISO control solution, or a more advanced MIMO control algorithm for below-rated operation of the wind turbine. Components that Delft Offshore Turbine currently uses could be modeled and analyzed to make an assessment on whether their performance meets the requirements for satisfactory turbine control performance.

1-6 Problem Statement & Objectives

In related research on turbine control for hydraulic wind turbine concepts, only fluid dynamics of the discharge line between rotor pump and discharge nozzle is considered for modeling and control design. However, addition of the regenerative power system and extra internal nozzle result in higher complexity of the drivetrain and therefore possibly the need for a more complex control strategy.

This thesis sets out to elaborate on dynamical modeling of a hydraulic wind turbine with fixed displacement components and a Regenerative Power System. For conventional wind turbines, turbine control in the below-rated operational region is achieved by drivetrain control (and not blade pitch control). Because the DOT drivetrain is completely different compared to conventional drivetrain set-ups, a new control strategy for the below-rated operational domain should be derived. Turbine start-up is left out of the scope for this thesis. In order to work towards a satisfactory result, several sub-goals are stated to set clear focus areas where this research can provide actual insights. The main objective for this thesis therefore is:

"Control a wind turbine with hydraulic drivetrain and regenerative power system in the below-rated operational domain."

This main objective is separated in the following sub-objectives:

1. Make a dynamical model of the DOT drivetrain.
 - (a) Analyze both static and dynamic relations of all individual drivetrain components with the literature, resulting in a set of component models.
 - (b) Combine those individual component models into one single drivetrain model. Use the off-the-shelf components that Delft Offshore Turbine b.v. currently has at its disposal;
2. Analyze the coupling between the in- and outputs of the complete drivetrain model and make an assessment of the feasibility for a decentralized SISO control solution, or a more advanced centralized MIMO control algorithm for below-rated operation of the wind turbine
3. Based on the physical limitations of the individual components that are currently used in the drivetrain model, describe a feasible control strategy.
 - (a) Derive a control strategy, taking into account the physical limitations of each drivetrain component that is currently used;
 - (b) Analyze what improvements could be done to allow for a control strategy which improves turbine operation and efficiency. These could involve changing the geometrical dimensions of components or physical limitations such as actuator speed.
4. Design a controller for the below-rated operational domain and evaluate this controller in a high-fidelity simulation environment;

1-7 Report Structure

This master's thesis presents five chapters. After this introductory chapter, the second chapter extensively describes the different components used in the DOT wind turbine, and models for these components are derived. The second chapter includes descriptions and modeling of the rotor, hydraulic pumps and motors, pipe line fluid dynamics and at last, spear valves are considered. The previously obtained knowledge is now combined into one single drivetrain model.

In Chapter 3, a control strategy is derived based on control methods used for conventional wind turbine control. It is discussed which operation points will be used, and an analysis on the system coupling is done. Based on this assessment, the actual controller design is presented.

Chapter 4 describes the control results of the control strategy and designed controllers, derived in the previous chapter. Simulations are performed using a high-fidelity non-linear model.

Finally, Chapter 5 combines the results in a final conclusion, and gives recommendations from an engineering perspective but also for possibilities of future research.



Chapter 2

Drivetrain Modeling

This chapter extensively describes the individual components which are part of the Delft Offshore Turbine (DOT) drivetrain. Both analytic relations and dynamical models for each of these individual components are derived. The schematic in Figure 2-1 illustrates the DOT drivetrain with enumerated labels for each type of component. These enumerated labels refer to the Sections of this Chapter. In Section 2-2, rotor characteristics are described and a dynamical rotor model is derived. Hereafter, Section 2-3 describes general pump and motor characteristics. Subsequently, each individual pump or motor model is adjusted based on efficiency data. Thereupon, Section 2-4 derives a model for fluid dynamics within a rigid pipe line. What remains are the spear valves which will be modeled in Section 2-5. Lastly, Section 2-6 describes the way in which these individual component models are linked together in a single drivetrain model.

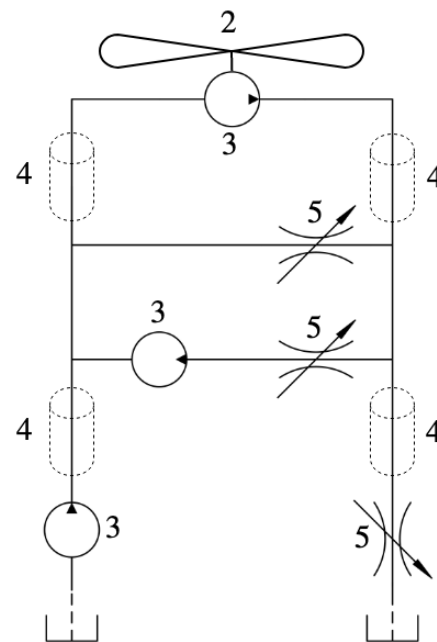


Figure 2-1: Schematic overview of the DOT drivetrain, containing enumerated labels for each type of component. These enumerated labels refer to the section which describes the modeling of this component.

2-1: Drivetrain component specification	16
2-2: Rotor model	18
2-3: Hydraulic pump and motor	22
2-4: Modeling of Fluid Dynamics in Hydraulic Pipe Lines	28
2-5: Spear Valve Modeling	33
2-6: Combined Drivetrain and Component Implementation	35

2-1 Drivetrain component specification

This section gives a brief description of the components as part of the hydraulic drivetrain with regenerative power system as illustrated in Figure 1-9b. Specifications and limitations are described after which each component is more extensively described and analyzed in the following sections of this chapter.

Rotor pump P_r

The rotor of the DOT wind turbine is mechanically coupled to a Kamat (K80120-5G) fixed-displacement high-pressure plunger water pump with five cylinders [35]. Its special five-cylinder design allows large volume flows without cavitation in the pump cylinders, given at least atmospheric pre-pressure. The integrated gearbox with oil forced lubrication and oil cooler enables a secure, continuous operation of the high-pressure pump. The gearbox has a ratio of 1:52.2. Figure 2-2 illustrates the Kamat pump and Table 2-1 contains the specifications of the Kamat rotor pump.

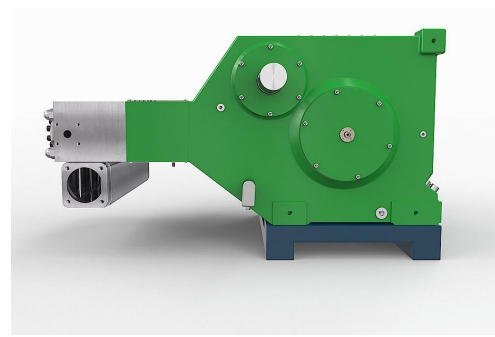


Figure 2-2: Picture of the Kamat K80120-5G fixed-displacement high-pressure plunger water pump with five cylinders [35].

Internal water motor M_1

The internal water motor as part of the Regenerative Power System (RPS) is a Janus MV160-225S axial piston (positive displacement) water motor [36]. Manufactured in 316 stainless steel, the product offers resistance to corrosive fluids. Minimal pulsation is experienced with these units due to the multiple piston design and the high operational speeds. An electrical generator is coupled to the Janus rotational shaft, and can exert a torque on the Janus motor shaft. The combination of demanded torque and the rotational speed of the water motor relates to the regenerated power of the RPS, used for operation of the pre-pressure Pleuger pumps. Figure 2-3 illustrates the Janus water motor and Table 2-1 contains the specifications of the Janus water motor.



Figure 2-3: Picture of the Janus MV160-225S axial piston fixed-displacement water motor [36].

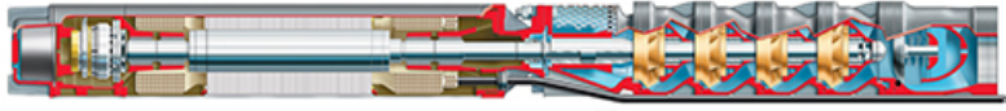


Figure 2-4: Picture of the submersible centrifugal pump 'NB64-23 + M6-600-2' from 'Pleuger Water Solutions' [37].

Pre-pressure pump P_{pp}

To pressurize the low pressure feed line, submersible centrifugal pumps (NB64-23 + M6-600-2) from 'Pleuger Water Solutions' are used [37]. Table 2-1 contains the specifications of a single Pleuger pre-pressure pump.

Spear valves S_i

Pressures in the feed and discharge line and the rotational speed of the internal (Janus) water motor are controlled by a variable-area orifices in the form of spear valves. By adjusting the spear position, valve resistance can be regulated. Decreasing opening area of the valve for equal flow rates results in higher pressure differentials across the valve. This phenomenon is used to control e.g. system torque, thus rotor speed, in the below-rated operational region. They also form high-speed water jets towards the Pelton turbine at the centralized hydro-power station. Figure 2-5 illustrates a schematic of one such spear valve with a nominal nozzle diameter D_{nz} of 26 mm, adjustable spear position s_s and a coning angle α of 50 degrees.

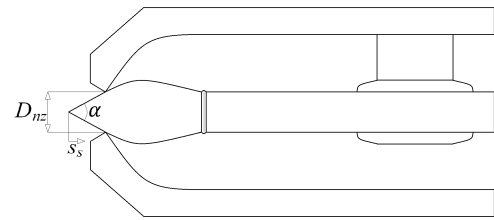


Figure 2-5: Schematic cross-section of the spear valves used. The nominal nozzle diameter is represented by D_{nz} , the distance of the spear head from its starting position (valve closed) by s_s and α is the coning angle of the spear

Rotor

Components as the rotor, nacelle and the yaw system are taken from a three-bladed Vestas V44 600 kW wind turbine. The rotor has a diameter of 44.0 m, a swept area of 1,521.00 m² and weighs 8.4 tons [38].

Description	Rotor pump	Water motor	Pre-pressure pump
Brand	Kamat	Janus	Pleuger
Type	K80120G-5M	MV160-225S	NB64-23 + M6-600-2
Volumetric displacement	2.3 l rev ⁻¹	0.225 l rev ⁻¹	0.14 l rev ⁻¹
Nominal speed	1500 rev min ⁻¹	300 - 2000 rev min ⁻¹	3600 rev min ⁻¹
Torque range available	0 - 5093 Nm	0 - 550 Nm	-
Pressure range available	0 - 125 bar	0 - 160 bar	0 - 40 bar
Torque range applied	0 - 3000 Nm	0 - 250 Nm	-
Pressure range applied	0 - 95 bar	0 - 95 bar	0 - 13 bar
Max. power demand	-	-	20 kW

Table 2-1: Specifications of the fixed-displacement hydraulic pumps and motor, part of the DOT drivetrain with regenerative power system as illustrated in Figure 1-9b.

2-2 Rotor model

This section elaborates on describing basic rotor characteristics after which the derivation of a simplified dynamical rotor model is presented.

Mikkelsen et al. [39] models the rotor of a wind turbine as an actuator disk. In this model, the rotor is represented by a permeable disk. The disk allows the flow to pass through the rotor, at the same time as it is subject to the influence of the surface forces. The ‘classical’ actuator disk model is based on conservation of mass, momentum, and energy, and constitutes the main ingredient in the 1D momentum theory.

The rotor with swept area A_r exerts a thrust force T on the mass air flow \dot{m} and extracts a power P , resulting in a decreasing velocity of the air flow. This phenomenon is often referred to as induction. Applying the law of conservation of mass shows that when the flow velocity decreases, the area of the stream tube increases, as Figure 2-6 illustrates.

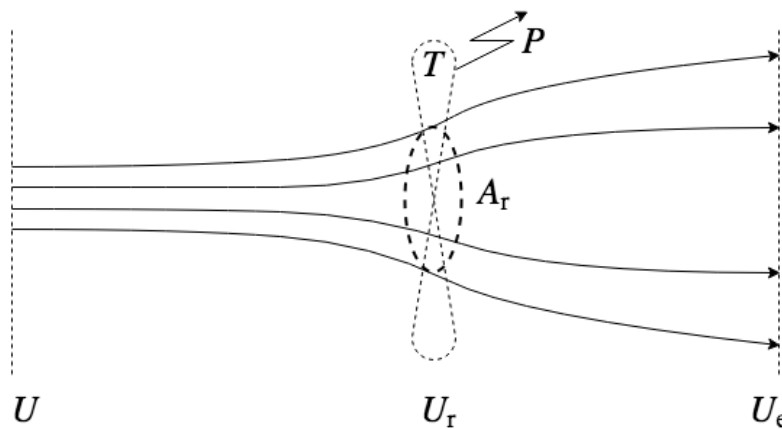


Figure 2-6: Actuator disk model where an air flow with velocity U enters the control volume, and leaves the control volume with velocity U_e . The velocity drop is a result of power extraction P by the actuator disk. The air flow at the actuator disk has velocity U_r , the thrust force is denoted as T and the swept rotor area is represented by A_r .

By equating the difference in power inside the wind entering and leaving the control volume $1/2\dot{m}(U^2 - U_e^2)$ and the power as a result of the thrust force $TU_r = \dot{m}(U - U_e)U_r$, the relation between the rotor wind speed and the incoming and outgoing wind speeds is defined as $U_r = (U + U_e)/2$. The relative decrease in wind speed from U to U_r is defined as the induction factor $a = (U - U_r)/U = \Delta U/U$. The air leaving the control volume thus has velocity $U_e = U(1 - 2a)$ [40].

The mass flow rate of air passing through the swept rotor area, the thrust force and the power extracted from the wind are defined as

$$\dot{m} = \rho_a U_r A_r = \rho_a U A_r (1 - a), \quad (2-1)$$

$$T = \dot{m}(U - U_e) = \frac{1}{2} \rho_a U^2 A_r 4a(1 - a), \quad (2-2)$$

$$P = \dot{m}(U - U_e)U_r = \frac{1}{2} \rho_a U^3 A_r 4a(1 - a)^2, \quad (2-3)$$

respectively, where the density of air is represented by ρ_a . The amount of energy that the rotor is capable of extracting from the wind is related to the induction factor a . In relation to this, Manwell et al. [40] describes that the fraction between the power yield of the rotor P_r and available wind power P_{wind} is defined as the power coefficient C_P (rotor efficiency). The extracted power from the wind with velocity U is now defined as

$$P = \frac{1}{2} \rho_a A_r U^3 C_P = \frac{1}{2} \rho_a \pi R^2 U^3 C_P, \quad (2-4)$$

where R represents the blade length of the rotor. Comparing Equations 2-3 and 2-4, it is concluded that, according to the momentum theory, the theoretical value of the power coefficient is related to the induction factor a as

$$C_P = 4a(1 - a)^2. \quad (2-5)$$

The maximum power coefficient is determined by taking the derivative of the power coefficient with respect to a and setting it equal to zero, yielding $a = 1/3$. Thus:

$$C_{P,\text{max}} = \frac{16}{27} = 0.5926 \quad (2-6)$$

is the theoretically highest attainable power coefficient, referred to as the Betz limit [40]. The same thing can be done for the thrust force T of the rotor. Figure 2-7 illustrates the power and thrust coefficient as a function of the induction factor. It shows that the velocity U_e of the air behind the rotor reaches 0 m s^{-1} at an induction factor of $a = 1/2$. Therefore, the Betz theory is only valid for $a < 0.5$. In practice, as the induction factor approaches and exceeds 0.5, complicated flow patterns that are not represented in this model occur [41], referred to as the turbulent wake state. Manwell et al. [40] describes the Glauert empirical relation for the thrust coefficient considering this turbulent wake state ($a > 0.5$).

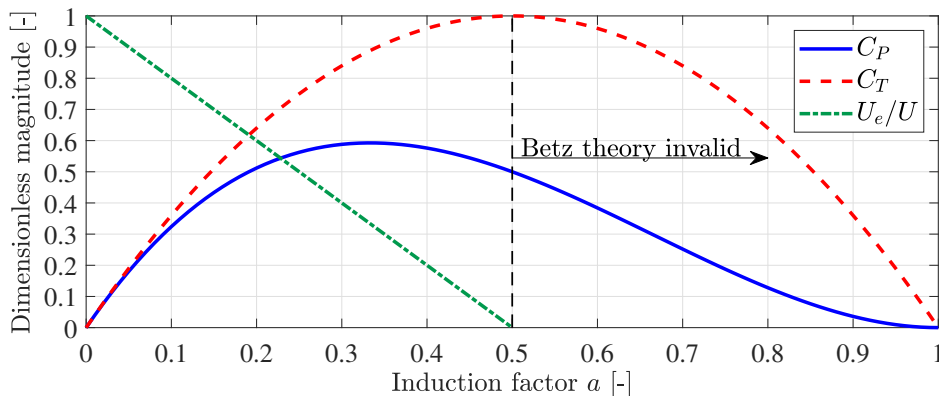


Figure 2-7: Operating parameters of a Betz turbine. The velocity of the undisturbed wind is represented by U and the wind velocity behind the rotor by U_e . The power and thrust coefficients are represented by C_P and C_T , respectively

During normal turbine operation in practice however, three effects lead to a decrease of the maximum achievable power coefficient:

- Rotation of the wake behind the rotor
- Finite number of blades and associated tip losses
- Non-zero aerodynamic drag

Moreover, the pitch angle β of the blades the rotational speed ω_r of the rotor with respect to the wind speed are highly influential on the rotor efficiency. According to Bianchi et al. [42], the rotor torque caused by the aerodynamic forces working upon the blades can be described as

$$\tau_r = \frac{1}{2} \rho_a \pi R^3 U_r^2 \frac{C_p(\lambda, \beta)}{\lambda}, \quad (2-7)$$

where the power coefficient C_p is a function of the blade pitch angle β and the dimensionless Tip-Speed Ratio (TSR) λ defined as

$$\lambda = \frac{\omega_r R}{U_r}. \quad (2-8)$$

Multiplication of Equation 2-7 with the rotational speed ω_r of the rotor leads to the extracted rotor power, similar to Equation 2-4.

The relation between the power coefficient and the torque coefficient C_τ is given by $C_\tau(\lambda, \beta) = C_p(\lambda, \beta)/\lambda$, such that Equation 2-7 can be written as

$$\tau_r = \frac{1}{2} \rho_a \pi R^3 U_r^2 C_\tau(\lambda, \beta) \quad (2-9)$$

In Mulders et al. [28], Blade Element Momentum (BEM) theory [4][40] was applied on the DOT rotor blade airfoils. Power and torque extraction capabilities of the rotor were translated to power and torque coefficient curves depending on blade pitch angle and TSR. Figure 2-8 shows the power and torque coefficient curve at fine-pitch angle β_0 , dependent of the TSR λ . The fine-pitch angle β_0 is the blade pitch position of that results in maximum power extraction from the wind in the below-rated operational domain [78]. Mulders et al. [28] found that the theoretical maximum rotor power and torque coefficient equal $C_{p,\max} = 0.48$ and $C_{\tau,\max} = 7.2 \cdot 10^{-2}$ at TSRs of 7.8 and 5.9, respectively.

The entire data set of power, torque and thrust coefficients is made publicly accessible as an external supplement under Mulders et al. [43].

In terms of rotor dynamics, Leithead and Connor [44] propose a first-order dynamical model, directly relating the rotor acceleration to its inertia, the rotor torque τ_r caused by the wind and the system torque τ_{sys} , exerted by the drivetrain, according to the Newton law for rotational motion

$$J_r \dot{\omega}_r = \tau_r - \tau_{\text{sys}} \quad (2-10)$$

where J_r represents the rotor inertia and ω_r the rotor rotational speed. The rotor inertia J_r is not publicly available, but Rodriguez [45] provided for a method to estimate the rotor inertia. The rotor inertia was estimated at $6.6 \cdot 10^5 \text{ kg m}^2$. This theoretical result has later been confirmed by Jager [46] by performing experiments on the actual turbine.

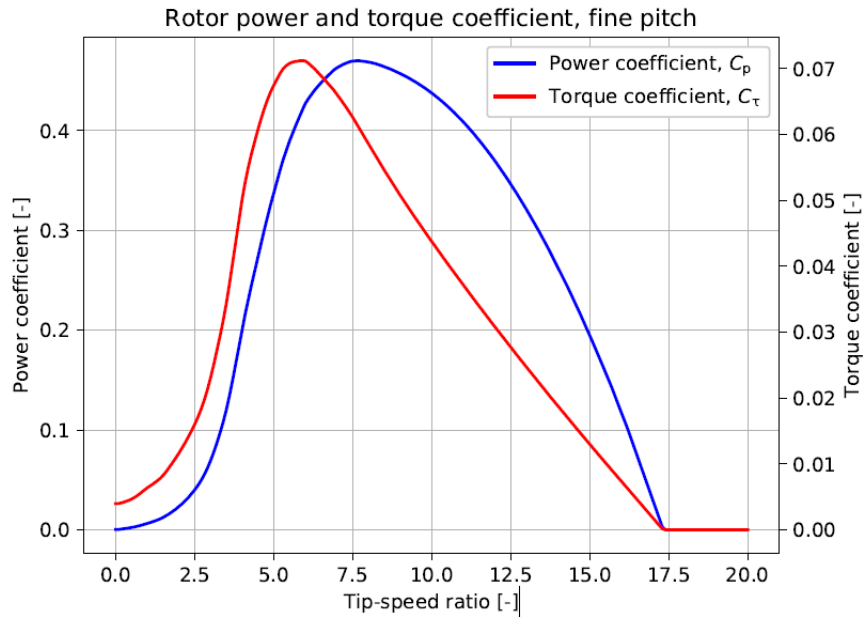


Figure 2-8: DOT500 rotor power and torque coefficient curves as functions of the TSR, obtained from a BEM analysis based on measured data of the blade-geometry. $C_{p,max} = 0.48$ at $\lambda = 7.8$. $C_{\tau,max} = 7.2 \cdot 10^{-2}$ at $\lambda = 5.9$ [28]

The system torque τ_{sys} counteracts the rotor torque and is influenced by all components employed in the hydraulic drivetrain. The off-the-shelf drivetrain components, introduced in section 2-1, have different energy conversion characteristics that will influence the operating behavior of the wind turbine. These components will be described more extensively and dynamical models will be derived in the remaining sections of this chapter.

Hydraulic components generally have high torque-to-inertia ratios which results in high acceleration capabilities [13]. Generally, consideration of pump and motor inertias is of unquestionable relevance in typical hydraulic power drive systems. However, in this particular wind turbine setup, the rotor inertia is considerably bigger compared to the pump inertia. After performing an analysis on this subject, Kempenaar [70] concluded that including component dynamics did not significantly improve model accuracy. In this thesis report therefore, it is assumed that the dynamics of the hydraulic pump in this drivetrain can be neglected, and that power conversions are given by static relations.

2-3 Hydraulic pump and motor

This section elaborates on modeling of the fixed displacement hydraulic pumps and motors. First some general pump equations are derived. Thereafter, efficiency data is analyzed and described in the form of fitted functions. This is first done for the hydraulic rotor pump, followed by the internal water motor and at last for the submersible pre-pressure pumps.

2-3-1 Rotor pump

The rotor pump (P_r) is a positive displacement pump, also known as reciprocating pump. These pump types can handle much higher pressures than hydrodynamic pumps [82][14], e.g. centrifugal pumps. There is a distinction between piston and plunger positive displacement pumps. Both types have the same working principle, but where the high-pressure seals reciprocates with the piston inside a piston pump, the high-pressure seal is stationary inside plunger pumps. This allows the latter to operate at even higher pressures. The Kamat pump, used in the DOT wind turbine, has five cylinders, of which there is one illustrated by the schematic of Figure 2-9.

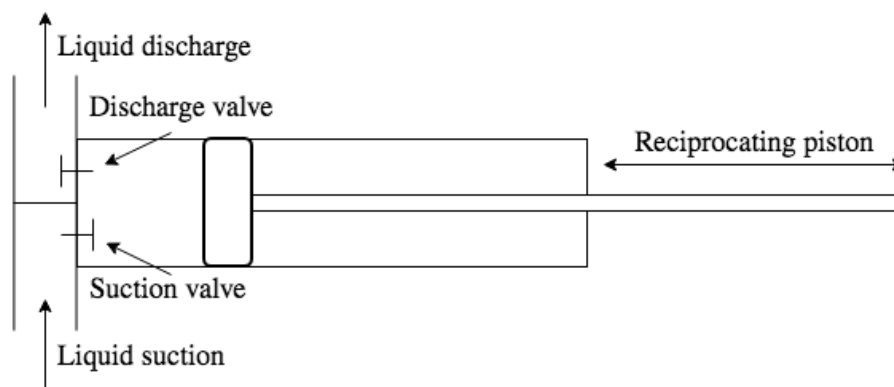


Figure 2-9: Positive displacement piston pump schematic. Liquid is provided through the liquid suction line. The piston is mechanically coupled to a rotating crankshaft which causes the piston to reciprocate to the left and right. When the piston moves to the right, the suction valve opens and liquid is sucked into the pressure chamber. When the piston 'pushes' to the left, the discharge valve opens and the liquid leaves the chamber under pressure through the liquid discharge line.

A positive displacement pump delivers a flow Q_p proportional to the rotational speed of the pump shaft, assuming that both volumetric and mechanical losses are present. Volumetric losses occur due to clearances in the pump that cause the fluid to partially slip back to the feed side of the pump. Mechanical losses are caused by slip and friction, and are influenced by characteristics of both the pump and the fluid.

Volumetric efficiency In general, a pump's volumetric efficiency is determined by the ratio of net flow and ideal flow [9]. The net flow is defined as the ideal flow minus the total slip flow Q_p due to leakage. This incorporates both the internal leakage between high and low pressure lines and the external leakage between the internal chambers and the case

drain. The slip flow is defined as

$$Q_{s,p} = C_{s,p} \frac{\Delta p_p}{\mu}, \quad (2-11)$$

where $C_{s,p}$ is the laminar leakage coefficient of the pump, Δp_p the pressure differential across the hydraulic pump and μ the dynamic viscosity [9][88]. This leads to a volumetric efficiency $\eta_{v,p}$ of

$$\eta_{v,p}(\omega_p, \Delta p_p) = \frac{Q_p}{V_p \omega_p} = 1 - C_{s,p} \frac{\Delta p_p}{V_p \mu \omega_p}, \quad (2-12)$$

where V_p represents the radial volumetric displacement of the pump and ω_p the rotational velocity of the pump shaft. Turbulent leakage flows are described in [89][90], but will not be considered in this thesis.

Assuming constant fluid properties, the volumetric efficiency is dependent of the pump's rotational speed and the pressure differential across the pump, hence the volume flow produced by the positive displacement pump is defined as

$$Q_p = V_p \omega_p \eta_{v,p}(\omega_p, \Delta p_p). \quad (2-13)$$

However, Diepeveen [9] and Trostmann [91] state that volumetric efficiencies of positive displacement pumps are generally high and more or less constant over the entire range of operation. Therefore, volumetric losses of the rotor pump are assumed constant at $\eta_{v,r} = 0.93$, as proposed by Mulders et al. [28] for a similar pump.

Mechanical efficiency In terms of mechanical losses, Nesbitt [14] states that a pump's maximum attainable pressure is dependent of the mechanical construction and driving power. The first can be accounted for by mechanical design, however, the latter imposes actual practical limitations. In an ideal pump, the maximum attainable pressure is described as

$$\Delta p_p = \frac{\tau_p}{V_p}, \quad (2-14)$$

where τ_p is the driving torque supplied by e.g. the rotor to the pump shaft, which means that the rotor torque limits the maximum attainable pressure (assuming a fixed volumetric volume displacement V_p). Including torques caused by damping and friction results in a driving torque described as

$$\tau_p = V_p \Delta p_p + \tau_f + \tau_d, \quad (2-15)$$

where τ_d is caused by viscous forces, and τ_f by frictional forces. The torque caused by viscous damping is proportional to the rotational speed of the pump as $\tau_d = C_d \mu \omega_p$, where C_d represents the damping coefficient and μ the dynamic viscosity of the fluid. The frictional torque τ_f is the resultant torque caused by pressure on the pump's geometry and is described by $\tau_f = C_f V_p \Delta p_p$, where C_f is the Coulomb frictional coefficient. Substituting those relations in Equation 2-15 results in a pump torque of

$$\tau_p = (1 + C_f) V_p \Delta p_p + C_d \mu \omega_p = \frac{V_p \Delta p_p}{\eta_{m,p}(\omega_p, \Delta p_p)}. \quad (2-16)$$

According to Nesbitt [14] however, the mechanical efficiency of positive displacement (reciprocating) pumps is generally not affected by pump speed or viscosity, thus only the pressure differential across the pump.

Data fitted function During in-field testing, mechanical efficiency data was gathered for the Kamat rotor pump. A function was fitted on this data for model implementation. This is done with Mean Squared Error (MSE) minimization, using the Particle Swarm Optimization (PSO) algorithm [83]. Appendix A-1 further elaborates on the PSO algorithm. The MSE cost function looks like

$$\arg \min_{\vec{a} \in \mathbb{R}^2} \frac{1}{n} \sum_{i=1}^n \left(\eta_{m,r}(\Delta p_{r,i}) - \check{\eta}_{m,r}(\vec{a}, \Delta p_{r,i}) \right)^2 \quad (2-17)$$

where Δp_r is the pressure differential across the rotor pump in Pa, $\eta_{m,r}$ is the mechanical efficiency of the rotor pump gathered from the data, $\check{\eta}_{m,r}$ is the estimated and parameterized mechanical efficiency and n is the amount of data points. Vector \vec{a} contains the coefficients a_i of the fitting function which looks like

$$\check{\eta}_{m,r}(\vec{a}, \Delta p_r) = a_1 - e^{-\frac{\Delta p_r}{a_2 \cdot 10^5}}. \quad (2-18)$$

The PSO algorithm returned $a_1 = 0.81$ and $a_2 = 5.38$ for a fit with mean error of 3.6%. Figure 2-10 shows the efficiency data and the fitted function

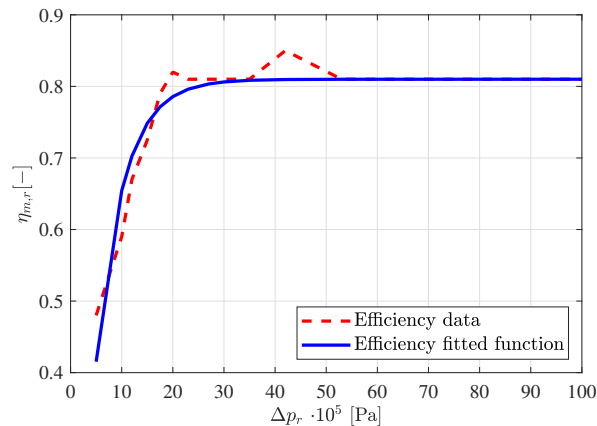


Figure 2-10: Mechanical efficiency data of the Kamat rotor pump, gathered during in-field testing. The fitted function is $\eta_{m,r} = a_1 - e^{-\Delta p_r / (a_2 \cdot 10^5)}$ where $a_1 = 0.81$ and $a_2 = 5.38$ and Δp_r is the pressure differential across the rotor pump. The fitted function has a mean error of 3.6% with respect to the efficiency data.

However, this would mean a negative efficiency in the very low pressure region. This is not realistic and since the lack of data in this pressure region, a constant efficiency of 0.5 is assumed. The estimated function intersects with $\eta_{m,r} = 0.5$ for $\Delta p_r = 6.3 \cdot 10^5$ bar. The relation between torque τ_r of the rotor pump and the pressure differential Δp_r across it, is now defined as

$$\tau_r(\Delta p_p) = \begin{cases} \frac{V_r \Delta p_r}{0.5} & \text{if } \Delta p_p \leq 6.3 \cdot 10^5, \\ \frac{V_r \Delta p_r}{\check{\eta}_{m,r}(\Delta p_r)} & \text{if } \Delta p_p > 6.3 \cdot 10^5. \end{cases} \quad (2-19)$$

2-3-2 Internal water motor

The same derivations hold for positive displacement hydraulic motors (e.g. water motor M1). However, the direction of energy transfer is exactly opposite. Since the flows through the internal water motor M1 are relatively small compared to the rest of the system, both mechanical and volumetric efficiency characteristics are assumed constant. The motor torque is dependent of pressure differential Δp_{M1} across the water motor as

$$\Delta p_{M1} = \frac{\tau_{M1}}{V_{M1}\eta_{m,M1}}, \quad (2-20)$$

with mechanical efficiency $\eta_{m,M1} = 0.90$ and volumetric motor displacement V_{M1} . The rotational speed of the motor, induced by the water flow Q_{M1} going through it, is defined as

$$\omega_{M1} = \frac{Q_{M1}}{V_{M1}}\eta_{v,M1}, \quad (2-21)$$

with the volumetric motor efficiency $\eta_{v,M1} = 0.95$.

2-3-3 Pre-pressure pump

The pre-pressure pumps (P2) are of the centrifugal type. Besides the rotational speed of the pump shaft, also the pump's operational pressure has a big influence on the flow displacement, more than for e.g. a positive displacement piston pump. This in effect results in a decreasing flow rate when the pressure in the pump's discharge line increases, assuming constant rotational speed of the pump shaft. Efficiency data mappings of the flow displacement were provided by the Pleuger Pumps manufacturer. The three-dimensional chart in Figure 2-11a shows the pump's flow rate Q for all combinations of discharge pressure p of the pump and rotational speed ω_{pp} of the pump shaft.

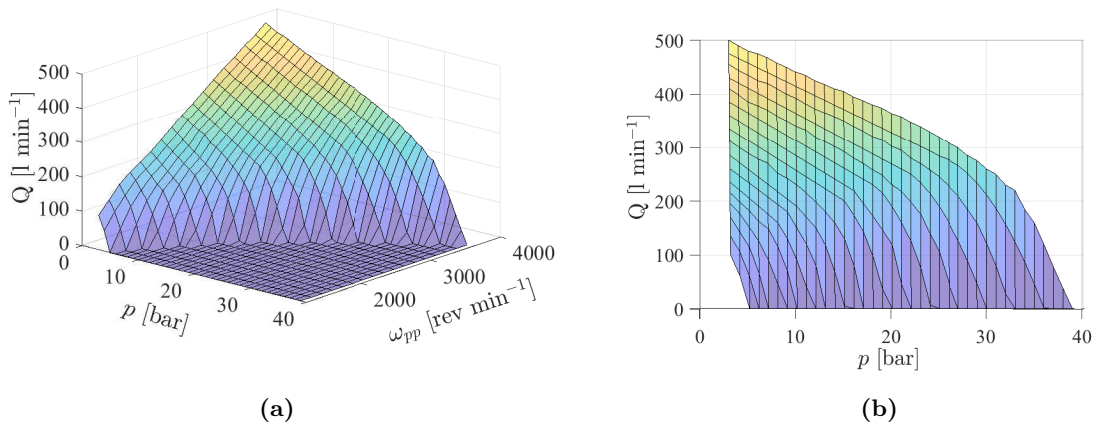


Figure 2-11: (a) Flow delivery $Q_{pp}(p_{pp,i}, \omega_{pp,j})$ of one single Pleuger pre-pressure pump against the pump's operational pressure and rotational speed of the pump; (b) Side view of (a), showing the relation between pump's operational pressure and its flow delivery $Q_{pp}(p_{pp,i}, \omega_{pp,j})$.

Figure 2-11b presents a side view of Figure 2-11a, showing the relation between delivered flow rate and the pump's operating pressure more clearly. The parabolic looking curves belong to constant rotational speeds of the pre-pressure pump. Assuming a constant

rotational speed of the pump shaft, the relation between flow rate and the pump pressure seems linear for higher rotational speed of the pump shaft in the lower pressure regions ($p < 12$ bar). For lower rotational speeds, a more 'parabolic' shape appears.

A parameterizable function is fitted on the pump's flow rate dependent of the discharge pressure and the rotational speed of the pump shaft. This is again performed with the PSO algorithm (Appendix A-1). The MSE cost function looks like

$$\arg \min_{\vec{b} \in \mathbb{R}^2} \frac{1}{mn} \sum_{j=1}^m \sum_{i=1}^n \left(Q_{pp}(p_{pp,i}, \omega_{pp,j}) - \check{Q}_{pp}(\vec{b}, p_{pp,i}, \omega_{pp,j}) \right)^2, \quad (2-22)$$

where $Q_{pp}(p_{pp,i}, \omega_{pp,j})$ represents the pump's flow rate based on data provided in the pump specifications sheet, $\check{Q}_{pp}(p_{pp,i}, \omega_{pp,j})$ the estimated flow, p_{pp} is the pump's discharge pressure and ω_{pp} is the rotational speed of the pre-pressure pump. Vector \vec{b} contains the coefficients b_i of the fitting function $\check{Q}_{pp}(p_{pp}, \omega_{pp})$ and m and n are the amount data points for rotational speed of the pump shaft and pump discharge pressure respectively, provided by the manufacturer. The following fitting function was assumed

$$\check{Q}_{pp}(p_{pp}, \omega_{pp}) = b_1 p_{pp}^{1 + ((\omega_{\max} - \omega_{pp}) / \omega_{\max})} + b_2 \omega_{pp}, \quad (2-23)$$

where ω_{\max} of $3600 \text{ rev min}^{-1}$ is the maximum rotational speed of the pump shaft. The PSO returned the parameters $b_1 = -6.2781$ and $b_2 = 0.1399$, resulting in a mean error of 3.5% between the fitted function and the data provided in the pump's specification sheet. Figure 2-12 shows the fitted function on top of the data provided in the specification sheet.

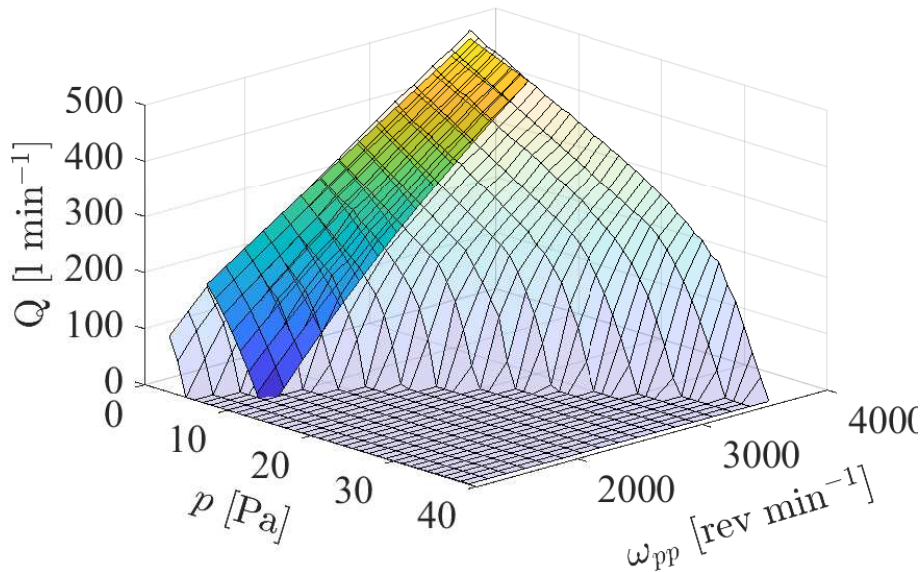


Figure 2-12: In transparent, the flow delivery $Q_{pp}(p_{pp,i}, \omega_{pp,j})$ of one single Pleuger pre-pressure pump against the pump operational pressure and rotational speed of the pump. The opaque plane illustrates the estimated flow delivery $\check{Q}_{pp}(p_{pp}, \omega_{pp})$ of one single pre-pressure pump.

This function is now translated to a relation for volumetric efficiency by dividing the fitted flow function for the maximum flow rate for each rotational speed of the pump shaft, which is $b_2\omega_{pp}$. The volumetric efficiency estimate of the pre-pressure pump is represented by the following relation

$$\check{\eta}_{v,pp}(p_{pp}, \omega_{pp}) = 1 + \frac{b_1}{b_2\omega_{pp}} p_{pp}^{1+((\omega_{max}-\omega_{pp})/\omega_{max})}. \quad (2-24)$$

Using Equation 2-13 and 2-24, the flow relation for a single pre-pressure pump becomes

$$Q_{pp} = V_{pp}\omega_{pp}\check{\eta}_{v,pp}(\omega_{pp}, p_{pp}). \quad (2-25)$$

Furthermore, as earlier mentioned in Section 2-1, the power demand for operation of one pre-pressure at its maximum rotational speed is 20 kW. For convenience it is assumed that the power demand and rotational speed of the pre-prepressure pump are proportional. At 3600 rev min⁻¹, the power demand is 20 kW.

2-4 Modeling of Fluid Dynamics in Hydraulic Pipe Lines

This section elaborates on the modeling of static and dynamic fluid relations in rigid hydraulic pipe lines. Firstly a relation for assumed static pressure losses is derived, followed by the derivation of differential equations that are relating the dynamic pressure loss across a hydraulic pipe line to fluid characteristic properties as induction, resistance and capacitance.

In hydraulics, a steady uniform flow in a component with a single entrance and exit is characterized by the following energy equation

$$-\frac{\dot{W}_s}{\dot{m}g} = \frac{V_2^2 - V_1^2}{2g} + \frac{p_2 - p_1}{\rho g} + z_2 - z_1 + h_L, \quad (2-26)$$

where \dot{W}_s is the work rate (power) performed by the fluid, \dot{m} the mass flow rate, V_1 and V_2 the fluid velocity at the entrance and the exit respectively and p_1 and p_2 the respective static pressures at the entrance and exit. Furthermore, g represents the gravitational constant, ρ the fluid density, z_1 and z_2 the elevation above a reference plane at the entrance and exit, respectively, and h_L the hydraulic loss [55]. All terms in Equation 2-26 have dimensions of height and are named kinematic head, piezometric head, geometric head and loss head, respectively, at the right-hand side of the equal sign. Analysis of hydraulic power and control systems however, are easier to perform with respect to pressures rather than heads. Equation 2-26 is therefore rewritten as

$$\frac{1}{2}\rho V_1^2 + p_1 + \rho g z_1 = \frac{1}{2}\rho V_2^2 + p_2 + \rho g z_2 + p_L, \quad (2-27)$$

where the hydraulic loss is now represented as pressure loss p_L . The flow rates within the DOT wind turbine are limited by approximately $3 \text{ m}^3 \text{ s}^{-1}$. The constant line diameter of 0.1 m results in a maximum kinematic pressure difference in the order of magnitude 10^4 Pa . This is a lot smaller than the static pressures in the range of $[5 - 100] \cdot 10^5 \text{ Pa}$. Since line diameter is assumed constant for the whole DOT drivetrain as well, pressure differences caused by kinematic head are neglected in this model which eliminates the terms $\rho V_i^2/2$. The steady uniform flow in a line component is now defined as

$$p_1 + \rho g z_1 = p_2 + \rho g z_2 + p_L, \quad (2-28)$$

Geometric head is considered since the height difference between components of the DOT drivetrain is significant, especially in the low pressure feed line. The pressure differential across a pipe element is therefore given by

$$\Delta p = \rho g(z_2 - z_1) + p_L, \quad (2-29)$$

where the pressure differential across a pipe line element is caused by difference in elevation levels and hydraulic losses. White [56] describes a dynamical model for hydraulic pressure losses caused by inductive, resistive and compressive characteristics of both the pipe line itself and the fluid flowing through it. Buhagiar [24] already used this approach to model these dynamic pipe losses for a hydraulic wind turbine model.

The pipe line is modeled as a particular amount of pipe segments which all consists of an inductive, a resistive and a compressive element. One such segment is illustrated in Figure 2-13.

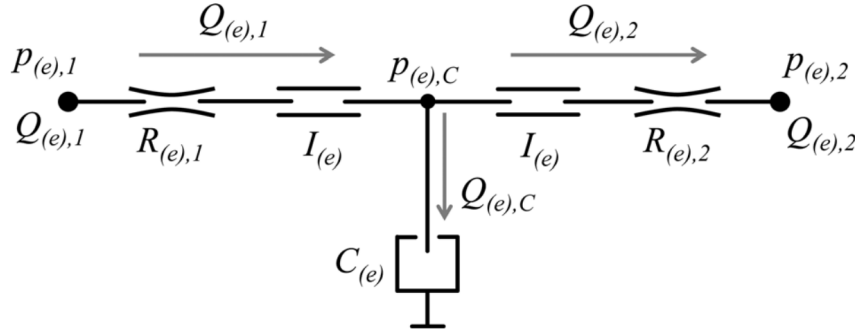


Figure 2-13: Dynamic pipe line segment, including inductive, resistive and compressive characteristics of the pipe and the fluid [24].

Each hydraulic line segment has an upstream elemental flow $Q_{(e),1}$ and pressure $p_{(e),1}$, and a downstream elemental flow $Q_{(e),2}$ and pressure $p_{(e),2}$.

The term $Q_{(e),C}$ is the net flow (difference between in- and outflow) and is linked to the capacitive characteristics of the line segment. This could include both compressibility of the fluid and compliance of the pipe walls, however, wall compliance is neglected since the piping is constructed with rigid steel. The inductive and resistive elements are illustrated as $I_{(e)}$ and $R_{(e),i}$ respectively.

Using White [56] and Murrenhoff [60], the following differential equations for pressure loss across a pipe segment can be derived as

$$p_{(e),1} - p_{(e),C} = I_{(e)} \dot{Q}_{(e),1} + R_{(e),1} Q_{(e),1} \quad (2-30)$$

$$p_{(e),C} - p_{(e),2} = I_{(e)} \dot{Q}_{(e),2} + R_{(e),2} Q_{(e),2} \quad (2-31)$$

$$\dot{p}_{(e),C} = \frac{1}{C_{(e)}} Q_{(e),C}, \quad (2-32)$$

where $p_{(e),C}$ represents the accumulated pressure caused by a non-zero net flow in the past. Hydraulic inductance, resistance and capacitance are individually discussed next.

Hydraulic inductance

Hydraulic induction resembles the ease of acceleration of a fluid volume and is therefore related to the fluid's inertia

$$I_{(e)} = \Delta p_{(e)} \left(\frac{dQ_{(e)}}{dt} \right)^{-1} = f_c \frac{4\rho L_{(e)}}{\pi D_p^2} \quad (2-33)$$

where $L_{(e)}$ is the length of the line segment and f_c a correction factor. This relation holds under the assumption that the flow speed profile is radially uniform [61]. Bansal [62] states that for this reason a distinction should be made between laminar and turbulent inductance, with a correction factor of $f_c = 4/3$ for turbulent flows. For laminar flows $f_c = 1$.

Hydraulic resistance

Hydraulic resistance causes dissipation of energy from a fluid flow in the form of a pressure loss across a hydraulic element. Hydraulic resistance could be taken advantage of by means of control valves, allowing adjustment of the valve set point, thus the hydraulic resistance it exerts. Another advantage of hydraulic resistance is that it could result in less leakage [60] since hydraulic resistance is directly proportional to fluid viscosity.

White [55] defines the pressure loss over a pipe element caused by friction as

$$\Delta p_{(e)} = f_f \frac{8\rho L_{(e)}}{\pi^2 D_p^5} Q_{(e)}^2, \quad (2-34)$$

where f_f represents the Darcy friction factor of the pipe. Murrenhoff [60] applies an analogy between electric and hydraulic circuitry such that the hydraulic resistance $R_{(e),i} = \Delta p_{(e)}/Q_{(e)}$ (analogous to $R = U/I$ for electric circuits). White [55] describes that friction resistance for laminar flows is caused by wall shear between the pipe wall and the fluid. The laminar friction factor is defined as

$$f_f = \frac{K_s}{\text{Re}}, \quad (2-35)$$

where the constant K_s is defined as the shape factor (e.g. for pipes with circular cross-sections $K_s = 64$) and Re the Reynolds number

$$\text{Re} = \frac{Q_{(e)} D_p}{\nu A} = \frac{4Q_{(e)}}{\nu \pi D_p}, \quad (2-36)$$

where ν is the kinematic viscosity. According to White [55], flows with a Reynolds number larger than 4000 can be considered turbulent, whereas flows with a Reynolds number smaller than 2000 can be considered laminar. Substitution of Equations 2-35 and 2-36 in Equation 2-34 leads to a pressure drop across the pipe segment of

$$\Delta p_{(e)} = K_s \frac{2\mu L_{(e)}}{\pi D_p^4} Q_{(e)}, \quad (2-37)$$

where μ is the dynamic viscosity ($\mu = \nu\rho$). It can be concluded that the hydraulic pressure loss caused by friction in laminar pipe flow is linearly proportional to the flow rate $Q_{(e)}$ through the pipe segment. However, this only holds for laminar flows, which in the offshore turbine set-up using seawater will not be the case.

Flows in the DOT drivetrain will be in the turbulent regime since $\text{Re} \gg 4000$. Hydraulic resistance in a turbulent regime becomes a very non-linear phenomenon as it is strongly affected by the surface roughness of the pipe wall as well. White [55] describes a distinction between friction factors for smooth- and rough-walled pipes in the turbulent flow regime. The smooth wall relations are only dependent of the Reynolds number

$$\frac{1}{f_f^{1/2}} = 2.0 \log \left(\text{Re} f_f^{1/2} \right) - 0.8 \quad (2-38)$$

For very rough pipes, the influence of viscosity vanishes and the friction factor is only dependent of the pipes's surface roughness, expressed as the surface roughness height ϵ relative to the pipe diameter D_p .

$$\frac{1}{f_f^{1/2}} = -2.0 \log \left(\frac{\epsilon/D_p}{3.7} \right) \tag{2-39}$$

To cover the transitionally rough range between smooth and rough turbulent pipe flows, Colebrook combined both Equations 2-38 and 2-39 into a more convenient formula

$$\frac{1}{f_f^{1/2}} = -2.0 \log_{10} \left(\frac{\epsilon/D_p}{3.7} + \frac{2.51}{Re f_f^{1/2}} \right) \tag{2-40}$$

In 1944, this formula was plotted by Moody into what's now called the Moody Chart for pipe friction, illustrated in Figure 2-14.

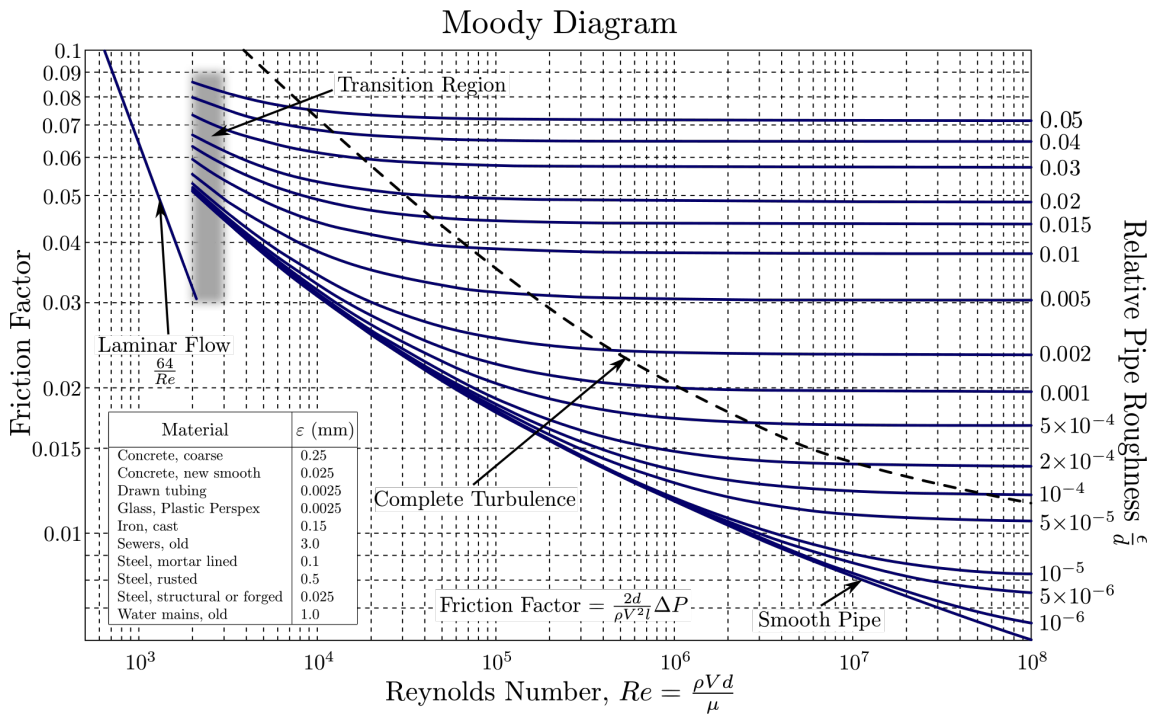


Figure 2-14: Moody Chart for pipe friction for smooth and rough walls [55]

The Moody chart is a chart in non-dimensional form, relating the Darcy friction factor f_f to the Reynolds number and the surface roughness height for fully developed flow. An alternative explicit formula was given by Haaland [63] as

$$\frac{1}{f_f^{1/2}} = -1.8 \log_{10} \left[\frac{6.9}{Re} + \left(\frac{\epsilon}{3.7D_p} \right)^{1.11} \right] \tag{2-41}$$

and varies less than 2 percent from Equation 2-40 [55]. Substituting this relation in Equation 2-34 leads to the hydraulic pressure loss caused by friction in a turbulent pipe flow of

$$\Delta p_{(e)} = \frac{8\rho L_{(e)} Q_{(e)}^2}{\pi^2 D_p^5} \left(-1.8 \log_{10} \left[\frac{6.9}{Re} + \left(\frac{\epsilon}{3.7D_p} \right)^{1.11} \right] \right)^{-2} \tag{2-42}$$

which is not nearly linearly proportional to the flow $Q_{(e)}$ through the pipe segment as for the laminar flow described in Equation 2-37.

Hydraulic capacitance

Compressibility of a fluid allow the amount of fluid within a control volume to increase or decrease as a result of pressure changes on the fluid an is therefore called hydraulic capacitance [9][60]. The effective bulk modulus K_{bulk} of a fluid represents the fluid's stiffness and is defined as the change in pressure relative to a volume change [60]

$$K_{\text{bulk}} = V_{(e)} \frac{dp}{dV}, \quad (2-43)$$

where $V_{(e)}$ represents the control volume $\frac{1}{4}\pi D_p^2 L_{(e)}$ of the pipe segment. Subsequently, taking the time derivative of the pressure leads to

$$\dot{p}_{(e)} = \frac{dp_{(e)}}{dt} = \frac{K_{\text{bulk}}}{V_{(e)}} \frac{dV}{dt} = \frac{K_{\text{bulk}}}{V_{(e)}} Q_{(e),C} = \frac{4K_{\text{bulk}}}{\pi D_p^2 L_{(e)}} Q_{(e),C} = \frac{1}{C_{(e)}} Q_{(e),C} \quad (2-44)$$

where $Q_{(e),C}$ is the net flow ($Q_{(e),1} = Q_{(e),2}$) and $C_{(e)}$ the hydraulic capacitance as illustrated in Figure 2-13. One can see that the hydraulic capacitance is directly proportional to the control volume. It results in a pressure differential across the pipe segment due to a non-zero net flow into the control volume, integrated over time, as

$$\Delta p_{(e)} = \frac{1}{C_{(e)}} \int Q_{(e),C} dt \quad (2-45)$$

Combined pipe line segment model

The hydraulic pressure loss p_L which is part of Equation 2-29 can now be expanded by the hydraulic inductance, resistance and capacitance terms derived above. The new differential equation, describing the hydraulic losses of one pipe line segment, is now given by

$$\Delta p_{(e)} = \rho g(z_2 - z_1) + I_{(e)} \frac{dQ_{(e)}}{dt} + R_{(e)} Q_{(e)} + \frac{1}{C_{(e)}} \int Q_{(e),C} dt \quad (2-46)$$

The amount of pipe segments per pipe line model is chosen to be 2. In the upcoming example, a single pipe line with one single spear valve at the end is considered. In Buhagiar et al. [24] it was concluded that a pipe line with 1 pipe segment did not differ a lot in time domain pressure response with respect to higher order pipe line models. Besides, from a computational effort perspective, minimizing the amount of pipe segment per pipe line is desirable. However, analyzing the Bode magnitude and phase plot of the transfer function between the spear position and the pressure at the entry of the pipe line, two pipe segment seems more sufficient for controller design. Figure 2-15 shows that the pipe model with two segments includes a resonance peak in upward direction where the pipe line model with just one segment does not. The model with three segments on the other hand, also includes a peak at a higher frequency, however, with a smaller magnitude than the first one. Since the two-segment model included the first peak which could be critical for maintaining stability margins during control design, the two-segment pipe line model is used in the drivetrain model.

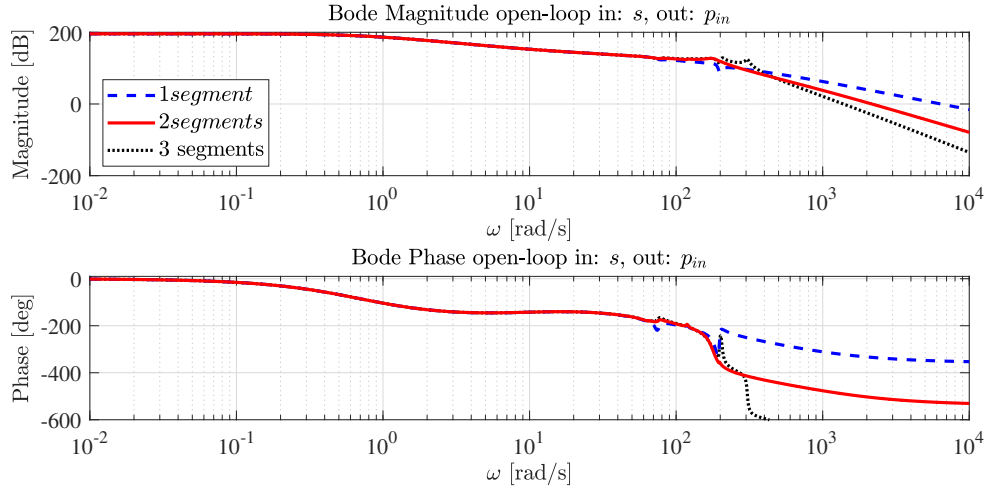


Figure 2-15: Bode magnitude and phase plot of the transfer function between spear position and pressure at the entrance of a pipe line. Three different transfer functions are presented for a pipe line with one, two and three pipe segments.

2-5 Spear Valve Modeling

This section elaborates on the modeling of the spear valves. Static relation for pressure loss will be combined with a first-order dynamic actuator model of the moving spear.

Pressures and flows in the hydraulic seawater lines are controlled by the employment of spear valves. One of such is schematically visualized in Figure 2-16a. The variable nozzle opening area A_{nz} is variable according to the relation

$$A_{nz}(s) = \frac{1}{4}\pi D_{nz}^2 - \pi \left((s_{\max} - s) \tan\left(\frac{\alpha}{2}\right) \right)^2, \quad (2-47)$$

where $\{s \in \mathbb{R} \mid 0 \leq s \leq s_{\max}\}$ represents the position of the spear in the circular cross-section of the nozzle head, D_{nz} is the nominal nozzle diameter and α the coning angle of the spear tip. The maximum spear position (nozzle fully opened) is defined as

$$s_{\max} = \frac{D_{nz}}{2 \tan(\alpha/2)}. \quad (2-48)$$

A mapping for spear positions to effective nozzle area for different nozzle diameters D_{nz} is given in Figure 2-16b.

White [55] describes the energy conversion over a nozzle with the Bernoulli equation for incompressible flows

$$\frac{1}{2}\rho V_1^2 + \rho g z_1 + p_1 = \frac{1}{2}\rho V_2^2 + \rho g z_2 + p_2, \quad (2-49)$$

where V_i is the water velocity and p_i is the static water pressure. Subscripts $(\cdot)_1$ and $(\cdot)_2$ indicate the location before and after the nozzle, respectively [55]. As in the given control volume the height difference Δz is negligible and the water density ρ_w and gravitational constant g are constant, the potential term is disregarded. Using Equation 2-49,

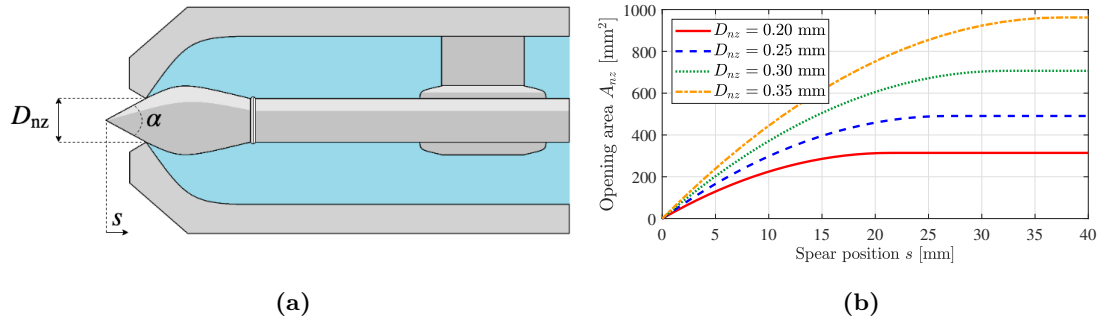


Figure 2-16: (a) Schematic cross-section of the spear valves used. The nominal nozzle diameter is represented by D_{nz} , the distance of the spear head from its starting position (valve closed) by s_s and α is the coning angle of the spear; (b) Effective nozzle area as function of the spear position in the circular cross-section of the nozzle head. The spear valve is fully closed at $s = 0$ and fully opened at $s = s_{max}$ of which the latter is variable according to the nozzle head diameter.

an expression for the discharge water pressure p_1 is obtained

$$p_1 = \frac{\rho}{2} \left(\frac{Q_{nz}}{C_d A_{nz}(s_s)} \right)^2 + p_2, \quad (2-50)$$

where Q_{nz} is the flow rate going through the spear valve opening with effective flow area $A_{nz}(s_s)$ as a function of the spear position s_s . A discharge coefficient C_d is introduced since pressure losses due to geometry and flow regime at the nozzle exit are taken into account [60]. The discharge coefficient of an orifice is defined as the ratio between the vena contracta area and the orifice area [57]. The vena contracta is defined as the point where the stream lines become parallel after passing the orifice. Since data on the specific discharge efficiency is not available, a constant discharge coefficient is assumed of $C_d = 0.98$, which seems to be a realistic value based on data analysis studies performed in Harris [64].

A first order actuator model for the dynamic response of the spear position is proposed by Mulders et al. [28].

$$\dot{s} = \frac{1}{t_s} (s_{ref} - s) \quad (2-51)$$

In accordance to the work of Mulders et al. [28], an actuator time constant t_s of 1.69 for reference tracking is assumed.

2-6 Combined Drivetrain and Component Implementation

In the sections 2-2 to 2-5, modeling of the individual components of the DOT drivetrain is presented. The implementation of these components in MATLAB Simulink (R2018b) [94] is explained in this section. All these components are coupled in the modeling and simulation environment of Simulink, using the Simscape Toolbox [95].

All components described in the earlier sections of this chapter have to be linked together, forming the total hydraulic drivetrain model of the DOT wind turbine. For 'simple systems' as e.g. described by Equation 3-26 in the next chapter, this can be done analytically in a relatively easy way. A simple drivetrain model is derived where there is only a rotor coupled to a pump with a single pipe line, leading towards one single spear valve voor control of the line pressure, thus rotor speed. However, the DOT drivetrain concept considered in this thesis incorporates a RPS (S_1 and M_1) and extra internal nozzle (S_2) for power regeneration and compensation of flow shortage in the low pressure feed line, respectively. This low pressure feed line has its own fluid dynamics as well and is partly supplied with seawater by the pre-pressure pumps. Coupling of all the differential equations for such a highly complex system turned out to be an ambitious and cumbersome task, since the literature lacks explanations and descriptions for this type of problem. In the search for other possibilities, usability of the Simscape toolbox [95] for MATLAB Simulink became evident.

2-6-1 Simscape Component Implementation

The Simscape toolbox enables one to create models of physical systems within the Simulink environment. With Simscape, physical component models are built based on physical connections that directly integrate with block diagrams and other modeling paradigms. In this case, the Simscape toolbox is employed for integration of the hydraulic actuators, e.g. spear valves, pumps/motors, and pipe line dynamics.

The Simscape library contains hydraulic component blocks which are very useful for putting together the DOT drivetrain model. Those components are explained in more detail below. Appendix A-2 showcases a simplified version of the Simulink model to provide an easy understanding of how these Simscape component blocks are linked together. It also describes the communication blocks that are needed for communication between SimScape component blocks and conventional Simulink blocks.

Spear valves The spear valves are implemented by the 'Variable Orifice'-block. Figure 2-17a illustrates the Simscape component block, used for implementation of spear valves. Connections A and B are hydraulic conserving ports associated with the orifice inlet and outlet, respectively. Connection S is a physical signal port and represents the spear position of the spear valve. Regarding the components settings, a data table relating the spear position to the effective nozzle opening area is provided according to Equation 2-47. The interpolation method between these supplied data point is set at 'Linear'. The 'Leakage area' is left on the default value of 10^{-12} m². The 'Laminar flow pressure ratio' is set at 0.999 since fully turbulent flow is assumed.

Hydraulic pump The hydraulic pumps are implemented in the Simulink model by employment of the 'Fixed-Displacement Pump'-block. Figure 2-17b illustrates this Simscape

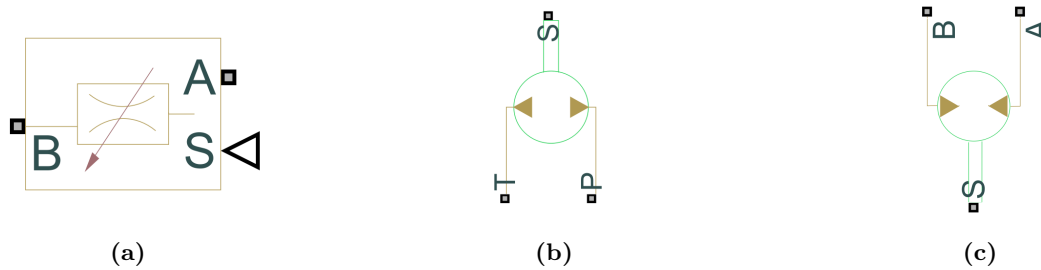


Figure 2-17: (a) Simscape component block, used for implementation of the spear valves in the combined drivetrain Simulink model. Connections A and B are hydraulic conserving ports associated with the orifice inlet and outlet, respectively. Connections S is a physical signal port and represents the spear position of the spear valve; (b) Simscape component block, used for implementation of the hydraulic pumps. Connections P and T are the hydraulic conserving ports associated with the pump outlet and inlet, respectively. Connections S is a mechanical rotational conserving port associated with the pump driving shaft; (c) Simscape component block, used for implementation of the hydraulic motor. Ports A and B are the hydraulic conserving ports associated with the motor inlet and outlet, respectively. Ports S is a mechanical rotational conserving port associated with the motor shaft.

component block. Connections P and T are the hydraulic conserving ports associated with the pump outlet and inlet, respectively. Connections S is a mechanical rotational conserving port associated with the pump driving shaft. Regarding the component settings, leakage and friction parameterization is implemented as 'Tabulated data - volumetric and mechanical efficiencies'. The 'pressure gain vector', 'Shaft angular velocity vector', 'Volumetric efficiency table' and 'Mechanical efficiency table' are constructed by the efficiency characteristics described in Sections 2-3-1 and 2-3-3 for the rotor pump and the pre-pressure pumps, respectively. The 'Pressure gain threshold for pump-motor transition' and 'Angular velocity threshold for pump-motor transition' is left on the defaults values of 1 bar and 10 rad s^{-1} , respectively.

Hydraulic motor The hydraulic motor is implemented in the Simulink model by employment of the 'Fixed-Displacement Motor'-block. Figure 2-17c illustrates the Simscape component. Ports A and B are the hydraulic conserving ports associated with the motor inlet and outlet, respectively. Ports S is a mechanical rotational conserving port associated with the motor shaft. Regarding the component settings, they are equal to those of the hydraulic pumps, described in the paragraph above.

Pipe lines The hydraulic pipe lines are implemented in the Simulink drivetrain model by employment of the 'Segmented Pipe LP'-blocks. Figure 2-18a illustrates this Simscape component block. Connections A and B are the hydraulic conserving ports. The block positive direction is from port A to port B. Regarding the component settings, each pipe has a internal pipe diameter of 0.1 m and total length of 30 m. Each pipe element consists of two pipe segments. The aggregate equivalent length of local resistances is assumed at 1 m. This parameter represents the total equivalent length of all local resistances associated with the pipe. It accounts for the pressure loss caused by local resistances, such as e.g. bends, fittings, armature and inlet/outlet losses. This length is added to the geometrical pipe length only for hydraulic resistance computation. Both the fluid volume and fluid inertia are determined based on pipe geometrical length only. The internal surface roughness height is assumed at $\epsilon = 4.5 \cdot 10^{-5} \text{ m}$, which is a conventional value for commercial steel pipes [97]. As proposed by White [55], the lower and upper Reynolds

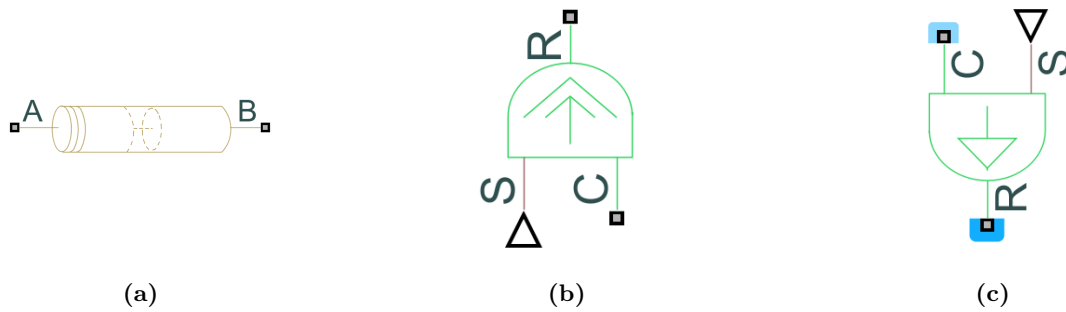


Figure 2-18: (a) Simscape component block used for implementation of the pipe lines in the combined drivetrain Simulink model. Connections A and B are the hydraulic conserving ports. The block positive direction is from port A to port B; (b) Simscape component block used for implementation of the ideal torque source. Connections R and C are the mechanical rotational conserving ports. Ports S is a physical signal port through which the control signal is applied; (c) Simscape component block used for implementation of the ideal rotational velocity source. Connections R and C are mechanical rotational conserving ports. Port S is a physical signal port through which the control signal is applied.

limit values for the transition region between laminar and turbulent flow are set to 2000 and 4000, respectively.

Ideal torque source The 'Ideal Torque Source'-block is implemented to simulate the torque demand of the generator that is coupled to the internal water motor. This component does not need any further settings. Figure 2-18b illustrates this Simscape component block. Connections R and C are the mechanical rotational conserving ports. Port C is connected to a ground, or 'Mechanical Rotational reference'-block. Ports S is a physical signal port through which the control signal is applied.

Ideal angular velocity source The 'Ideal angular velocity Source'-block is implemented to operate the pre-pressure pumps. The components directly feeds through a value in rad s^{-1} and does not need any further settings. Figure 2-18c illustrates this Simscape component block. Connections R and C are mechanical rotational conserving ports. Port C is connected to a ground, or 'Mechanical Rotational reference'-block. Port S is a physical signal port through which the control signal is applied.

Hydraulic pressure sensor The 'Hydraulic Pressure Sensor'-block represents an ideal hydraulic pressure sensor which converts a hydraulic pressure differential measured between two points into a physical control signal proportional to the pressure. Figure 2-19a illustrates this Simscape component block. Connections A and B are hydraulic conserving ports and connections P is a physical signal port. The sensor is oriented from A to B. For measurements of absolute pressure, port B is connected to a 'Hydraulic Reference'-block, described below.

Mechanical rotational reference The 'Mechanical Rotational Reference'-block represents a mechanical rotational reference point, that is, a frame or ground. It is used to connect mechanical rotational ports that are rigidly affixed to the frame (or ground). Figure 2-19b illustrates this Simscape component block.

Hydraulic reference The 'Hydraulic Reference'-block represents a connections to atmosphere. Is has only one hydraulic conserving port which should be connected to other

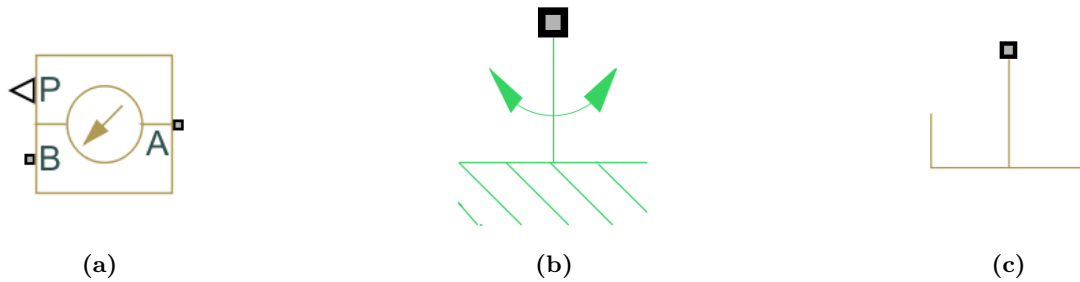


Figure 2-19: (a) Simscape component block used for implementation of pressure measurement devices in the combined drivetrain Simulink model. Connections A and B are hydraulic conserving ports and connection P is a physical signal port. The sensor is oriented from A to B; (b) Simscape component block used for implementation of a mechanical reference, or ground, and is considered a rigid connections to the 'world'; (c) Simscape component block used for implementation of a hydraulic reference, or ground. This block is used if absolute pressure are measured with respect to atmospheric pressure.

component block that are considered directly connected to the atmosphere. Figure 2-19c illustrates this Simscape component block.

2-6-2 Defining model inputs and outputs

The aforementioned components are implemented into a fully combined drivetrain Simulink model. This non-linear model will be linearized at different operation points for controller design, which will be elaborated on in the next chapter. Therefore, inputs and outputs for the system linearization should be defined first.

Figure 2-20 illustrates again a schematic of the DOT hydraulic drivetrain; this time it illustrates the inputs and outputs which are used for controller design later. The inputs of this drivetrain Simulink model are defined as the local wind speed U_r , the rotational speed ω_{pp} of the pre-pressure pumps, the torque demand τ_{M1} excited on the internal water motor and the three spear position references $s_{i,ref}$. The outputs are defined as the pressure differential Δp_r across the rotor pump, the pressure p_{fl} at the upper side of the low-pressure feed line and the rotational speed ω_{M1} of the internal water motor. The difference in elevation h_t between pipe entry and exit is 30 m for each individual pipe line.

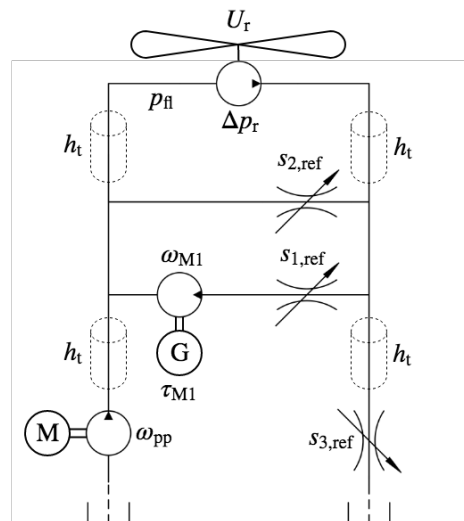


Figure 2-20: Schematic of the DOT hydraulic drivetrain with the inputs and outputs indicated. The inputs of the drivetrain model are defined as the local wind speed U_r , the rotational speed ω_{pp} of the pre-pressure pumps, the torque demand τ_{M1} excited on the internal water motor and the three spear position references $s_{i,ref}$. The outputs of the drivetrain model are defined as the pressure differential Δp_r across the rotor pump, the pressure p_{fl} at the upper side of the low-pressure feed line and the rotational speed ω_{M1} of the internal water motor. The difference in elevation h_t between pipe entry and exit is 30 m for each individual pipe line.



Chapter 3

Control Strategy & Design

This chapter elaborates on the control strategy and the controller design of the Delft Offshore Turbine (DOT) wind turbine with hydraulic drivetrain and Regenerative Power System (RPS). To start with, control of conventional wind turbine is analyzed and described extensively in Section 3-1. Most commonly used top-level control strategies will be discussed and one is chosen as a foundation of the DOT control strategy. Hereafter, Section 3-2 translates the chosen Optimal Torque Control (OTC) strategy into a Optimal Pressure Control (OPC) strategy. Section 3-3 describes technical improvements of the DOT drivetrain such that higher drivetrain efficiencies could be obtained. Section 3-4 describes the control strategy and control specifications which will be used for controller evaluation in Chapter 4. Thereupon, Section 3-5 describes the linearization of a non-linear model and one single operation point of the DOT wind turbine is presented which is used as an example for further control design. In Section 3-6, an analysis is performed on rotor stall stability, leading towards an extra stability criterion for later control design. Hereafter, Section 3-7 presents a Relative Gain Array (RGA) analysis to make an assessment on the interaction between the in- and output of the drivetrain model. Lastly, Section 3-8 presents the process of loop-shaping controller design. Controllers are designed for multiple operation points, and an interpolated gain-scheduling strategy is presented.

3-1: Control of Conventional Wind Turbines	40
3-2: Optimal Pressure Control Strategy	43
3-3: Future Improvements	49
3-4: Control strategy and specifications	51
3-5: System linearization	52
3-6: Rotor stall stability analysis	54
3-7: Relative Gain Array analysis	59
3-8: SISO Control Design using Interpolated Gain Scheduling	62

3-1 Control of Conventional Wind Turbines

This section presents a brief overview of conventional wind turbine control strategies. One is chosen as the foundation for controller design of the DOT wind turbine.

Generally, the focus of the control objectives differ depending on the operating conditions of the wind turbine, which is usually divided in 4 regions.

- **Region 1:** The wind speed is below the cut-in wind speed. In this region the wind turbine is usually kept at a standstill by supervisory control. The cut-in wind speed is determined by the production of electrical energy relative to the energy losses during operation which it should at least compensate for [3].
- **Region 2:** The turbine operates in the partial-load regime. It is referred to as the below-rated region and is located between the cut-in and the rated speed. In this region, the main goal is to maximize power production by operating the rotor at maximum efficiency. For variable speed wind turbines, this is usually achieved through torque control [3].
- **Region 3:** The turbine operates in the full load regime and is the so-called above-rated region. In contrast to region 2, in the above-rated region power production is limited to make sure that no excessive loads occur on the wind turbine [3][4]. For variable pitch wind turbines, this is mostly achieved by employment of Collective Pitch Control (CPC). Aerodynamic rotor characteristics and efficiency are altered by pitching the blades 'away' from their fine-pitch angle, which is their most efficient pitch angle [42].
- **Region 4:** A region of excessive wind speeds above the cut-out wind speed. In this region, the wind turbine is shut down by supervisory control [3].

As earlier mentioned in Section 2-2, rotor efficiency is maximized for operation at the maximum power coefficient $C_{p,max}$. This depends both on operating on the optimum pitch angle, or fine-pitch angle β_0 , and optimal Tip-Speed Ratio (TSR) λ_0 . During operation in region 2, therefore, rotor speed should be controlled such that the optimal TSR is maintained for maximum power production. Rotor speed can be controlled by employment of various Maximum Power Point Tracking (MPPT) strategies. Those strategies are usually based on control of the generator torque demand, which is from here referred to as 'system torque'.

In contrast to region 2, the objective of region 3 is to no longer maximize power production, but to limit it by regulating rotor speed and torque. Generally, generator torque is kept constant while pitch control of the rotor blades is employed to reduce aerodynamic efficiency.

For this thesis, region 2 (below-rated domain) is of interest since turbine control in this region is mainly achieved through control of the system torque. MPPT algorithms of conventional wind turbines are categorized into four types: Optimum TSR control, Optimal Torque Control (OTC), Power Signal Feedback (PSF) control and Hill Climb Search (HCS) control [81].

Optimum TSR control is rarely applied. It requires measurements or an estimation of the rotor effective wind speed, but acquiring an accurate value of the rotor effective wind speed is generally difficult with nacelle-top anemometry.

Optimal Torque Control consists of a feed forward control law based on rotor speed without any knowledge of the prevailing wind speed. A feedback controller is used to make sure that the generator tracks the torque reference obtained from the feed forward law. Turbine characteristics and measurements of generator speed are indispensable for this approach. Assuming steady-state turbine operation at e.g. maximum power efficiency, the power coefficient is maximized at $C_{p,\max}$ for an optimum TSR λ_0 . The power produced is then

$$P_{\text{opt}} = \frac{\rho_{\text{air}}\pi R^5 C_{p,\max}}{2\lambda_0^3} \omega_r^3 = K_{\text{opt}}\omega_r^3, \quad (3-1)$$

where K_{opt} is defined as the **Optimal Mode Gain** in $\text{Nm s}^2 \text{rad}^{-3}$. Using the relation $\tau_r = P_r/\omega_r$, this optimal power law can be written as a torque law. OTC relies on imposing the generator torque demand according to this quadratic optimal power law

$$\tau_{\text{opt}} = \frac{\rho_{\text{air}}\pi R^5 C_{p,\max}}{2\lambda_0^3} \omega_r^2 = K_{\text{opt}}\omega_r^2. \quad (3-2)$$

By measuring the rotor speed, tracking of the maximum power coefficient $C_{p,\max}$, thus maximum rotor efficiency, can be achieved for below-rated operation. The control diagram of OTC is depicted in Figure 3-1a.

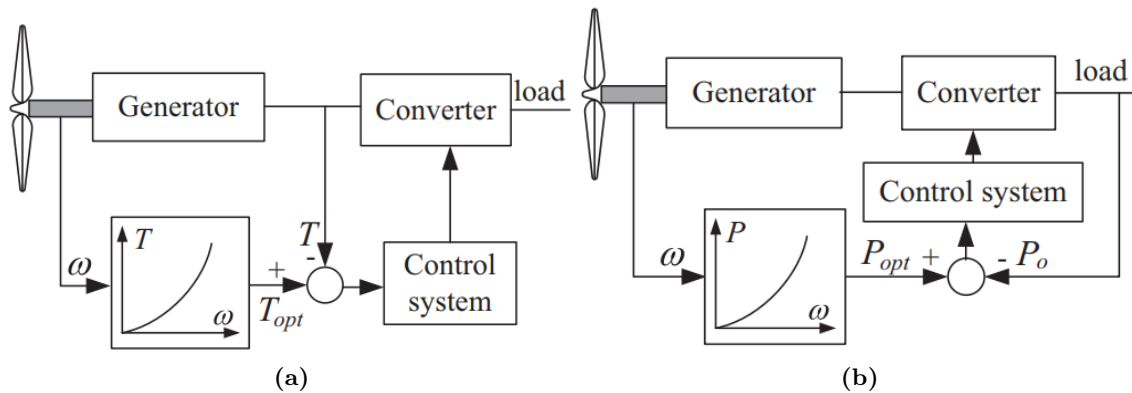


Figure 3-1: (a) OTC control diagram. The Optimal Mode Gain K_{opt} describes the feed forward torque law. By means of a feedback control loop, this torque reference is tracked by the power electronic components inside the wind turbine [81]; (b) PSF control diagram. The Optimal Mode Gain K_{opt} describes the feed forward power law. By means of a feedback control loop, this power reference is tracked by the power electronic components inside the wind turbine [81].

This traditional and widely used control method has its drawbacks. The blades' aerodynamic conditions change over time due to wear, tear and fouling, and hence the value for K_{opt} can change during turbine operation which brings uncertainties into the system. This could result in a wind turbine that is operating off its maximum rotor efficiency [80][81].

Figure 3-1b shows the control diagram of **Power Signal Feedback** control. It looks quite similar to the OTC control diagram, however, instead of tracking optimal torque, an optimal power curve is used. The control law of Equation 3-1 could be used or data obtained during performance tests [80][81].

The last category of MPPT algorithms, discussed in this section is **Hill Climb Search**. This model-free method is quite robust and does not depend on priori knowledge of the wind turbine's characteristics [80]. Neither optimal power coefficient nor optimal TSR needs to be known, in contrast to the aforementioned MPPT strategies. This MPPT approach can be employed by perturbing the generator torque which result in a speed variation $\Delta\omega_r$. By observing the resulting increase or decrease in power ΔP it can be concluded whether the perturbation was in the right direction or not. If the perturbation results in a decrease of power, the perturbation is reversed in order to track in the direction of increasing power [85]. This is possible since the relation between tracked power and rotor speed has a parabolic, thus convex allure. Due to its characteristics, this method is also known as Perturb and Observe (P&O) [80]. The main concern of this method is the way the perturbation is excited onto the system. Weak perturbations will result in slow responses and incapability of tracking the exact maximum power point under rapidly varying wind speed. More aggressive perturbation may lead to instability [86] or will at least amplify the oscillations around the maximum power point. Yaoqin et al. [87] implemented the HCS method with variable step perturbation, proportional to the derivative $dP/d\omega_r$ of the power curve. However, this method only works well when a change in rotor speed can be measured quite instantly, which requires the rotor inertia to be significantly low [80].

This gradient search approach knows a few variations, of which one goes by the name of **Extremum Seeking Control (ESC)** [74]. ESC is a model-free real-time set-point optimization algorithm built upon the gradient search scheme. A major class of ESC algorithms estimates the online gradient by using a pair of dither and demodulation signals in combination with proper filtering, and the optimality is achieved by closing the control loop via integral action. A distinctive advantage of this strategy with respect to conventional HCS is that the gradient extraction process is locked to the harmonics of dither frequencies, which results in two benefits. Firstly, the search process is decoupled from the change due to exogenous disturbance (e.g. wind fluctuations) and/or process variations, provided that significant signal-to-noise ratio is present in the dithered output. Secondly multiple-input ESC can be easily realized by assigning different dither frequencies to different input channels. Due to such advantages, ESC has drawn the wind industry's attention as a potential MPPT strategy for below-rated turbine control (region 2).

Conclusion:

Since one of the future goals of Delft Offshore Turbine is to increase the size of its hydraulic wind turbines, it is inevitable that rotor inertia's will increase. Besides that, power generation takes place at a centralized hydro power unit at a considerable distance from one individual wind turbine. Individual turbine control based on collective power production therefore, invalidates the potential for both PSF control or a gradient search algorithm as HCS or ESC. Therefore, OTC will be used as a foundation of the Delft Offshore Turbine (DOT) MPPT strategy. This strategy will be elaborated on more deeply in the next section where this strategy is translated to an Optimal Pressure Control (OPC) MPPT strategy.

3-2 Optimal Pressure Control Strategy

This section proposes a control strategy for the DOT wind turbine in the below-rated operational region (region 2). Drivetrain efficiency and an feasibility analysis on the Regenerative Power System system are considered for determination of the control strategy. This sections ends with a couple of control specifications.

The relation between rotor torque, wind speed and the rotational speed of the rotor was defined by Equation 2-7. The assumption that the rotor is operating at the most efficient TSR during below-rated operation leads to Equation 3-2, where the rotor torque and rotational speed of the rotor were related by the Optimal Mode Gain. Adjusting the system torque according to this optimal quadratic law ideally results in operation at maximum rotor efficiency. Substitution of Equation 3-2 in Equation 2-16 now relates the pressure differential Δp_r across the rotor pump to the rotational speed ω_r of the rotor, ideally resulting in an equal system torque excited onto the rotor. This relation is defined as

$$\Delta p_{r,opt} = \frac{\tau_{opt} \eta_{m,r}(\omega_r, \Delta p_r)}{V_r} = \frac{K_{opt}}{V_r} \eta_{m,r}(\omega_r, \Delta p_r) \omega_r^2. \quad (3-3)$$

Regulation of the pressure differential across the rotor pump according to this new pressure law for below-rated operation results in maximum rotor efficiency. Assuming operation along $\Delta p_{r,opt}$, Δp_r is directly related to rotor speed ω_r . Since the ratio between rotor speed ω_r and pump speed ω_p is fixed, the pump's mechanical efficiency $\eta_{m,p}(\omega_p, \Delta p_p)$ becomes only dependent of the rotor speed. Therefore, Equation 3-3 can be rewritten as

$$\Delta p_{r,opt} = K_{opt}^p(\omega_r) \omega_r^2, \quad (3-4)$$

where K_{opt}^p will be referred to as the **Optimal Pressure Gain**.

Until here, optimal rotor efficiency is used as a general case. However, optimal rotor efficiency will not necessarily result in an optimized total drivetrain efficiency. Taking total drivetrain efficiency into account, alternative optimal pressure paths Δp_{opt} could be derived. For convenience, this section considers two cases, namely, below-rated operation at $C_{p,max}$ and at $C_{\tau,max}$. Figure 3-2a depicts the rotor torque paths for operation at $C_{\tau,max}$ and $C_{p,max}$ with red and blue, respectively. These paths describe the relation between rotor torque and the rotational speed of the rotor, as defined in Equation 3-2. Using Equation 2-19, these rotor torque paths are converted to pressure differential paths, as defined in Equation 3-4. Figure 3-2b depicts the rotor pump pressure differential paths for operation at $C_{\tau,max}$ and $C_{p,max}$ with red and blue, respectively.

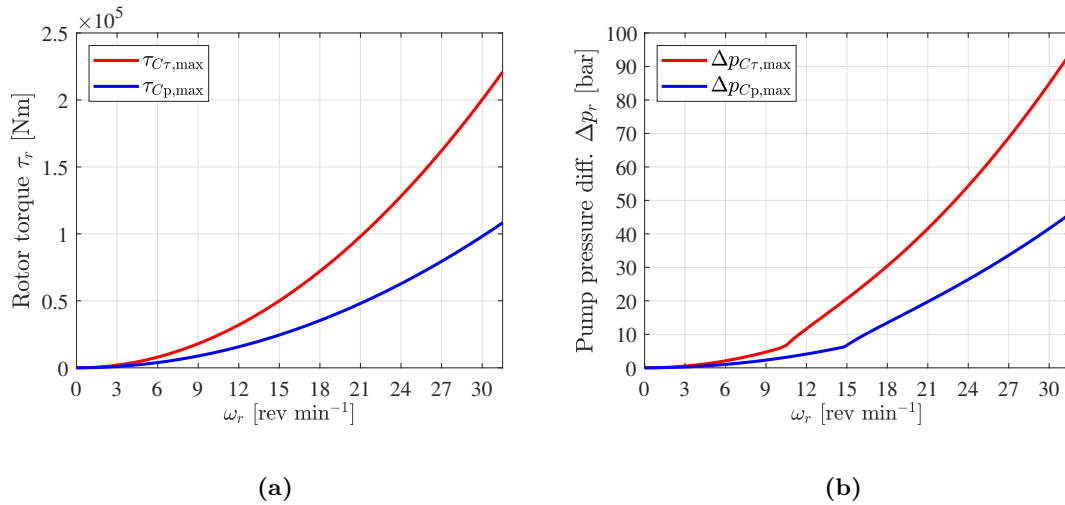


Figure 3-2: (a) Rotor torque paths as function of the rotor rotational speed ω_r for operation at $C_{\tau,max}$ and $C_{p,max}$, depicted in red and blue respectively; (b) Rotor pump pressure differential paths as function of the rotor rotational speed ω_r for operation at $C_{\tau,max}$ and $C_{p,max}$, depicted in red and blue respectively.

It is observed that operation at $C_{\tau,max}$ results in a faster increasing pressure differential Δp_r across the rotor pumps. This has influence on drivetrain efficiency since e.g. the rotor pump has an increasing mechanical efficiency for increasing pressure differentials, as described in Section 2-3-1. Besides rotor efficiency, what is the optimal path for overall drivetrain efficiency? Furthermore, operation of the pre-pressure pumps is limited by the maximum amount of electrical power, extracted by the Regenerative Power System (RPS). This effects overall drivetrain efficiency since less flow being directed to the Pelton turbine leads to reduced power production of the wind turbine. These two aspects are analyzed in the two subsequent subsections.

3-2-1 Power generation of the Regenerative Power System

The set of two pre-pressure pumps together need an electrical power supply of 40 kW for operation at maximum rotational speed ω_{pp} . As mentioned in Section 2-3-3, this power demand is assumed linearly proportional to their rotational speed. In order to be completely self-sustainable, the power demand of the pre-pressure pumps need to be regenerated by the RPS, illustrated in Figure 3-3. The regenerated power is dependent of the rotational speed of the internal water motor and the generator torque demand (of the generator G) as $P_{M1} = \omega_{M1}\tau_{M1}$. Losses between the internal water motor and generator are neglected. The rotational speed ω_{M1} relates to the flow through the RPS, and the amount of torque τ_{M1} which can be demanded by the generator, completely depends on the hydraulic torque that is available. The available hydraulic torque of the internal water motor is related to the pressure dif-

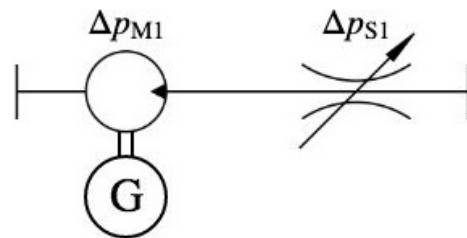


Figure 3-3: Schematic of the RPS of the DOT drivetrain. The pressure differential across spear valve S_1 is represented by Δp_{S1} and the pressure differential across water motor M_1 by Δp_{M1} . For convenience of this analysis, the total pressure differential across the RPS is assumed equal to the pressure differential across the rotor pump.

ferential across it, defined by Equation 2-20.

As will be illustrated further in this section, it is desirable to maximize the power generation of the RPS for operation of the pre-pressure pumps. Therefore, flow through the RPS is maintained constant at its maximum value. Due to the volumetric displacement and the maximum rotational speed of the internal water motor, the RPS deals with a flow of 350 l min^{-1} at a constant rotational speed ω_{M1} of $1555 \text{ rev min}^{-1}$. The attainable regenerated power is thus dependent on the maximum attainable pressure differential across the internal water motor. For convenience of this analysis, the pressure differential across the RPS is assumed equal to the pressure differential Δp_r across the rotor pump.

For generation of 40 kW and a rotational speed of $1555 \text{ rev min}^{-1}$, a generator torque demand τ_{M1} of 250 Nm is needed. According to Equation 2-20, this can only be achieved for a pressure differential Δp_{M1} of 80 bar. However, as Figure 3-2b illustrates, this pressure differential can only be achieved in a small section of the below-rated operational domain for operation at $C_{\tau, \max}$. For operation at $C_{p, \max}$, this pressure differential is not reached at all. But how does this translate to operation of the pre-pressure pumps, considering self-sustainability (and no external electrical power source)?

As mentioned before, the pressure differential across the total RPS is assumed equal to the pressure differential across the rotor pump $\Delta p_{M1} + \Delta p_{S1} = \Delta p_r$. Subtracting the hydraulic loss of spear valve S_1 results in the maximum attainable pressure differential across the internal water motor. For operation at $C_{\tau, \max}$ and $C_{p, \max}$, the respective Figures 3-4a and 3-5a illustrate the maximum attainable pressure differentials Δp_{M1} across the internal water motor with the red solid lines.

The minimum hydraulic pressure loss Δp_{S1} caused by the spear valve is achieved with the maximum spear position for a maximized effective opening area of the spear valve. However, operation of the spear near to its maximum position puts controllability of the RPS at risk since actuator limits will be reached sooner during e.g. disturbance rejection.

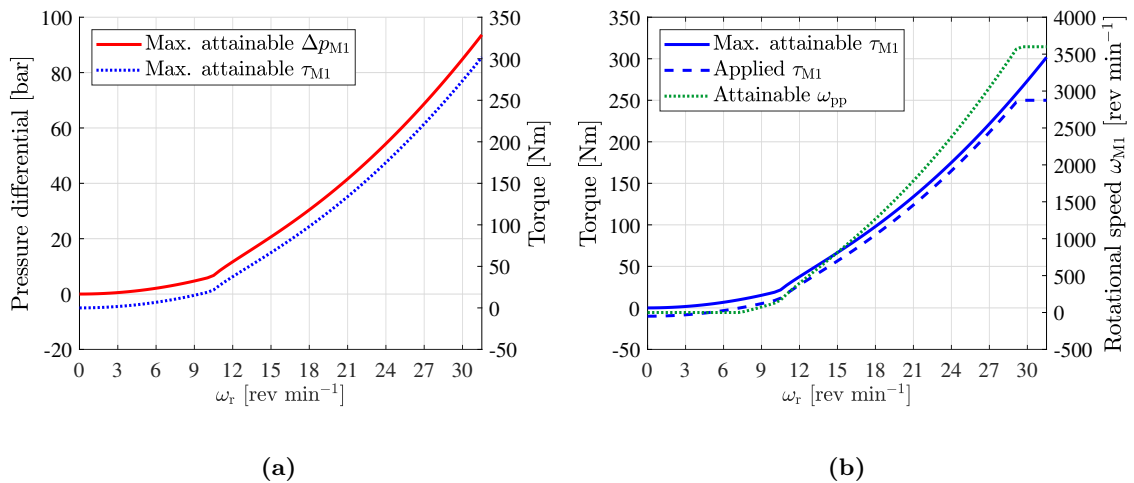


Figure 3-4: For operation at $C_{\tau, \max}$: (a) Maximum attainable pressure differential across the internal water motor, indicated by the solid red. The blue dotted line indicates the maximum torque demand τ_{M1} that can be excited onto the internal water motor; (b) The solid blue line indicates the maximum torque demand τ_{M1} again, and is equal to the blue dotted line in figure (a). The blue dotted line in this figure denotes the actual, applied torque τ_{M1} , which is chosen 10 Nm lower than the maximum attainable torque as a safety margin. The green dotted line shows the maximum attainable rotational speed of the pre-pressure pumps.

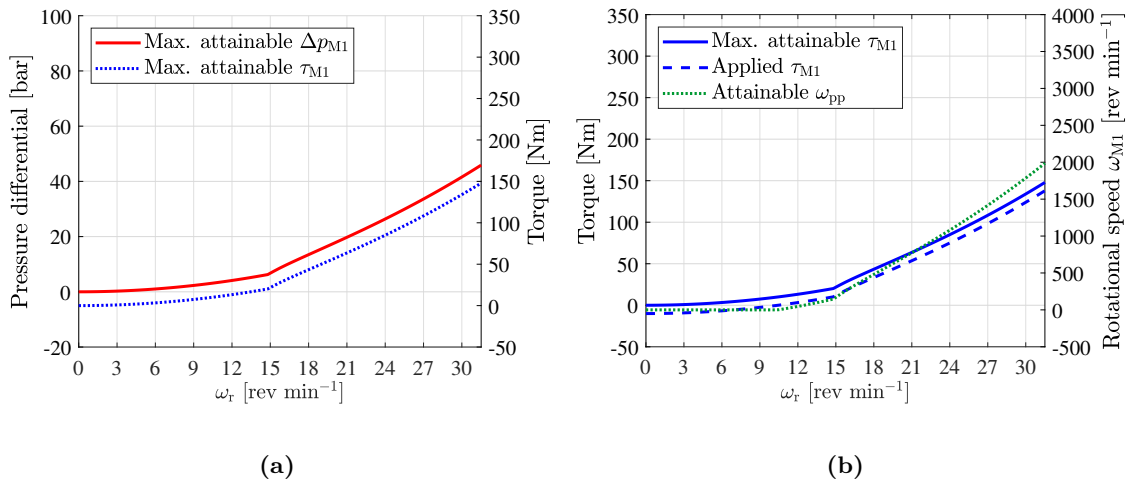


Figure 3-5: For operation at $C_{p,\max}$: **(a)** Maximum attainable pressure differential across the internal water motor, indicated by the solid red. The blue dotted line indicates the maximum torque demand τ_{M1} that can be excited onto the internal water motor; **(b)** The solid blue line indicates the maximum torque demand τ_{M1} again, and is equal to the blue dotted line in figure (a). The blue dotted line in this figure denotes the actual, applied torque τ_{M1} , which is chosen 10 Nm lower than the maximum attainable torque as a safety margin. The green dotted line shows the maximum attainable rotational speed of the pre-pressure pumps.

To prevent this occurrence, there is accounted for a pressure loss over the spear valve that is opened for 80 %. This safety margin makes sure that the spear valve is able to account for disturbance rejection such that the rotational speed of the internal water motor can be regulated at all times. The pressure loss of the spear valve (80 % opened) for a flow rate of 350 l min^{-1} is approximately 1 bar. The blue dotted lines in the Figures 3-4a and 3-5a indicate the maximum allowable torque demand τ_{M1} that can be excited onto the internal water motor, derived by Equation 2-20.

Because the internal water motor is operated at constant rotational speed, the torque demand τ_{M1} is assumed linearly proportional to the pre-pressure pump rotational speed as $[0 - \tau_{M1,\max}] \sim [0 - \omega_{pp,\max}]$. For operation at $C_{\tau,\max}$ and $C_{p,\max}$, the respective Figures 3-4b and 3-5b illustrate the maximum torque demand τ_{M1} on the internal water motor denoted by the blue solid line. The blue dotted lines in these figures denote the actual applied torque τ_{M1} , which is chosen 10 Nm lower than the maximum attainable torque as a safety margin. The green dotted lines in both figures show the maximum attainable rotational speed of the pre-pressure pumps.

It can be easily concluded that for operation at $C_{\tau,\max}$ the pre-pressure pumps can only reach their maximum rotational speeds for a really small part of the below-rated operational domain. For operation at $C_{p,\max}$, this maximum rotational speed is not even achieved at all. If the pre-pressure pumps deliver less flow, less flow is supplied to the Pelton Turbine. This leads to a lower power production, resulting in a lower drivetrain efficiency. The next section elaborates on the drivetrain efficiency for operation at both $C_{\tau,\max}$ and $C_{p,\max}$.

3-2-2 Drivetrain Efficiency

In the previous subsection, operation of the pre-pressure pumps is analyzed. A big difference between operation at $C_{\tau,\max}$ and $C_{p,\max}$ is discovered in terms of maximum attainable power extraction by the RPS. For both cases, the rotor speed is related to the pressure differential across the rotor pump, thus the RPS. This was translated to a maximum attainable rotational speed of the pre-pressure pumps. Supplying these pre-pressure pumps with sufficient electrical power such that higher flow rates towards the Pelton turbine can be realized turns out to be crucial for overall drivetrain efficiency, as will be described below.

Overall drivetrain efficiency is defined as the power generated by the wind turbine divided by the wind power that was available at that time. However, instead of electrical power output, hydraulic power output is considered since no data is available about Pelton turbine efficiency. Besides that, the efficiency of Pelton turbines is generally high and dependent of the percentage of input flow with respect to the maximum flow [51]. Figure 3-6 illustrates that the efficiency of a Pelton turbine with one spear valve jet approaches maximum efficiency for relatively low flows. Moreover, Brekke [51] states operation of a Pelton turbine with multiple spear valve jets experiences reaches its maximum efficiency over a wider flow range. Therefore, the Pelton turbine should be dimensioned such that maximum Pelton efficiency occurs throughout a big part of the below-rated operational domain. Jarquin [52] describes an optimal torque control strategy of the generator that is coupled to such a Pelton turbine. This control strategy is used to control the ratio between the spear valve jet velocity and the rotational speed of the Pelton wheel, such that the maximum attainable Pelton efficiency is reached. Since the Pelton efficiency is high and constant for a wide range of flows, hydraulic power will be used in this thesis to determine drivetrain efficiency.

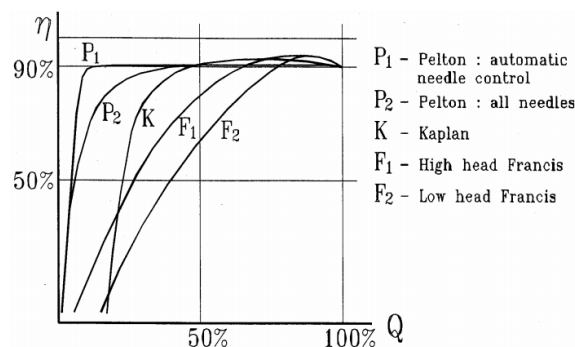


Figure 3-6: Comparison of efficiency of different hydraulic turbine types [51]

Figure 3-7 illustrates a simplified schematic of the energy flows in the DOT wind turbine. The wind enters the system with power P_{wind} and leaves the system with hydraulic power P_{hydro} . In between, the rotor losses are denoted as $P_{r,\text{loss}}$ and the drivetrain losses as $P_{\text{sys},\text{loss}}$. As presented in Section 3-2-1, the maximum attainable rotational speed of the pre-pressure pumps is limited by the amount of regenerated electrical power. Lower operating speeds of the pre-pressure pumps result in decreased flows of seawater towards the Pelton turbine. Instead, more flow will go through spear valve S_2 , compensating for the flow shortage in the low-pressure feed line. From Figures 3-4b and 3-5b, it is concluded that the flow of seawater towards the Pelton turbine is higher for operation at $C_{\tau,\max}$, together

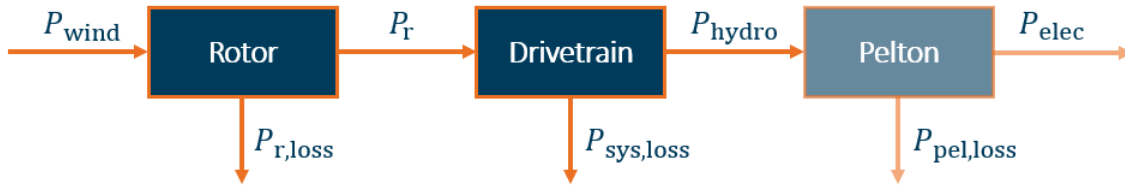


Figure 3-7: Block diagram, illustrating the energy flows of the DOT wind turbine drivetrain. The wind enters the system with power P_{wind} and leaves the system with hydraulic power P_{hydro} . In between, losses occur at the rotor and in the drivetrain, denoted as $P_{\text{r,loss}}$ and $P_{\text{sys,loss}}$, respectively.

with a faster increasing discharge pressure as well. Evidently, operation at $C_{\tau,\text{max}}$ results in a much higher amount of power P_{hydro} going to the Pelton turbine, resulting in a much higher drivetrain efficiency during below-rated operation.

Figure 3-8 illustrates both the drivetrain efficiency and total efficiency of the DOT wind turbine, considering operation at $C_{\tau,\text{max}}$ and $C_{\text{p,max}}$. The drivetrain efficiency does not include rotor losses, as the total efficiency does. The drivetrain loss $P_{\text{sys,loss}}$ incorporates the energy loss caused by seawater that is flowing back through the RPS and the extra internal spear valve S_2 , and the volumetric and mechanical losses of the pre-pressure pumps, the internal water motor and rotor pump. Combining the maximum attainable speed of the pre-pressure pumps and the discharge pressure of the spear valve that is leading towards the Pelton wheel, the hydraulic power output P_{hydro} can be determined as a function of the rotor rotational speed. The wind power is defined as

$$P_{\text{wind}} = \frac{1}{2} \rho_{\text{air}} \pi R^2 U_r^3. \quad (3-5)$$

Dividing the hydraulic power output by P_{wind} , the total efficiency of the DOT wind turbine is determined. Dividing this total efficiency by C_{p} , the drivetrain efficiency is isolated. It can be concluded that the drivetrain efficiency is much higher for operation at $C_{\tau,\text{max}}$. For controller design in the following sections therefore, only operation at $C_{\tau,\text{max}}$ is considered.

Before that, a couple of improvements are proposed in the next section, since drivetrain efficiency is relatively low compared to drivetrains of conventional wind turbines.

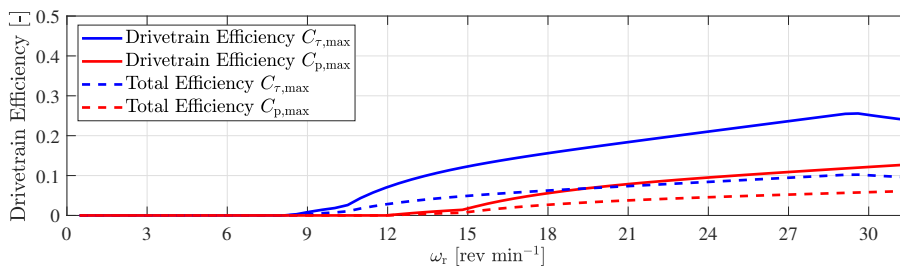


Figure 3-8: Comparison of drivetrain and total turbine efficiency for operation at $C_{\tau,\text{max}}$ and $C_{\text{p,max}}$. The drivetrain efficiencies as function of the rotor rotational speed are represented by the solid lines. The dotted lines represent the total turbine efficiencies, adding the rotor efficiency to the drivetrain efficiency.

3-3 Future Improvements

Considering operation at $C_{\tau,\max}$, the drivetrain efficiency is fairly low as concluded in the previous subsection. This is mainly due to the low amount of regenerated power of the RPS, allowing the pre-pressure pumps to only operate at fairly low rotational speeds throughout the whole below-rated operational domain. This results in low flow rates of seawater heading towards the Pelton turbine. In addition to that, at their maximum speed, the two pre-pressure pumps are only covering for a percentage (max. 27 %) of the seawater flow needed at the rotor pump. Figure 3-8 shows a maximum efficiency peak at a rotor rotational speed of $29.1 \text{ rev min}^{-1}$, which coincides with the moment that the pre-pressure pumps reach their maximum rotational speed, as shown in Figure 3-4b. For this rotor speed, the seawater flow through the rotor pump is approximately 3500 l min^{-1} . Dividing the amount of flow delivered by the pre-pressure pumps (approximately equal to the flow towards the Pelton wheel) by this rotor pump flow results in a theoretical drivetrain efficiency limit of $\approx 27 \%$. Evidently, increasing the pre-pressure pump flow relative to the rotor pump flow, would result in a higher drivetrain efficiency. Just by scaling up the pre-pressure pump's dimensions, however, the issue is that sufficient electrical energy must be available for operation of the pre-pressure pumps, and in the current case this is already an issue.

More power generation of the RPS can be achieved either by increasing the pressure differential across the rotor pump or by employment of an internal water motor with a larger volumetric displacement V_{M1} . Let's have a closer look.

3-3-1 Decreasing transmission ratio between rotor and rotor pump

The first case can be realized by adjusting the transmission ratio of the hydraulic rotor pump. Let's consider a gearbox ratio of half the size for example. This would result in a rotor pump that demands half the flow, but twice the pressure differential, compared to the current drivetrain set-up presented earlier. This brings a couple of advantages. First of all, the pressure differential increases, resulting in an increased attainable torque over the internal water motor. Therefore, more electrical energy can be extracted by the RPS for lower rotational speeds of the rotor. This allows the pre-pressure pumps to operate at their maximum speed over a wider range of rotor speeds, as illustrated in Figure 3-9a. Secondly, since only half the flow is demanded by the rotor pump with respect to the current rotor pump, less seawater has to flow back from the high pressure discharge line to the low-pressure feed line through spear valve S_2 . Because the pre-pressure pumps deliver a relatively larger part of the flow need at the rotor pump now, the efficiency limit increases significantly. This is illustrated in Figure 3-9b.

3-3-2 Increased volumetric displacement of the water motor

If the volumetric displacement V_p of the internal water motor is increased, larger torques on the internal water motor can be attained, which as a result increases the maximum attainable power generation of the RPS (assuming the same rotational speed ω_{M1} as before, thus an increased flow through the RPS). In the original concept, the flow of seawater going through spear valve S_2 is large compared to the flow going through the RPS. Increasing the volumetric displacement of the water motor of the RPS shifts this ratio and results

in increased power regeneration (and less hydraulic energy loss through spear valve S_2). Figure 3-10a illustrates the result of employing an internal water motor with a larger volumetric displacement. To clearly show the differences, a water motor with a volumetric displacement twice as large (0.450 l rev^{-1}) is chosen. It can be concluded that the pre-pressure pumps can reach their maximum speed at a lower rotational speed of the rotor. Consequently, Figure 3-10b shows a slightly higher efficiency peak compared to Figure 3-8. The peak is located at a lower rotational speed of the rotor since this point, again, coincides with the moment where the pre-pressure pumps reach their maximum speed. However, for higher rotational speeds of the rotor, the amount of seawater heading towards the Pelton wheel is equal to that of the current set-up. Therefore, comparing Figures 3-8 and 3-10b, drivetrain efficiency follows a similar path after the point where the pre-pressure pumps

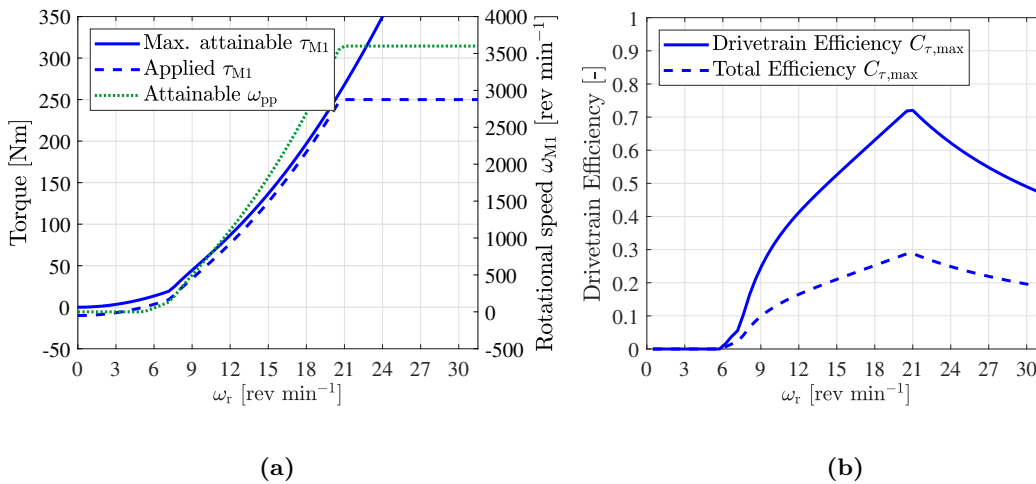


Figure 3-9: Half the transmission ratio between the rotor and the rotor pump asks for higher pressure differentials across the rotor pump. Figure (a) shows the maximum attainable and applied torque demand of the generator coupled to the internal water motor. Figure (b) shows that the drivetrain efficiency becomes much higher, compared to the efficiency of the current set-up illustrated in Figure 3-8.

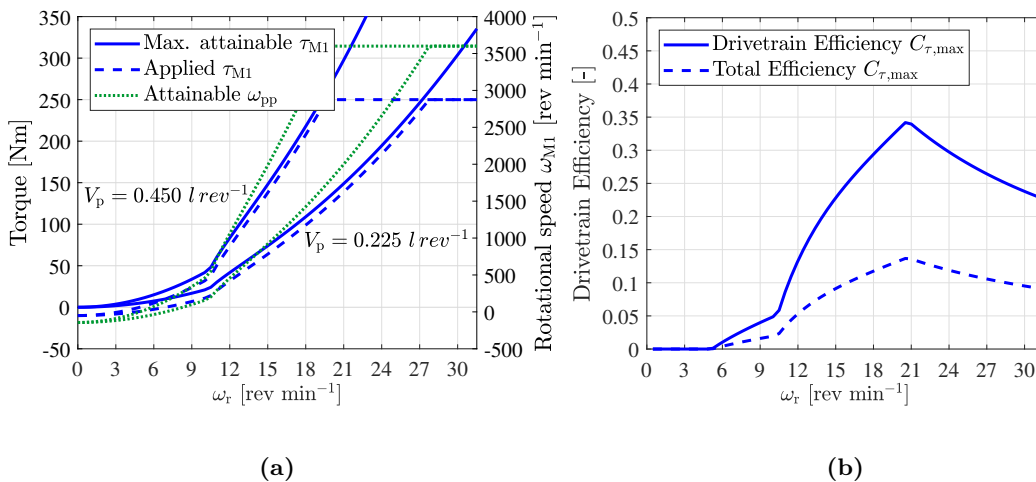


Figure 3-10: Figure (a) considers two cases. An internal water motor with the current volumetric displacement V_p of 0.225 l rev^{-1} , and an internal water motor with twice that volumetric displacement. It shows the maximum attainable and applied torque demand of the generator coupled to the internal water motor for both cases. Figure (b) shows the total and drivetrain efficiency for the case with $V_p = 0.450 \text{ l rev}^{-1}$.

3-4 Control strategy and specifications

This section briefly presents the controller specifications for further controller design within the next sections of this chapter

In Section 3-2, an analysis on the drivetrain efficiency and the power generation capabilities of the RPS was presented. Based on this analysis, it was concluded that operating at $C_{\tau, \max}$ is best for the current drivetrain set-up. For further controller design, operation points along the optimal pressure gain path are chosen. However, besides an optimal pressure differential Δp_r across the rotor pump as function of the rotor speed, a couple of other specifications are introduced. An automated optimization procedure is used to find the operation points conforming the specifications below.

- For every wind speed, the rotational speed of the rotor and the pressure differential across the rotor pump P_r are related according to the optimal pressure gain.
- The feed line pressure p_{fl} in front of the rotor pumps has to be at least 1 bar to prevent cavitation in the pump cylinders. To make sure that the rotor pump boost/intake pressure never drops below 1 bar due to e.g. wind disturbances, the control reference is set to 5 bar in the whole operational domain.
- The rotational speed of the internal water motor M_1 has to be controlled to $1555 \text{ rev min}^{-1}$ in the whole operational domain. How much electrical power is generated by the RPS is determined by the torque demand τ_{M1} , excited onto the internal water motor.
- The DOT wind turbine should be self-sustainable such that electrical power supply from the grid is unnecessary. Therefore, the power extracted by the RPS is maximized throughout the whole operational region. This means that generator torque demand τ_{M1} follows the blue dotted line of Figure 3-4b as a function of the rotational speed of the rotor. It is assumed that slight deficits of regenerated power meant for operation of the pre-pressure pumps, caused by wind fluctuations, don't influence operation of the pre-pressure pumps.
- In addition to the previous specification, the rotational speed of the pre-pressure pumps are a function of the rotor rotational speed according to the green dotted line in Figure 3-4b.

3-5 System linearization

This section presents the operation points that are used for controller design. It describes in what form the linearized systems are extracted from the non-linear Simulink model. An operation point is presented which will be used to illustrate the system analysis and controller design in the following sections.

After defining the model in- and outputs in Section 2-6-2 and having determined the operation points according to the specifications of Section 3-4, the non-linear Simulink Simscape model is linearized for extraction of Linear Time Invariant (LTI) State-Space models. A set of non-linear differential equations $f(x, u)$ describing the drivetrain dynamics are linearized as

$$\hat{\dot{x}} = \underbrace{J_x(f(x, u))\Big|_{\bar{x}, \bar{u}}}_A \hat{x} + \underbrace{J_u(f(x, u))\Big|_{\bar{x}, \bar{u}}}_B \hat{u}, \quad (3-6)$$

where J_x and J_u represent the Jacobian with respect to the state vector $x(t)$ and input vector $u(t)$ respectively. The $\hat{(\cdot)}$ -notation indicates a value deviation from the operating point and $\bar{(\cdot)}$ indicates the value at the operating point. Using the Jacobian leads to a set of LTI differential equations, formulated in a state-space representation. The system A matrix relates state value deviations $\hat{x}(t)$ to the state derivatives $\hat{\dot{x}}(t)$. The input B matrix relates input value deviations $\hat{u}(t)$ to the state derivatives $\hat{\dot{x}}(t)$. The obtained LTI state-space systems have the form

$$\begin{aligned} \hat{\dot{x}}(t) &= A\hat{x}(t) + B\hat{u}(t) \\ \hat{y}(t) &= C\hat{x}(t) + D\hat{u}(t), \end{aligned} \quad (3-7)$$

where matrix C and D relate the outputs defined in Section 2-6-2 to the state and input vector respectively.

The LTI state-space systems obtained from the non-linear drivetrain model consist of 22 states. One state describes the rotor speed dynamics, 3 states describe the spear positioning dynamics of the spear valves and 16 states describe the pipe line dynamics. There are two pipe lines, each consisting of two pipe segments. Each pipe segment is represented by two states: the chamber pressure p_c of the segment and its derivative \dot{p}_c . The remaining two states represent first-order filters which are necessary for calculation of input derivatives. The numerical solvers in Simulink required some input derivatives, so input filtering was used for calculation of those time derivatives. The first-order filters, represented by states q_1 and q_2 , provide one derivative each, and both have time constants t_{qi} of 0.001 sec.

The state vector, input vector and output vector can therefore be written as

$$x = [\omega_r \quad s_1 \quad s_2 \quad s_3 \quad p_{c1} \quad \dot{p}_{c1} \dots p_{c8} \quad \dot{p}_{c8} \quad q_1 \quad q_2]^T, \quad (3-8)$$

$$u = [\omega_{pp} \quad U_r \quad \tau_{M1} \quad s_{1,ref} \quad s_{2,ref} \quad s_{3,ref}]^T, \quad (3-9)$$

$$y = [\omega_{M1} \quad p_{lpl} \quad \Delta p_p]^T, \quad (3-10)$$

A distinction should be made between control input variables $u(t)$ and disturbance input variables which are exerted onto the system by the external environment, denoted by $w(t)$. In this case, the wind speed is considered a disturbance and the remaining inputs

are considered control inputs. The new state-space representation of the LTI differential equations now becomes

$$\begin{aligned}\hat{\dot{x}}(t) &= A\hat{x}(t) + B_c\hat{u}(t) + B_d\hat{w}(t), \\ \hat{y}(t) &= C\hat{x}(t) + D_c\hat{u}(t) + D_d\hat{w}(t),\end{aligned}\quad (3-11)$$

where control input B_c matrix and disturbance input B_d matrix relate the control input $u(t)$ and the disturbance input $w(t)$ to the state derivative, respectively. Matrix D_c and D_d relate the control input $u(t)$ and the disturbance inputs $w(t)$ to the output variables in $y(t)$, respectively.

Figure 3-11 illustrates what operating points are chosen for controller design in the following sections of this chapter. Both the torque and pressure path for operation at $C_{\tau, \max}$ are presented. The black dotted lines indicate at what operational points the non-linear Simulink drivetrain model is linearized. Each line is labeled with the wind speed that the particular operation point is corresponding to.

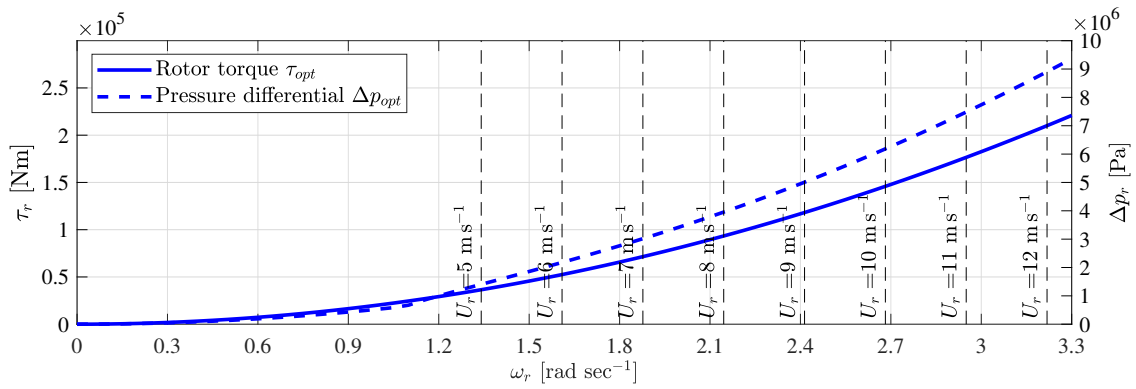


Figure 3-11: Operating points which are chosen for controller design in the following sections of this chapter. Both the torque and pressure path for operation at $C_{\tau, \max}$ are presented. The black dotted lines indicate at what operational points the non-linear Simulink drivetrain model is linearized. Each line is labeled with the wind speed that the particular operation point is corresponding to.

Transfer matrices

The relation between control inputs $U(s)$, disturbances $W(s)$ and system outputs $Y(s)$, described by Equation 3-11 is in the Laplace domain written as

$$Y(s) = C(sI - A)^{-1}(B_c U(s) + B_d W(s)) + D_c U(s) + D_d W(s) \quad (3-12)$$

where s represents the complex frequency variable in the Laplace domain. This matrix relates all control and disturbance inputs to the system outputs by LTI transfer functions. For analyzing the coupling between the in- and outputs, separate transfer matrices relating control and disturbance inputs to outputs are defined as,

$$G_{\text{plant}}(s) = \frac{Y(s)}{U(s)} = C(sI - A)^{-1}B_c + D_c, \quad (3-13)$$

$$G_{\text{dist}}(s) = \frac{Y(s)}{W(s)} = C(sI - A)^{-1}B_d + D_d. \quad (3-14)$$

3-6 Rotor stall stability analysis

In this section, an analysis on rotor stall stability is presented. Section 3-2-1 presented an analysis on the relation between power regeneration of the RPS and drivetrain efficiency. Operation at $C_{\tau, max}$ turned out to be most efficient. However, operation at $C_{\tau, max}$ decreases the margin between the point of operation and the point where rotor stall occurs, potentially leading to undesired rotor stall. This section describes this phenomenon and presents an analysis that leads towards a stability criterion for stable rotor operation and avoidance of undesired rotor stall.

What happens if an aircraft tilts backwards in an attempt to climb higher into the sky? The lift of the wing indeed increases, as the wing is tilted backwards. However, if the wing is tilted too much, the air cannot stick to the wing anymore which causes the lift to decrease. This phenomenon also occurs at wind turbine rotor blades, which is called rotor stall.

Figure 3-12 illustrates a schematic cross section of a rotor blade. The meteorological wind speed at location of the rotor is denoted by U_r , and the wind speed caused by rotation of the rotor blade is denoted by $\omega_r R$. The combination of both result in the relative wind speed U_b experienced by the rotor blade. The angle of incidence θ_b is the angle between the rotational plane and the chord line of the rotor blade. The angle of attack α_b is the angle between the relative wind and the chord line of the rotor blade. It shows that the angle of attack increases for higher wind speeds or for decreasing angles of incidence. When the angle of attack becomes too big, the air flow on the upper surface could stop sticking to the surface of the wing. Instead, the air whirls around in an irregular vortex (a condition which is mostly referred to as turbulence). This causes the lift, which is a result of the lower pressure on the upper surface of the wing, to disappear. This phenomenon is known as stall, and results in a decreasing rotor speed during increasing wind speed.

This section describes a stability criterion for the prevention of undesired rotor stall during operation.

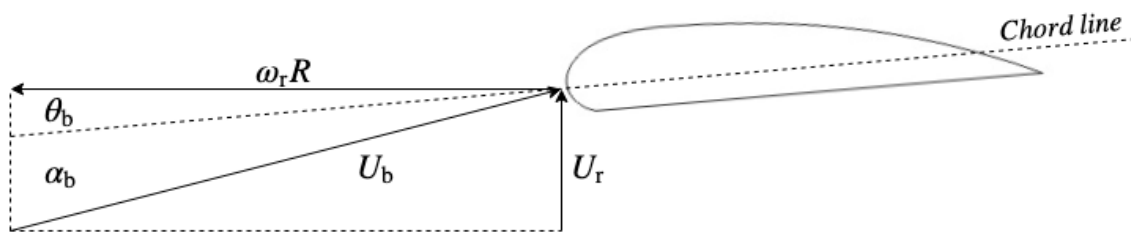


Figure 3-12: Schematic cross section of a rotor blade. The meteorological wind speed at location of the rotor is denoted by U_r , and the wind speed caused by rotation of the rotor blade is denoted by $\omega_r R$. The combination of both result in the relative wind speed U_b experienced by the rotor blade. The angle of incidence θ_b is the angle between the rotational plane and the chord line of the rotor blade. The angle of attack α_b is the angle between the relative wind and the chord line of the rotor blade.

Substitution of Equations 2-9 and 3-2 in Equation 2-10 from Section 2-2 leads to the following rotor equation

$$J_r \dot{\omega}_r = \tau_r - \tau_{sys} = c_r U_r^2 C_\tau(\lambda, \beta) - K_{opt} \omega_r^2, \quad (3-15)$$

where $c_r = \frac{1}{2}\rho\pi R^3$. Linearizing τ_r and τ_{sys} with respect to ω_r and U_r leads to

$$\hat{\tau}_r = \bar{k}_{U_r}(\omega_r, \beta, U_r)\hat{U}_r + \bar{k}_{\omega_r}(\omega_r, \beta, U_r)\hat{\omega}_r, \quad (3-16)$$

$$\hat{\tau}_{\text{sys}} = \bar{k}_{\tau_{\text{sys}}}(\omega_r, \beta, U_r)\hat{\omega}_r, \quad (3-17)$$

respectively, where $(\hat{\cdot})$ indicates a value deviation from the operating point and $(\bar{\cdot})$ is the value at the operating point [42]. Furthermore,

$$\bar{k}_{U_r}(\omega_r, \beta, U_r) = 2c_r U_r C_\tau(\lambda, \beta) - c_r \omega_r R \left. \frac{\partial C_\tau(\lambda, \beta)}{\partial \lambda} \right|_{\omega_r=\bar{\omega}_r, \beta=\bar{\beta}, U_r=\bar{U}_r}, \quad (3-18)$$

$$\bar{k}_{\omega_r}(\omega_r, \beta, U_r) = c_r U_r R \left. \frac{\partial C_\tau(\lambda, \beta)}{\partial \lambda} \right|_{\omega_r=\bar{\omega}_r, \beta=\bar{\beta}, U_r=\bar{U}_r}, \quad (3-19)$$

$$\bar{k}_{\tau_{\text{sys}}}(\omega_r) = 2K_{\text{opt}}\omega_r \Big|_{\omega_r=\bar{\omega}_r}, \quad (3-20)$$

where \bar{k}_{U_r} , \bar{k}_{ω_r} and $\bar{k}_{\tau_{\text{sys}}}$ represent the linear wind speed gain, the intrinsic speed feedback gain and the linear mode gain respectively. The linearization of Equation 3-15 can now be written as the linear state equation

$$J_r \hat{\omega}_r = \left(\bar{k}_{\omega_r}(\omega_r, \beta, U_r) - \bar{k}_{\tau_{\text{sys}}}(\omega_r, \beta, U_r) \right) \hat{\omega}_r + \bar{k}_{U_r}(\omega_r, \beta, U_r) \hat{U}_r. \quad (3-21)$$

For stable rotor operation, the real part of the eigenvalues have to be negative. From this one-dimensional equation therefore, it could be observed that stable turbine behavior will be attained if the following equality holds

$$\bar{k}_{\omega_r}(\omega_r, \beta, U_r) - \bar{k}_{\tau_{\text{sys}}}(\omega_r, \beta, U_r) < 0. \quad (3-22)$$

This Equation shows that the intrinsic feedback gain \bar{k}_{ω_r} plays a critical role for attaining stable turbine behavior since $\{k_{\tau_{\text{sys}}} \in \mathbb{R} \mid k_{\tau_{\text{sys}}} \geq 0\}$. During operation with high tip-speed ratio's, the intrinsic feedback gain is negative $\bar{k}_{\omega_r} < 0$ since $\partial C_\tau / \partial \lambda < 0$, resulting in negative damping values and higher stability margins [42]. However, for lower tip-speed ratio's $\lambda < \lambda_{C_\tau, \text{max}}$, the intrinsic feedback gain becomes positive $\bar{k}_{\omega_r} > 0$ since $\partial C_\tau / \partial \lambda > 0$ (Figure 2-8) which can result in an exceedance of this inequality, resulting in 'positive damping', thus instability. To attain stable turbine behavior, the following stability criterion is derived, where the derivative of the torque coefficient C_τ has to be smaller than the quantity Γ_s

$$\frac{\partial C_\tau(\lambda, \beta)}{\partial \lambda} < \underbrace{2 \frac{C_\tau(\lambda, \beta)}{\lambda}}_{\Gamma_s}. \quad (3-23)$$

Since no drivetrain dynamics are considered at all in this analysis, evidently, exactly the same stability criterion can be derived by maintaining the wind speed gain positive such that stall won't occur.

$$\bar{k}_{U_r}(\omega_r, \beta, U_r) > 0. \quad (3-24)$$

Figure 3-13 illustrates the torque coefficient C_τ at fine pitch angle β_0 , its derivative and quantity Γ_s as a function of the tip-speed ratio λ . The vertical black line indicates the tip-speed ratio where $\partial C_\tau / \partial \lambda < \Gamma_s$. Stable turbine behavior will be attained above this tip-speed ratio of $\lambda_{\min} = 4.55$. The closer the designed operational point is to λ_{\min} , the smaller the stability margin.

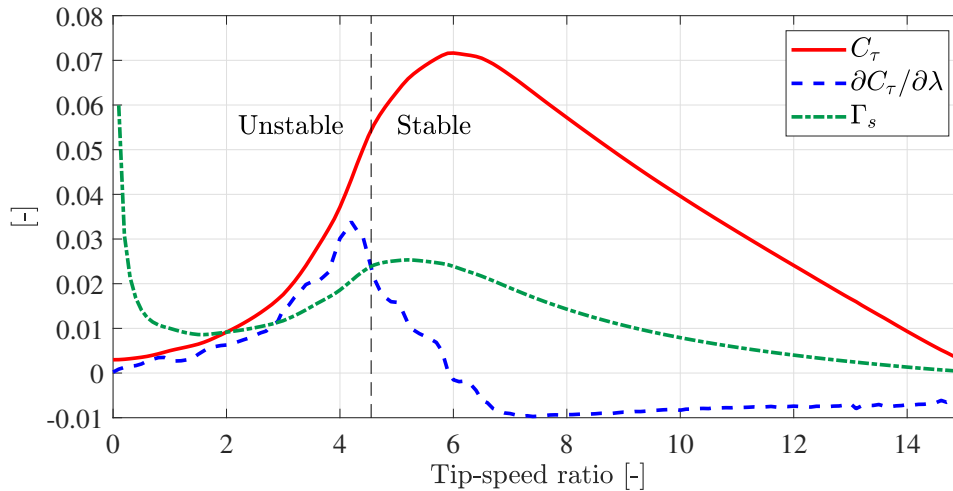


Figure 3-13: Torque coefficient C_τ at fine pitch angle β_0 , its derivative and quantity Γ_s as a function of the tip-speed ratio λ . The vertical black line indicates the tip-speed ratio where $\partial C_\tau / \partial \lambda = \Gamma_s$. Stable turbine behavior is attained above this tip-speed ratio of $\lambda_{\min} = 4.55$.

3-6-1 The effect of incorporating drivetrain dynamics

This stability criterion is derived for a rigid coupling between the rotor, and the system torque actuator. However, as derived in Section 2-4, capacitance (stiffness) and resistance (damping) of the drive-train was introduced. In Bianchi et al. [42], a Linear Parameter-Varying (LPV) state-space model of a conventional drivetrain was derived, incorporating the damping and stiffness of the drivetrain components. This was done by modeling the drivetrain as two rotating inertia's, coupled by a shaft with stiffness C_s and and damping coefficient R_s , as illustrated in Figure 3-14.

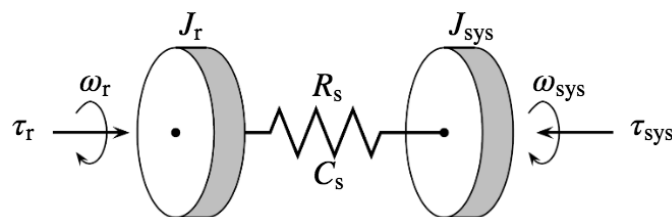


Figure 3-14: Simplified drivetrain model of conventional wind turbine, modeled as two rotating inertias which are dynamically coupled by means of a spring and damper. The rotor is represented by the left-handed inertia J_r with rotational speed ω_r , and is excited with torque τ_r . The drivetrain components are represented by the right-handed inertia J_{sys} with rotational speed ω_{sys} and is excited with torque τ_{sys} . Capacitance and resistance of the combined drivetrain are modeled as a spring and damper, respectively. The spring and damper have spring and damper coefficients K_s and C_s , respectively [42].

Therefore, this could also be derived for a hydraulic drive-train with inductance, capacitance and resistance, as described in Section 2-4. A simplified drivetrain model is taken for analysis, where the rotor pump is coupled to one single pipe segment with one spear valve at the end. Recall Equations 2-30, 2-31 and 2-32 and the net flow v of one pipe segment which is described as

$$v = v_{\text{in}} - v_{\text{out}}, \quad \dot{v} = Q_{\text{in}} - Q_{\text{out}}. \quad (3-25)$$

Together with Equation 2-51 for the actuator dynamics of a spear valve, a non-linear state-space equation is derived. As presented by Equation 2-42, the resistance terms $R_{(e),1}$ and $R_{(e),2}$ contain the (state) flow variables $Q_{(e),1}$ and $Q_{(e),2}$, respectively. The state equation looks like

$$\begin{bmatrix} \dot{v} \\ \dot{Q}_{(e),1} \\ \dot{Q}_{(e),2} \\ \dot{s}_1 \end{bmatrix} = \begin{bmatrix} 0 & 1 & -1 & 0 \\ -\frac{1}{C_{(e)}I_{(e),R}} & -\frac{R_{(e),1}}{I_{(e),R}} & 0 & 0 \\ \frac{1}{C_{(e)}I_{(e)}} & 0 & -\frac{R_{(e),2}}{I_{(e)}} & 0 \\ 0 & 0 & 0 & -\frac{1}{t_{s1}} \end{bmatrix} \begin{bmatrix} v \\ Q_{(e),1} \\ Q_{(e),2} \\ s_1 \end{bmatrix} + \begin{bmatrix} 0 \\ \frac{1}{I_{(e),R}} \Delta p_r \\ -\frac{1}{I_{(e)}} \Delta p_{\text{nz}} \\ \frac{1}{t_{s1}} s_{1,\text{ref}} \end{bmatrix} \quad (3-26)$$

where Δp_{nz} is the pressure differential across the spear valve at the end of the pipe line. The inertial terms $I_{(e),R}$ in entries a_{21} and a_{22} are the fluid inertial term as presented before in Section 2-4. However, since this is the inertial term for the flow that is entering the pipe element, it is expanded with the rotor inertia J_r as described in Mulders et al. [28]. This looks like

$$I_{(e),R} = \frac{J_r \eta_{m,r}}{V_r^2 \eta_{v,r}} + I_{(e)}. \quad (3-27)$$

Equation 3-16 for the linearized rotor torque is rewritten to a pressure differential across the rotor pump as

$$\Delta \bar{p}_r(\bar{\omega}_r, \bar{U}_r) = \bar{k}_{U_r}^* (\bar{\omega}_r, \bar{U}) \hat{U}_r + \bar{k}_{Q_{(e),1}}^* (\bar{\omega}_r, \bar{U}_r) \hat{Q}_{(e),1}, \quad (3-28)$$

where the new linear intrinsic flow feedback gain and the wind speed pressure gain are defined by the conversions

$$\bar{k}_{Q_{(e),1}}^* = \bar{k}_{\omega_r} \frac{\eta_{m,r}}{V_r^2 \eta_{v,r}}, \quad \bar{k}_{U_r}^* = \bar{k}_{U_r} \frac{\eta_{m,r}}{V_r}, \quad (3-29)$$

respectively, with rotor pump volumetric displacement V_r .

The pressure differential across the spear valve is dependent of the spear position and the flow $Q_{(e),2}$ flowing through it. Equation 2-47 gives the relation between the spear position and the resulting effective nozzle area of the spear valve. Substituting this relation in Equation 2-50 results in the pressure differential across the spear valve. Linearization of this Equation with respect to spear position s_1 and flow $Q_{(e),2}$ result in

$$\Delta \bar{p}_{\text{nz}}(\bar{Q}_{(e),2}, \bar{s}_{s1}) = \bar{k}_{Q_{(e),2}} (\bar{Q}_{(e),2}, \bar{s}_{s1}) \hat{Q}_{(e),2} + \bar{k}_{s1} (\bar{Q}_{(e),2}, \bar{s}_{s1}) \hat{s}_1 \quad (3-30)$$

where

$$\bar{k}_{Q_{(e),2}} (\bar{Q}_{(e),2}, \bar{s}_{s1}) = \frac{Q_{(e),2} \rho_w}{C_d^2 \pi^2 \left(D_{\text{ns}}^2 / 4 - (s_{\text{max}} - s_1)^2 \tan^2(\alpha/2) \right)^2} \Bigg|_{\bar{Q}_{(e),2}, \bar{s}_{s1}}, \quad (3-31)$$

$$\bar{k}_{s1} (\bar{Q}_{(e),2}, \bar{s}_{s1}) = \frac{2Q_{(e),2}^2 \rho_w (s_1 - s_{\text{max}}) \tan^2(\alpha/2)}{C_d^2 \pi^2 \left(D_{\text{ns}}^2 / 4 - (s_{\text{max}} - s_1)^2 \tan^2(\alpha/2) \right)^3} \Bigg|_{\bar{Q}_{(e),2}, \bar{s}_{s1}}. \quad (3-32)$$

The state equation of Equation 3-26 can now be written as

$$\hat{\dot{x}} = A\hat{x} + B\hat{u} + B_{U_r}\hat{w}, \quad (3-33)$$

where

$$A = \begin{bmatrix} 0 & 1 & -1 & 0 \\ -\frac{1}{C_{(e)}I_{(e),R}} & -\frac{(R_{(e),1}-\bar{k}_{Q_{(e),1}}^*)}{I_{(e),R}} & 0 & 0 \\ \frac{1}{C_{(e)}I_{(e)}} & 0 & -\frac{(R_{(e),2}+\bar{k}_{Q_{(e),2}}^*)}{I_{(e)}} & -\frac{\bar{k}_{s1}}{I_{(e)}} \\ 0 & 0 & 0 & -\frac{1}{t_{s1}} \end{bmatrix}, \quad (3-34)$$

$$B = \begin{bmatrix} 0 & 0 & 0 & \frac{1}{t_{s1}} \end{bmatrix}^T, \quad B_{U_r} = \begin{bmatrix} 0 & \frac{k_{U_r}^*}{I_{(e),R}} & 0 & 0 \end{bmatrix}^T$$

with the respective state vector and input and wind disturbance variables

$$x = \left[\hat{v} \quad \hat{Q}_{in} \quad \hat{Q}_{out} \quad \hat{s}_1 \right]^T, \quad u = s_{1,ref}, \quad w = U_r, \quad (3-35)$$

It is clearly seen that the intrinsic flow feedback gain $k_{Q_{(e),1}}^*$ appears in the same entry of matrix A as the negative resistance (damping) term $R_{(e),1}$. Increased damping $R_{(e),1}$ improves compensation for an increasing intrinsic flow feedback gain $k_{Q_{(e),1}}^*$ (as $\partial C_\tau / \partial \lambda$ increases for decreasing $\lambda < \lambda_{C_\tau, max}$). This suggests **increased stability margins** due to dynamic drive-train effects. Schmitz et al. [59] also describes that the effects of damping in a drivetrain with hydrostatic transmission improves turbine stability. This was confirmed with tests that showed excellent damping characteristics of hydraulic components, compensating instability. However, the stability criterion described by Equation 3-23 describes the worst case scenario since it completely neglects drivetrain dynamics. Therefore, this criterion is used for controller design.

3-7 Relative Gain Array analysis

This sections presents an analysis of the coupling between in- and output of the drivetrain model, which is very useful for making a substantiated assessment on what control implementation will be used. The analysis is performed with linearized LTI models obtained according to the procedure described in Section 3-5.

For Single-Input Single-Output (SISO) systems, coupling between the in- and output in question is evident. This basically means that the control input directly relates to the measured output. However, the DOT drivetrain is a Multiple-Input Multiple-Output (MIMO) system. In this case, pairing of control inputs to measured outputs is not self-evident anymore. Therefore, a Relative Gain Array (RGA) analysis is performed; a classical widely-used method for determining the best input-output pairings for multivariable control systems. Besides that, the RGA analysis quantifies the level of input-output interaction which leads to the assessment of whether a decentralized or centralized control implementation should be used.

Given an LTI system represented by transfer matrix G , the RGA \mathcal{R} is defined as

$$\mathcal{R}(G(s)) = G(s) \circ (G(s)^{-1})^T \quad (3-36)$$

where \circ represents the Hadamard (or entrywise) product of two matrices. The RGA is often generalized to be used when G is singular, e.g. non-square, by replacing the inverse of G with its Moore-Penrose inverse, or pseudo-inverse G^\dagger [53].

The RGA is analyzed for all potential control inputs. The transfer matrix between the control inputs and measured outputs is defined Equation 3-13. However, assuming that the torque demand τ_{M1} for power regeneration of the RPS should follow a varying setpoint based on the rotational speed of the pre-pressure pumps, the generator torque demand τ_{M1} is left out for the RGA analysis. Therefore, the RGA analysis is first performed for the system with the rotational speed ω_{pp} of the pre-pressure pumps and the spear position reference values $s_{i,\text{ref}}$ as control inputs. The outputs are the rotational speed ω_{M1} of the internal water motor, the intake pressure p_{fl} of the rotor pump and the pressure differential Δp_r across the rotor pump. This is written as

$$\begin{bmatrix} \omega_{M1} \\ p_{\text{fl}} \\ \Delta p_r \end{bmatrix} = \begin{bmatrix} g_{11} & g_{12} & g_{13} & g_{14} \\ g_{21} & g_{22} & g_{23} & g_{24} \\ g_{31} & g_{32} & g_{33} & g_{34} \end{bmatrix} \begin{bmatrix} \omega_{pp} \\ s_{1,\text{ref}} \\ s_{2,\text{ref}} \\ s_{3,\text{ref}} \end{bmatrix}, \quad (3-37)$$

where g_{ii} is each separate transfer function between the individual control inputs and measured outputs. With this relation it is easily shown that all measured outputs are influenced by every control input. To what extent the in- and outputs interacts with each other however, varies for different frequency regions.

The RGA is determined for every operation point in the below-rated operational region, as a function of frequency. Figure 3-15 illustrates the RGA by means of three separate diagrams. From the left to the right, input-output coupling is illustrated with respect to the rotational speed of internal water motor M_1 , the feed line pressure p_{fl} and the pressure differential Δp_r across the rotor pump. All possible degrees of input-output coupling for all operating points in the below-rated operational region are covered by the colored areas. The fat lines indicate the averaged input-output coupling of all operating points.

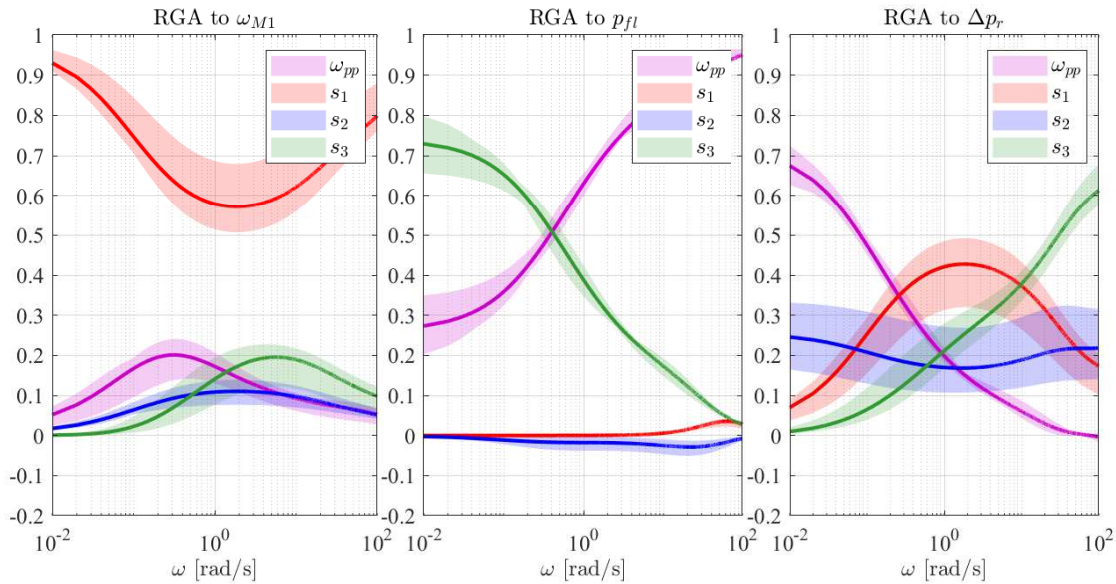


Figure 3-15: RGA curves, quantifying the level of in/output interaction of the MIMO system where the rotational speed ω_{pp} of the pre-pressure pumps and the spear position reference values $s_{i,ref}$ of the three spear valves are considered as control inputs. From the left to the right, input-output coupling is illustrated with respect to the rotational speed ω_{M1} of internal water motor, the feed line pressure p_{fl} and the pressure differential Δp_r across the rotor pump. All possible degrees of input-output coupling for all operating points in the below-rated operational region are covered by the colored areas. The fat lines indicate the averaged input-output coupling of all operating points. It can be easily concluded that the system is quite coupled for all frequencies. Especially the pressure differential Δp_r across the rotor pump encounters a high degree of coupling to multiple control inputs.

A value close to 1 means that the input-output pair in question encounters a high degree of coupling with respect to other inputs. On the other hand, values close to 0 indicate a lower degree of coupling. From Figure 3-15, it is concluded that the system is quite cross-coupled in all frequency regions. Especially the pressure differential Δp_r across the rotor pump encounters a high degree of coupling to multiple control inputs. This could suggest a MIMO control strategy.

However, it could be interesting to look at the case where the rotational speed of the pre-pressure pumps is eliminated as a control variable as well by giving it a feed forward speed set-point. This possibly results in an easier control implementation, but first and foremost, the DOT hydraulic drive train only has limited supply of seawater, delivered by the pre-pressure pumps. For maximizing the outflow of seawater, leading to the Pelton turbine, it is desirable to operate the pre-pressure pumps at their maximum possible rotational speed throughout the total below-rated operational region, dependent of how much electrical power can be regenerated by the RPS. Operating the pre-pressure pumps at their maximum attainable rotational speed, results in the highest drivetrain efficiency, as was explained in detail in Section 3-2-1. This results in a very strict operational path for the pre-pressure pumps, which could be achieved by feed forward control of the pre-pressure pumps. In this case, the three spear valves could be used for feedback disturbance rejection.

Leaving the rotational speed of the pre-pressure pumps out of the loop, the transfer matrix looks quite similar as defined in Equation 3-37, however, without ω_{pp} in the input vector.

Figure 3-16 again illustrates the RGA curves, quantifying the level of in/output interaction of the MIMO system.

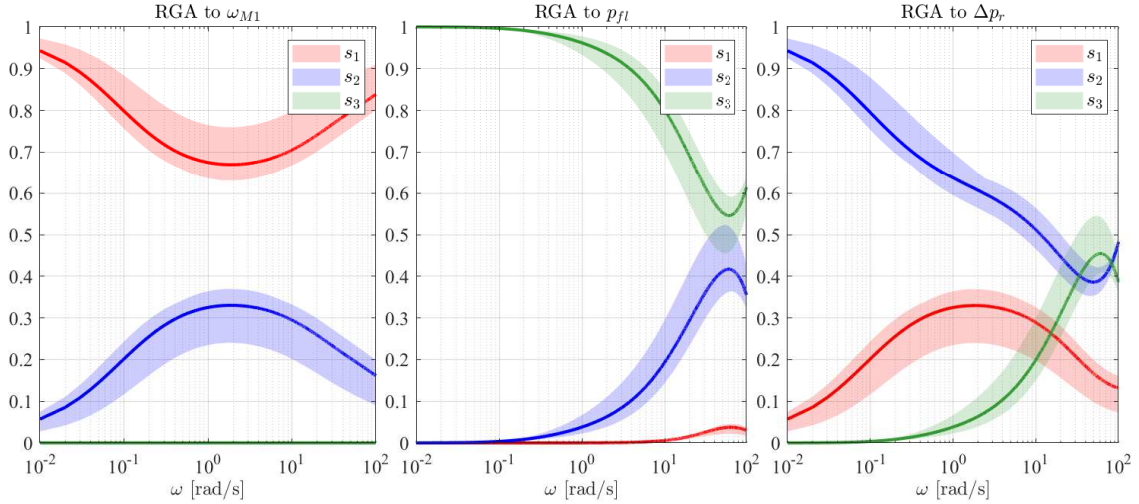


Figure 3-16: RGA curves, quantifying the level of in/output interaction of the MIMO system where only the spear position reference values $s_{i,\text{ref}}$ of the three spear valves are considered as control inputs. From the left to the right, input-output coupling is illustrated with respect to the rotational speed of internal water motor M_1 , the feed line pressure p_{fl} and the pressure differential Δp_r across the rotor pump. All possible degrees of input-output coupling for all operating points in the below-rated operational region are covered by the colored areas. The fat lines indicate the averaged input-output coupling of all operating points. It can be concluded that the system is significantly less coupled by leaving the rotational speed of the pre-pressure pumps out of the loop. Especially for lower frequencies, the system looks quite decoupled.

From Figure 3-16, it is concluded that the relations between the spear position and the measured outputs are much more decoupled with respect to each other in the lower frequency regions. For low frequencies of $\omega < 10^{-2} \text{ rad s}^{-1}$, the system is almost fully decoupled. The rotational speed of the internal water motor ω_{M1} is mostly coupled to spear position s_1 , the feed line pressure p_{fl} is mostly coupled to spear position s_3 and the pressure differential Δp_r is mostly coupled to spear position s_2 .

This creates the potential for a decoupled (or decentralized) SISO control strategy with control with the three most optimal input-output pairs, mentioned above. This will be described in more detail in the next section.

3-8 SISO Control Design using Interpolated Gain Scheduling

This section elaborates on controller design by means of loop shaping the transfer functions of the input-output pairs encountering the highest degree of coupling. A procedure for H_∞ fixed-structure controller synthesis is applied to achieve the desired target loop shapes.

Based on the RGA analysis performed in the previous section, individual SISO controllers are constructed for the proposed input/output pairs $G_i(s)$. The presence of non-linearities is covered for by means of gain scheduled controllers, resulting in equal controller performance throughout the whole range of operation.

For each operating point, two Proportional Integral (PI)-controllers and one Proportional Integral Derivative (PID)-controller $K_i(s)$ are tuned by loop shaping. This choice of controller structure is further explained later in this section. Since controllers should be tuned for multiple operating points, this process is automated by a procedure for H_∞ fixed-structure controller synthesis [96], subject to H_∞ constraints. Loop shaping is a frequency-domain technique for enforcing requirements on control bandwidth (thus response speed), roll-off and steady-state error. The idea of this H_∞ procedure is to specify a target loop shape for the open-loop response $L_i(s) = G_i(s)K_i(s)$.

Ideally, an integrator is chosen as loop-shape since it is crossing the 0 dB line with a roll-off of -20 dB/dec. However, to avoid difficulties with marginally stable poles and improper inverses, the target loop shape is chosen to be a bi-proper, bi-stable realization. The target loop shape is defined as

$$w_i(s) = \frac{s/M_i + \omega_{c,i}}{s + \omega_{c,i}A_i} \quad (3-38)$$

where $|w_i(j\omega)|$ is equal to $1/M_i$ at high frequencies and $1/A_i$ at low frequencies. To simulate an integrator loop-shape, $M_i = 10^3$ and $A_i = 10^{-3}$ (used for all three controllers). The target loop-shape has to be turned into constraints on the closed-loop gains. Therefore, the target loop shape w_i and its reciprocal are used to filter the error signal e and the assumed white noise source n_w , respectively. Figure 3-17 the control diagram with the parameterized controller K .

This system can be transformed to a generalized plant, which is the complete system,

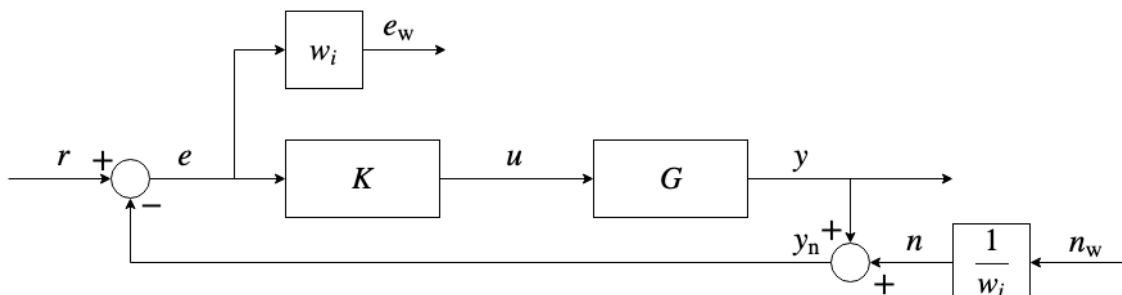


Figure 3-17: Control diagram of plant G with parameterized structured controller K . The error signal e and the white noise source n_w are filtered with the target loop shape, described by w_i .

excluding the controller K . The generalized plant is formulated as

$$\begin{bmatrix} z \\ e \end{bmatrix} = \begin{bmatrix} P_{11} & P_{12} \\ P_{21} & P_{22} \end{bmatrix} \begin{bmatrix} w \\ u \end{bmatrix} \quad (3-39)$$

with $w = [r \ n_w]^T$ and $z = [y \ e_w]^T$. Including the controller K in the system result in the nominal plant $z = Nw$ by. This is illustrated in Figure 3-18.

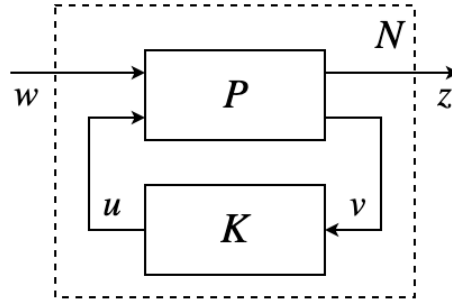


Figure 3-18: Nominal plant $z = Nw$ representation of the closed loop system.

The nominal plant N is determined by applying the lower linear fractional transformation (LFT) of P as

$$N = P_{11} + P_{12}K(I - P_{22}K)^{-1}P_{21}, \quad (3-40)$$

which results in a nominal plant

$$N = \begin{bmatrix} T & -w_i^{-1}T \\ w_i S & -S \end{bmatrix}, \quad (3-41)$$

with the sensitivity function $S = (I + GK)^{-1}$ and the complementary sensitivity function $T = GK(I + GK)^{-1}$.

The procedure for H_∞ fixed-structure controller synthesis minimizes $\|N(K)\|_\infty$ for K and tries to enforce $\|N(K)\|_\infty < 1 \forall \omega$, such that the closed-loop system has adequate stability margins and small overshoot. According to this procedure, two PI-controllers and one PID-controller are tuned such that the desired control bandwidth is achieved. This choice is further explained later in this section. In the Laplace domain, a PID-controller is defined as

$$K(s) = K_p + K_i \frac{1}{s} + K_d \frac{s}{T_f s + 1} \quad (3-42)$$

where K_p , K_i and K_d represent the proportional, integrator and derivative terms, respectively. Filter coefficient T_f is introduced to filter the derivative term such that high frequency noise is less amplified. Minimizing the infinity norm of the nominal plant now looks like

$$\arg \min_{K_p, K_i, K_d, T_f} \|N(K_p, K_i, K_d, T_f)\|_\infty \forall \omega. \quad (3-43)$$

To illustrate this procedure for controller synthesis, one operation point is chosen for illustrative purposes. This operation point is specified first.

3-8-1 Operation point specification

For presentation of the controller design procedure, the following linearization point is used as an example. Table 3-1 presents the parameter values for this operation point with steady-state conditions:

Specification	Operation point
\bar{U}_r	11 m s ⁻¹
$\bar{\omega}_r$	2.950 rad s ⁻¹ (28.17 rev min ⁻¹)
$\bar{\lambda}$	5.900
$\bar{\omega}_{pp}$	3283 rev min ⁻¹
\bar{s}_1	3.697 mm
\bar{s}_2	9.497 mm
\bar{s}_3	2.745 mm
$\bar{\tau}_{M1}$	228.0 Nm
$\Delta\bar{p}_r$	74.82 bar
\bar{p}_{fl}	5.000 bar
$\bar{\omega}_{M1}$	1555 rev min ⁻¹

Table 3-1: Operation point specifications of the LTI model which is used for presentation of the controller design procedure.

3-8-2 Controller synthesis

As mentioned earlier, a procedure for H_∞ fixed-structure controller synthesis is used for obtaining a set of three decentralized SISO controllers. Based on the RGA analysis presented in Section 3-7, the following input-output pairs are considered for controller synthesis

Plant	Input	Output
G_1	$s_{1,ref}$	ω_{M1}
G_2	$s_{2,ref}$	Δp_r
G_3	$s_{3,ref}$	p_{fl}

Table 3-2: Input-output pairs used for synthesis of three decentralized SISO controllers. Plant G_1 describes the dynamics between spear position reference $s_{1,ref}$ and the rotational speed ω_{M1} of the internal water motor. Plant G_2 describes the dynamics between spear position reference $s_{2,ref}$ and the pressure differential Δp_r across the rotor pump. Plant G_3 describes the dynamics between spear position reference $s_{3,ref}$ and the feed-line pressure.

where plant name G_i will be used to refer to one of these input-output relations. Plant G_1 describes the dynamics between spear position reference $s_{1,ref}$ and the rotational speed ω_{M1} of the internal water motor. Plant G_2 describes the dynamics between spear position reference $s_{2,ref}$ and the pressure differential Δp_r across the rotor pump. Plant G_3 describes the dynamics between spear position reference $s_{3,ref}$ and the feed-line pressure.

As an example, the blue dashed line in Figure 3-19 illustrates the open-loop Bode magnitude and phase plot of G_1 . The target loop-shape of the form presented by Equation 3-38 has a cross-over frequency $\omega_{c,1}$ of 6 rad s⁻¹ and is illustrated by the green dotted line. The cross-over frequency represents the controller performance (a higher cross-over frequency

results in faster time-domain response). The H_∞ procedure returns a PI-controller K_1 such that the open-loop system G_1K_1 obtains an open-loop gain with cross-over frequency $\omega_{c,1}$.

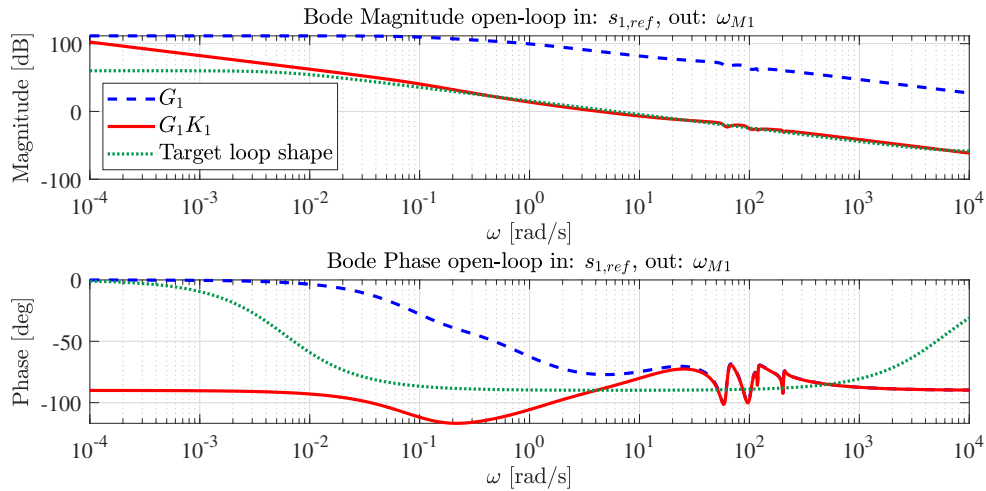


Figure 3-19: Bode magnitude and phase plot of transfer function G_1 , loop-gain $L_1 = G_1K_1$ and the target loop-shape. The transfer function has spear position reference $s_{1,ref}$ as input and the rotational speed ω_{M1} of the internal water motor as output.

It can be concluded that the loop-gain has a satisfactory loop-shape as it has the desired cross-over frequency and negative roll-off in the cross-over region. For **robustness** of the controlled plant, a minimal **phase margin** of $\phi_{pm} > 50^\circ$ and a **gain margin** of $g_m > 5$ ($g_m > 14$ dB) is desired. With a phase margin of $\phi_{G_1K_1} = 90.8^\circ$ and an infinite gain margin, both these robustness criteria are met.

The same procedure is used for the transfer function G_2 , to obtain a PI-controller K_2 . Again, the target cross-over frequency is 6 rad s^{-1} . Figure 3-20 illustrates the open-loop Bode magnitude and phase plot of G_2 , G_2K_2 and the target loop shape. For clear visibility, the phase plot is wrapped between -180 deg and 180 deg. With a phase margin of $\phi_{G_2K_2} = 52.9^\circ$ and a gain margin of $g_{G_2K_2} = 15.0$ dB, both robustness criteria are met.

For synthesis of controller K_3 , only a proportional and integral term is not sufficient for attaining both performance and robustness together. As Figure 3-21 illustrates, the phase of G_3 starts to approach -180° , and crosses this stability limit at about 8 rad s^{-1} . Again, for clear visibility, the phase plot is wrapped between -180 deg and 180 deg. For attaining a robust phase margin of $\phi_{G_3K_3}$, the control bandwidth would be limited at about 1 rad s^{-1} . Addition of a derivative term in this region, adds phase such that a higher control bandwidth is achieved while meeting the requirements for robustness. Therefore, the procedure for H_∞ controller synthesis is used to tune a PID-controller in this case. The phase plot of the open-loop gain G_3K_3 in Figure 3-21 clearly shows the effect of the derivative term, compared to G_3 only. The target cross-over frequency is 10 rad s^{-1} . With a phase margin of $\phi_{G_3K_3} = 70.7^\circ$ and a gain margin of $g_{G_3K_3} = 17.5$ dB, both robustness criteria are met.

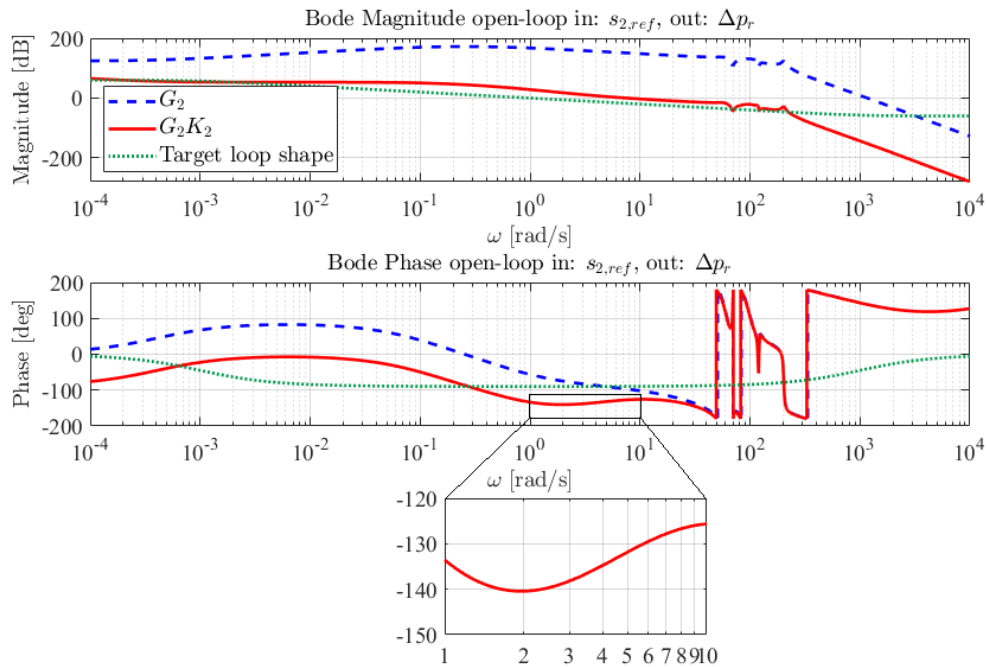


Figure 3-20: Bode magnitude and phase plot of transfer function G_2 , loop-gain $L_2 = G_2K_2$ and the target loop-shape. The transfer function has spear position reference $s_{2,ref}$ as input and the pressure differential Δp_r across the rotor pump as output. The zoomed area shows a small phase drop right before crossing the 0 dB line.

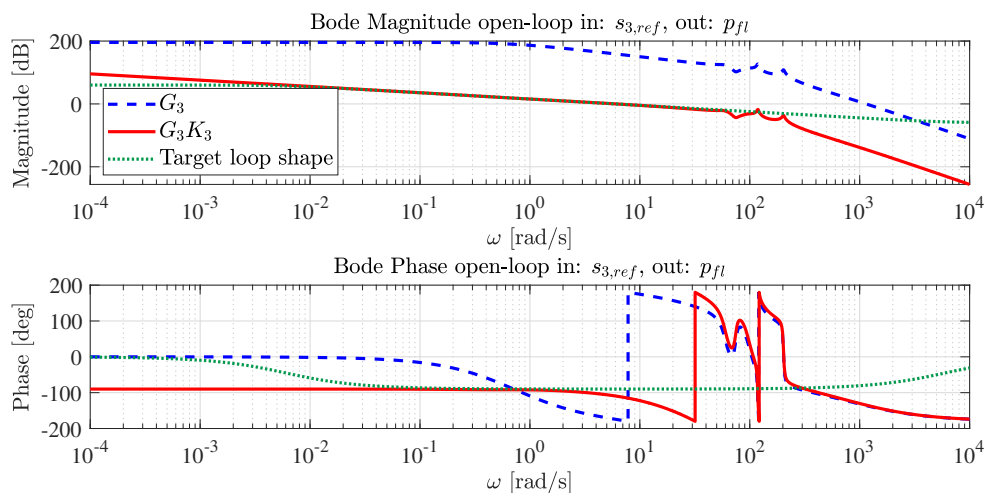


Figure 3-21: Bode magnitude and phase plot of transfer function G_3 , loop-gain $L_3 = G_3K_3$ and the target loop-shape. The transfer function has spear position reference $s_{3,ref}$ as input and the feed-line pressure p_{fl} as output.

3-8-3 Modulus margin

For robustness, sufficient phase margin and gain margin is assured for all three controllers. However, Figure 3-20 zooms in on a section of the phase plot. It shows that the phase $\phi_{G_2K_2}$ 'fulfills' the robust requirement in terms of phase margin where the magnitude plot crosses the 0 dB line (6 rad s^{-1}). However, it also clearly shows a small phase drop right before that.

To fully ensure robustness of the controller, it might be useful to have a look at the Nyquist plot. Figure 3-22a shows the Nyquist plot of $L_2(j\omega) = G_2(j\omega)K_2(j\omega)$. The distance between the point $(-1, 0)$ and the Nyquist curve is defined as $|1 + L(j\omega)|$. Therefore, the shortest distance between the Nyquist curve and the point $(-1, 0)$, the Modulus Margin, is the inverse of the sensitivity peak $M_{S,i}$, defined as

$$M_{S,i} = \max_{0 \leq \omega < \infty} |S_i(j\omega)| = \max_{0 \leq \omega < \infty} \left| \frac{1}{1 + G_i(j\omega)K_i(j\omega)} \right| = \min_{0 \leq \omega < \infty} |1 + L_i(j\omega)|. \quad (3-44)$$

It is observed that there is a significant amount of space left between the Nyquist curve and the point $(-1, 0)$, which is critical for stability. Therefore, an increase of proportional gain or phase will not directly result in instability. Figure 3-22b shows the sensitivity function $|1 + L_2(j\omega)|^{-1}$ with the peak sensitivity $M_{S,2}$ indicated by the black dashed line at 13.9 rad s^{-1} . This sensitivity peak is a result of the waterbed effect [53], and is practically unavoidable due to the relative degree ($N_{p_i} - N_{z_i}$) that is larger than 2. The amount of poles and zeros is represented by N_{p_i} and N_{z_i} , respectively. From this figure, it is clearly visible that an increase of proportional gain or phase will result in a higher peak sensitivity, thus less noise attenuation [53]. If the Nyquist curve reaches $(-1, 0)$, the peak sensitivity goes to infinity ($M_{S,i} \rightarrow \infty$), and the plant becomes unstable.

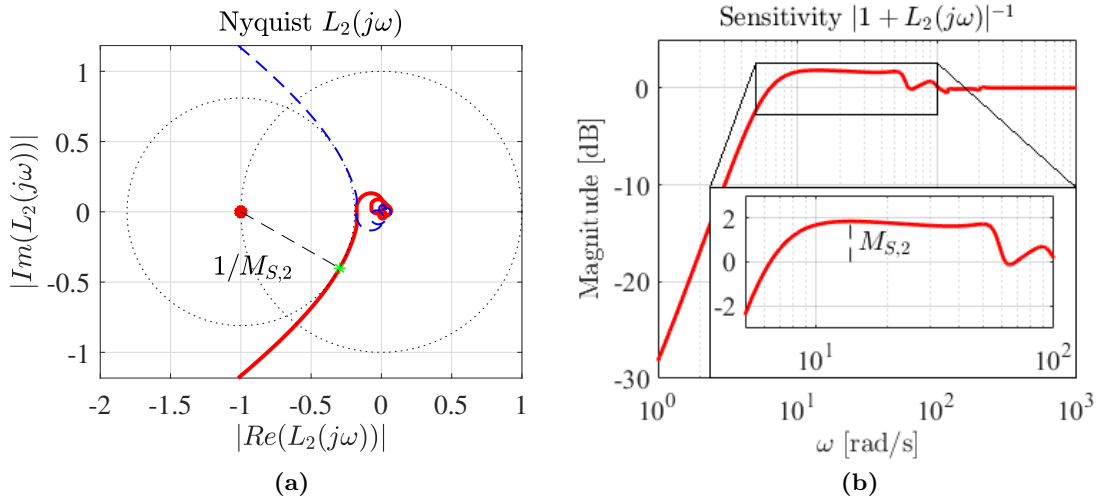


Figure 3-22: (a) The red line is the Nyquist plot of $L_2(j\omega) = G_2(j\omega)K_2(j\omega)$. The blue dashed line is the inverse polar plot of the same system. The shortest distance between $(-1, 0)$ and the Nyquist curve is equal to the inverse of the sensitivity peak, therefore indicated by $1/M_{S,2}$. This is the modulus margin of 0.81 at 13.9 rad s^{-1} . (b) Sensitivity plot of $L_2(j\omega)$. The peak sensitivity $M_{S,2}$ is found to be 1.2 (or 1.8 dB).

Figure 3-23a shows the Nyquist plot of $L_1(j\omega)$. For $L_1(j\omega)$, a modulus margin of 0.98 was found at 58.0 rad s^{-1} . By approximation therefore, $L_1(j\omega)$ does not come inside the unit circle with center point $(-1, 0)$. This translates to a peak sensitivity $M_{S,1}$ of 0.13 dB,

so no waterbed effect is encountered for this open-loop transfer function, as illustrated in Figure 3-23b. The reason for this is a relative degree of 1 [53].

Figure 3-24a shows the Nyquist plot of $L_3(j\omega)$, where a modulus margin of 0.79 was found at 15.8 rad s^{-1} . This directly translates to a peak sensitivity $M_{S,3}$ of 2 dB, which is illustrated in Figure 3-24b. Occurrence of the waterbed effect is unavoidable due to a relative degree larger than 2. All three Nyquist curves show that an increase of proportional gain or phase will not directly lead to instability of the system.

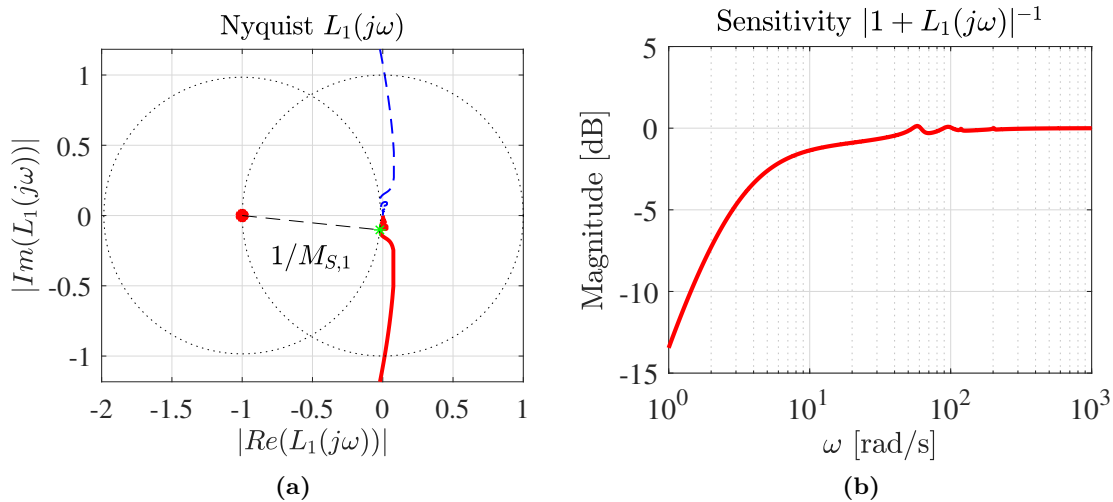


Figure 3-23: (a) Nyquist plot of $L_1(j\omega)$ in red. The blue dashed line is the inverse polar plot of the same system. A modulus margin of 0.98 (thus peak sensitivity $M_{S,1}$ of 0.13 dB) was found at 58.0 rad s^{-1} . Figure (b) shows the Sensitivity function of $L_1j\omega$. No waterbed effect is observed.

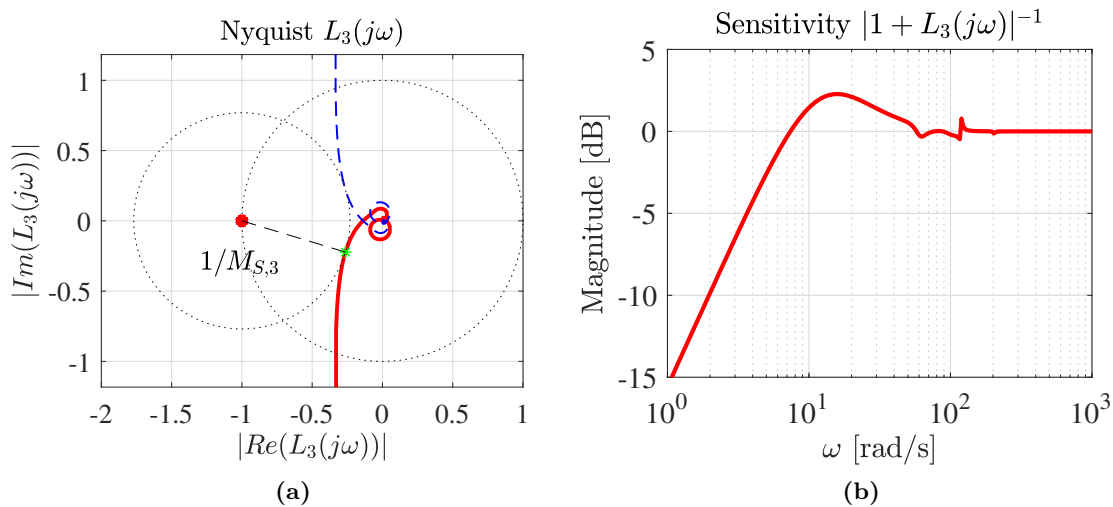


Figure 3-24: (a) Nyquist plot of $L_3(j\omega)$ in red. The blue dashed line is the inverse polar plot of the same system. A modulus margin of 0.79 (thus peak sensitivity $M_{S,3}$ of 2 dB) was found at 15.8 rad s^{-1} . Figure b shows the Sensitivity function of $L_3j\omega$.

The procedure for controller synthesis as presented in this section is performed for all operation points that are described in section 3-5. For all controllers, robustness is ensured in terms of phase, gain margin and modulus margin. The Figures 3-25a, 3-25b and 3-25c illustrate the Bode magnitude and phase plots for all chosen operation points of G_i and G_iK_i .

3-8-4 Gain scheduling with linear interpolation

All controllers obtained by the H_∞ structured controller synthesis, described in the previous subsection, are used for control of the DOT wind turbine close to the operation points that the controllers are designed for. The reason for this is that equal control performance is desired throughout the complete below-rate operational domain.

The PI- and PID-controllers are structured controllers, which allows for a scheduling of the controller parameters. For unstructured controllers, gain scheduling can be realized by means of output interpolation, as proposed in [34]. The controllers are stacked by means of a Linear Parameter Varying (LPV) type of structure, and look like

$$\dot{x}(\varphi, t) = A(\varphi)x(t) + B(\varphi)e(t), \quad (3-45)$$

$$\hat{s}_{i,\text{ref}}(\varphi, t) = C(\varphi)x(t) + D(\varphi)e(t), \quad (3-46)$$

where φ is the scheduling parameter that describes the operation point of DOT wind turbine. The control input is the error $e(t)$ and the control output is a spear position reference value $\hat{s}_{i,\text{ref}}$ with respect to the operation point φ . Therefore, the operation point $\bar{s}_{i,\text{ref}}(\varphi)$ is added to this deviation as

$$s_{i,\text{ref}}(\varphi, t) = \hat{s}_{i,\text{ref}}(\varphi, t) + \bar{s}_{i,\text{ref}}(\varphi). \quad (3-47)$$

The elements of matrices A , B , C and D are linearly interpolated between the controller matrices which are constructed at the specific operation points, described in Section 3-5. To illustrate this for the A matrix e.g., the linear interpolation procedure is described as

$$A_{i,j}(\varphi) = \frac{\varphi - \varphi_{i-1}}{\varphi_i - \varphi_{i-1}}(A_{i,j}(\varphi_i) - A_{i,j}(\varphi_{i-1})) + A_{i,j}(\varphi_{i-1}), \quad (3-48)$$

where $\varphi_{i-1} < \varphi < \varphi_i$. In this case, the scheduling parameter φ is chosen as the rotor rotational speed ω_r .

This chapter presented the control strategy and controller design of the DOT wind turbine. The next chapter presents the results of time-domain simulations and the control performance is evaluated.

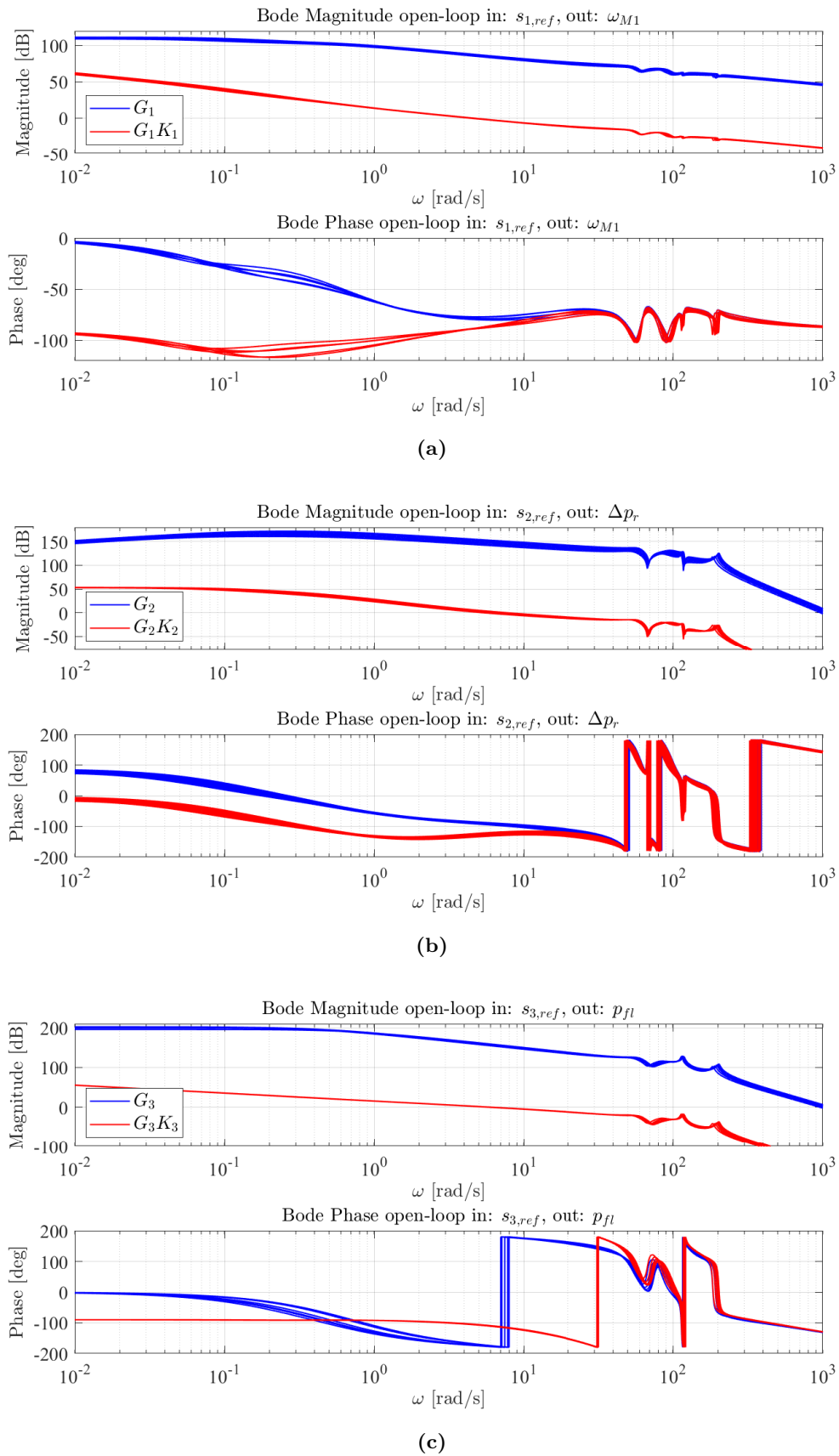


Figure 3-25: For all operation points which are presented in section 3-5, Figures (a), (b) and (c) illustrate the Bode magnitude and phase plots of both G_1 and G_1K_1 , G_2 and G_2K_2 and G_3 and G_3K_3 . For clear visibility, the phase plots are wrapped between -180 deg and 180 deg.



Chapter 4

Control Results & Evaluation

In the previous chapter, a decentralized gain scheduled controller is designed. This chapter presents the results of two different time-domain simulations. In Section 4-1, controller performance is analyzed based on multiple step-responses. Both increasing and decreasing wind step responses are considered. Thereupon, simulation results of a 25 minute simulation with a realistic wind profile are presented in Section 4-2.

4-1:	Time domain step response	72
4-2:	Time domain wind simulation	77

4-1 Time domain step response

This section presents the results of time-domain step-response simulations. First, two different scenarios are described. Thereupon, the control simulation results are presented of both scenarios. Lastly, the controller performance is evaluated.

Before controller behavior is studied for an actual wind signal with realistic turbulence, a couple of step responses are studied first. Formally, knowing the step response of a dynamical system gives information on the stability of such a system, and on its ability to reach one stationary state when starting from another. The step response of a system, given an initial state, consists of the time evolution of its outputs when some input describes a Heaviside step function.

For this step response analysis, two scenarios are considered. Since the dynamic behavior of the DOT wind turbine is slightly different for increasing and decreasing wind speeds, both these cases are covered by the step-response scenarios A and B, respectively. Tables 4-1 and 4-2 give an overview of the eight step-response scenarios that are considered. Wind speed U_r at the rotor is taken as step input. Scenario A starts at a wind speed of 8 m s^{-1} , and knows four step inputs of 0.5 , 1.5 , 2.5 and 3.5 m s^{-1} . Scenario B starts at a wind speed of 11 m s^{-1} , and knows four step inputs of -0.5 , -1.5 , -2.5 and -3.5 m s^{-1} . The step response results of both scenarios A and B are presented in the rest of this section.

Remark: all step-response control simulations are performed with the full non-linear model in the Simulink simulation environment [94].

4-1-1 Results scenario A

The first scenario considers increasing wind step inputs. Four different wind step inputs are studied, specified in Table 4-1. The non-linear model is brought into a steady state condition before the simulation starts at $t = 0$.

Step response nr.	Wind speed U_r at $t < 0$	Wind speed U_r at $t \geq 0$
1	8 m s^{-1}	8.5 m s^{-1}
2	8 m s^{-1}	9.5 m s^{-1}
3	8 m s^{-1}	10.5 m s^{-1}
4	8 m s^{-1}	11.5 m s^{-1}

Table 4-1: Step response scenario A. Four different step inputs, all starting at a wind speed of 8 m s^{-1} and relative step inputs of 0.5 , 1.5 , 2.5 and 3.5 m s^{-1}

Figure 4-1b illustrates the step responses of the rotor speed. All step responses have settling times (the time required for the response curve to reach and stay within a range of 5% of the final value) between 20 and 22 seconds. Figure 4-1c depicts the step responses of the pressure differential Δp_r and the pressure differential reference values $\Delta p_{r,\text{ref}}$. The pressure differential step response is almost identical to the response of the rotor speed, similar to conventional wind turbines.

Figure 4-1d shows the step responses of the feed line pressure p_{fl} . In section 3-4, one of the control specifications mentioned that the feed line pressure needs to stay above atmospheric pressure ($> 1 \text{ bar}$). The figure shows that for positive wind step inputs the

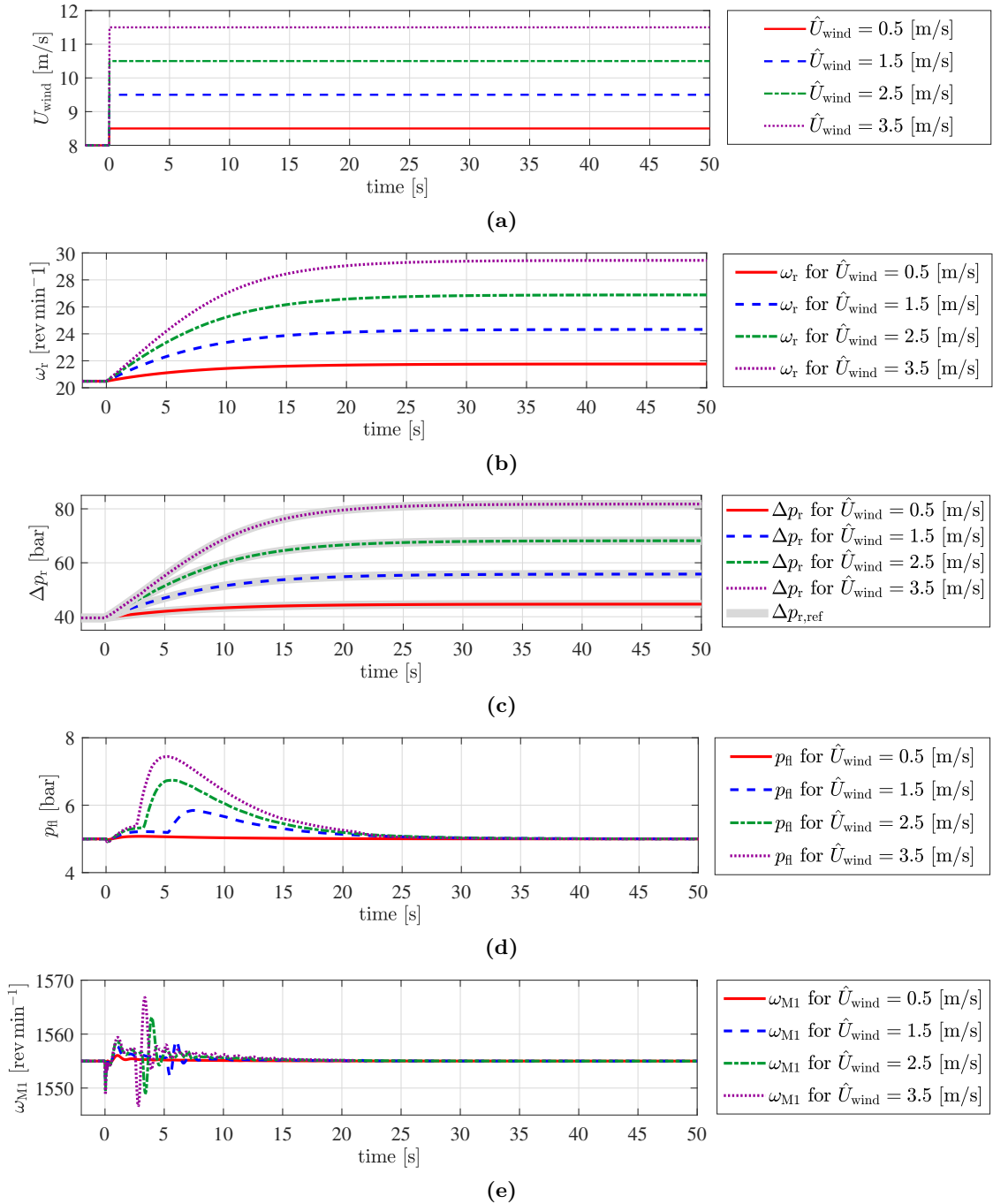


Figure 4-1: Step responses of the increasing wind step inputs as specified in Table 4-1. The step wind inputs are illustrated in Figure (a). Figure (b) illustrates the rotor speed over time. Figure (c) shows the pressure differentials Δp_r across the rotor pump, that has to follow the reference pressure differential. Figure (d) presents the step responses of the feed line pressure p_H which has to stay at 5 bar, and cannot exceed 1 bar. Figure (e) illustrates the step responses of the rotational speed ω_{M1} of the internal water motor.

feed line pressure increases as well. Therefore, this control specification is met. However, a small delay is observed. This is caused by the volumetric efficiency of the pre-pressure pumps, described in Section 2-3-3. Before the step input ($t < 0$), the pre-pressure pumps are operating at a low rotational speed with a discharge pressure of approximately 11 bar. As Figure 2-12 shows, the volumetric efficiency is very low under these conditions, hence the leakage flow is bigger than the discharge flow. Figure 4-2 illustrates this for the step

response of $\hat{U}_{\text{wind}} = 1.5 \text{ m s}^{-1}$. For $t > 0$, the rotational speed of the pre-pressure pumps increases based on the rotor rotational speed. Due to the low efficiency of the pre-pressure pumps, first the leakage flow increases significantly faster with respect to the discharge flow. For higher rotational speeds of the pre-pressure pumps, the volumetric efficiency increases and the discharge flow starts to increase. For this case, the increasing discharge flow becomes notable for $t > 5$, which exactly coincides with the increase of the feed line pressure p_{fl} for $\hat{U}_{\text{wind}} = 1.5 \text{ m s}^{-1}$ illustrated in Figure 4-1d. For the more aggressive step inputs, the delay becomes smaller since the rotor speed, thus the rotational speed of the pre-pressure pumps, increases faster.

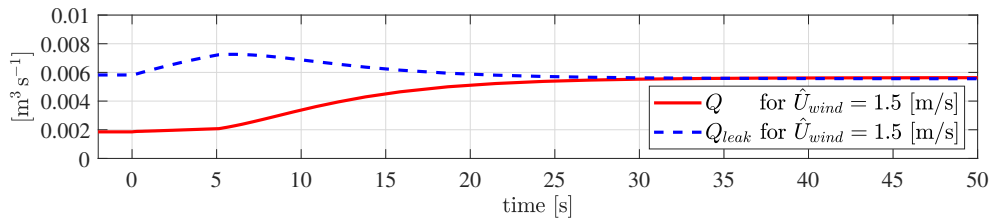


Figure 4-2: Discharge flow Q and leakage flow Q_{leak} of the pre-pressure pumps combined during the step response simulation of $\hat{U}_{\text{wind}} = 1.5 \text{ m s}^{-1}$ illustrated in Figure 4-1d

Lastly, Figure 4-1e illustrates the step responses of the rotational speed ω_{M1} of the internal water motor. Overshoot is encountered here, however, even for the most aggressive step input of $\hat{U}_{\text{wind}} = 3.5 \text{ m s}^{-1}$, this overshoot stays well below 1 %.

It can be concluded that all specifications of Section 3-4 are met for the step responses of scenario A. The subsequent subsection will present the step response results of scenario B.

4-1-2 Results scenario B

Scenario B considers decreasing wind step inputs. Four different wind step inputs are studied, specified in Table 4-2. The non-linear model is brought into a steady state condition before the simulation starts at $t = 0$.

Step response nr.	Wind speed U_r at $t < 0$	Wind speed U_r at $t \geq 0$
1	11 m s^{-1}	10.5 m s^{-1}
2	11 m s^{-1}	9.5 m s^{-1}
3	11 m s^{-1}	8.5 m s^{-1}
4	11 m s^{-1}	7.5 m s^{-1}

Table 4-2: Step response scenario B. Three different step inputs, all starting at a wind speed of 11 m s^{-1} and relative step inputs of -0.5 , -1.5 , -2.5 and -3.5 m s^{-1}

Figure 4-3b illustrates the step responses of the rotor speed. All step responses have settling times (the time required for the response curve to reach and stay within a range of 5% of the final value) between 16.5 and 18.5 seconds. Figure 4-3c depicts the step responses of the pressure differential Δp_r and the pressure differential reference values $\Delta p_{r,\text{ref}}$. The pressure differential step response is almost identical to the response of the rotor speed, similar to conventional wind turbines.

Figure 4-3d illustrates the step responses of the feed line pressure p_{fl} . In this case, the feed line pressure drops for negative wind step inputs. In Section 3-4, one of the control specifications mentioned that the feed line pressure needs to stay above atmospheric pressure (> 1 bar). The step responses show that even for the most aggressive wind step input of $\hat{U}_{\text{wind}} = -3.5 \text{ m s}^{-1}$, the feed line pressure stays well within this boundary.

Lastly, Figure 4-3e illustrates the step responses of the rotational speed ω_{M1} of the internal water motor. Again, overshoot is encountered here, however, even for the most aggressive step input of $\hat{U}_{\text{wind}} = -3.5 \text{ m s}^{-1}$, this overshoot stays well below 1 %.

It can be concluded that all specifications of Section 3-4 are met for the step responses of both scenario A and B. The next section will present the results of time domain simulations performed with a varying wind signal and realistic turbulence.

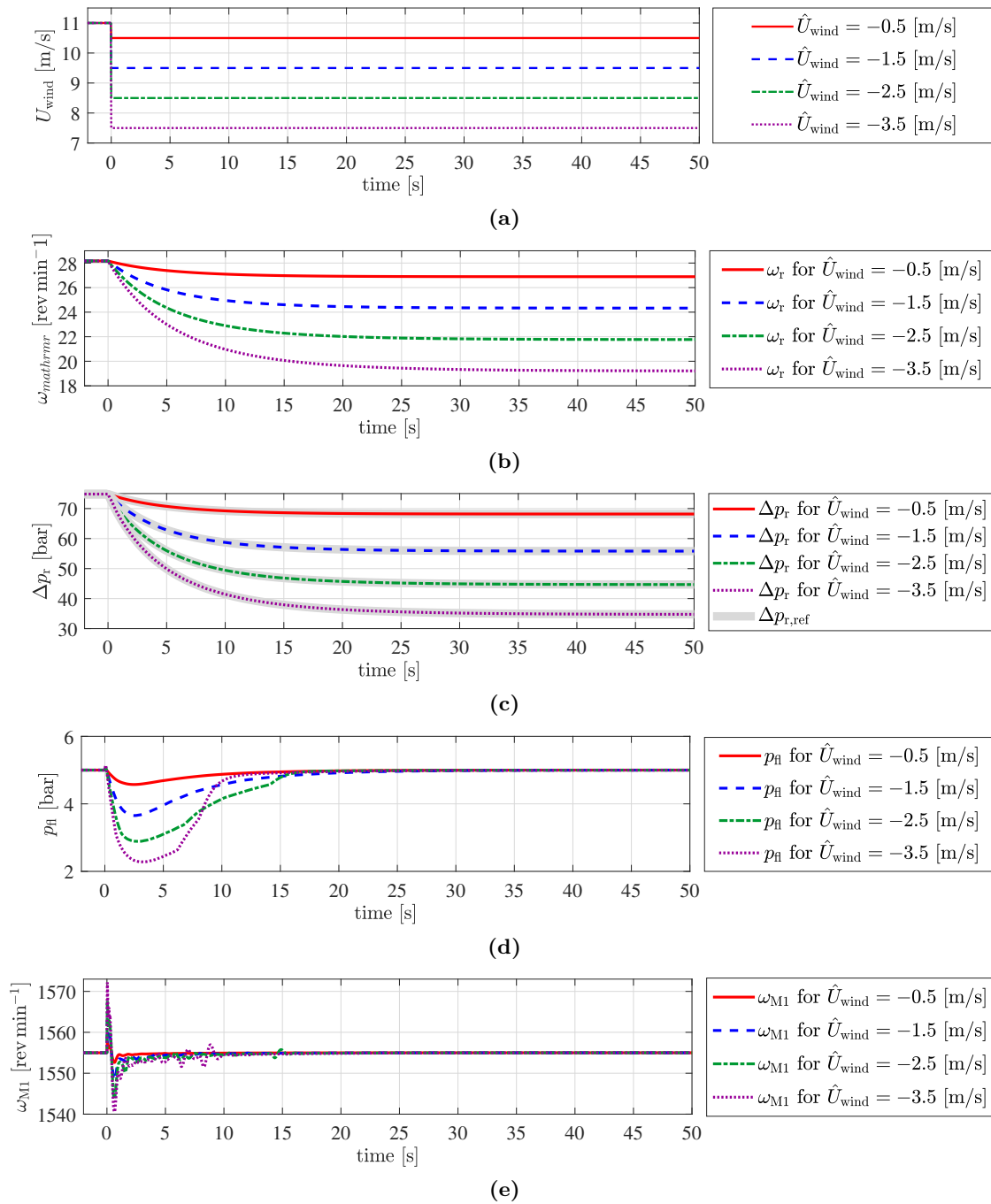


Figure 4-3: Step responses of the increasing wind step inputs as specified in Table 4-1. The step wind input signals are illustrated in Figure (a). Figure (b) illustrates the rotor speed over time. Figure (c) shows the pressure differentials Δp_r across the rotor pump, that has to follow the reference pressure differential. Figure (d) presents the step responses of the feed line pressure p_H which has to stay at 5 bar, and cannot exceed 1 bar. Figure (e) illustrates the step responses of the rotational speed ω_{M1} of the internal water motor.

4-2 Time domain wind simulation

This section presents the results of time-domain simulations with a wind signal with realistic turbulence. After presentation of the control simulations results, the controller performance is evaluated.

A wind signal with realistic turbulence was generated with TurbSim software [93]. This wind signal is illustrated in Figure 4-5a, together with the rotor speed of the DOT wind turbine. Besides stable turbine operation, it is concluded that good tracking of the wind is achieved for operation at $C_{\tau, \max}$. Figure 4-5b illustrates the pressure differential Δp_r across the rotor pump and its reference value $\Delta p_{r, \text{ref}}$ which is determined by the feed forward law based on rotor speed described by Equation 3-4.

As mentioned in Section 3-4, the feed line pressure before the rotor pump has to be regulated to a pressure of 5 bar. In addition to that, the pressure cannot exceed the atmospheric pressure (1 bar). Figure 4-5c shows the result of the time domain simulation, and it is concluded that the control requirements are met.

Another requirement mentioned in Section 3-4 was that the rotational speed of the internal water motor has to be regulated at a constant rotational speed of $1555 \text{ rev min}^{-1}$. Figure 4-5d illustrates the results of the time domain simulation and a satisfactory result is achieved. The rotational speed of the internal water motor stays within a range of 0.64 % of the desired rotational speed. Besides, it was assumed that small deficits in regenerated power, caused by wind fluctuations, do not affect operation of the pre-pressure pumps. In reality, a small safety margin would already account for these fluctuations with a maximum of 0.64 %. However, how big this safety margin should be is left out of the scope of this thesis.

At last, Figure 4-4 illustrates the generator torque demand τ_{M1} (excited on the internal water motor of the regenerative power system) and the rotational speed ω_{pp} of the pre-pressure pumps during the time domain wind simulation. Both the torque τ_{M1} and the rotational speed ω_{pp} are determined by the feed forward relations illustrated in Figure 3-4b, based on the rotational speed of the rotor.

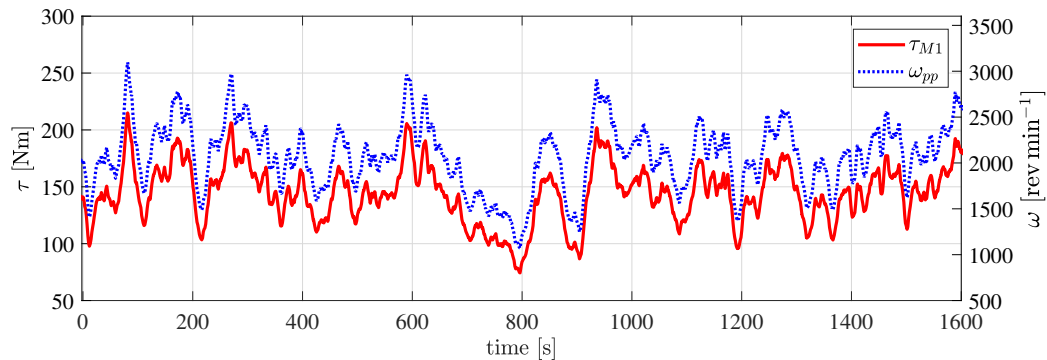


Figure 4-4: The red line indicates the generator torque demand τ_{M1} excited on the internal water motor of the regenerative power system. The blue line indicates the rotational speed ω_{pp} of the pre-pressure pumps. Both are determined by the feed forward relations illustrated in Figure 3-4b, based on the rotational speed of the rotor.

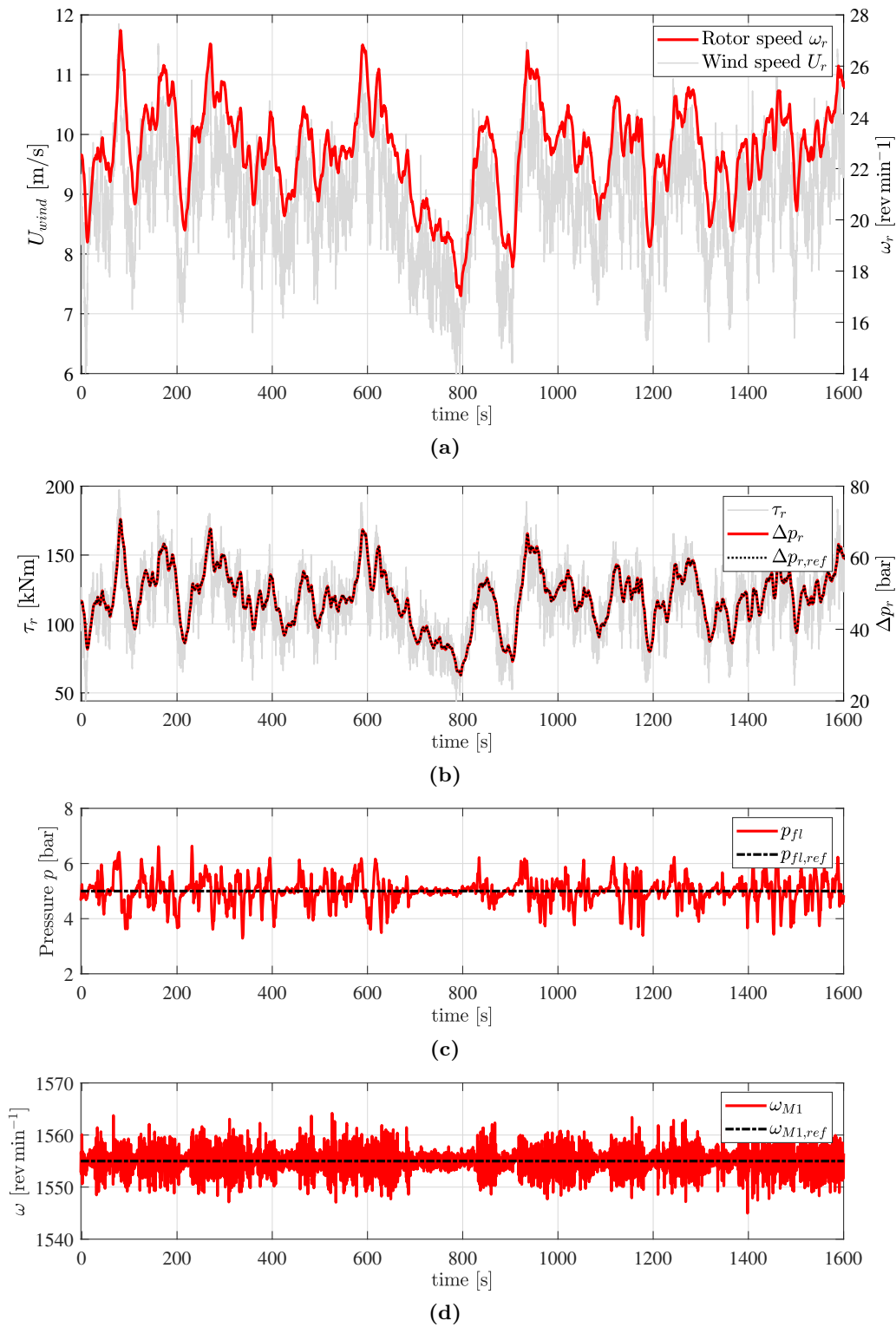


Figure 4-5: Results of the time domain wind simulation where (a) depicts the wind speed U_r and rotational speed ω_r of the rotor; (b) the rotor torque τ_r , the pressure differential Δp_r across the rotor pump and its reference value $\Delta p_{r,ref}$; (c) the feed line pressure p_{fl} right before the rotor pump and its reference value $p_{fl,ref}$; (d) the rotational speed ω_{M1} of the internal water motor and its reference value $\omega_{M1,ref}$.

4-2-1 Actuator limits

Good tracking of the rotor speed is achieved, together with a stable feed line pressure and rotational speed of the internal water motor. However, the control actuators have to be physically able to track the control signals, otherwise, none of the above mentioned makes any sense. In this case, the speed limits of the spears inside the spear valves are restricted. As mentioned in section 2-5, the maximum spear velocity is 0.44 mm s^{-1} , both in opening and closing direction.

Figure 4-6 shows the spear velocities of all three spear valves. The velocity limits are indicated by the black dashed lines. It can be concluded that the spear valves S_1 and S_3 do not come close to these velocity limits. However, spear valve S_2 is operating at the limits of its capabilities, but does not exceed this limit. However, heavier turbulence would ask spear valve S_2 to exceed its limit. Spear valve S_2 is responsible for control of the pressure differential Δp_r across the rotor pump and is therefore the main control actuator for rotor speed control. For that reason, a spear valve with higher velocity limits of the spear would be recommended for spear valve S_2 in order to guarantee stable turbine behavior.

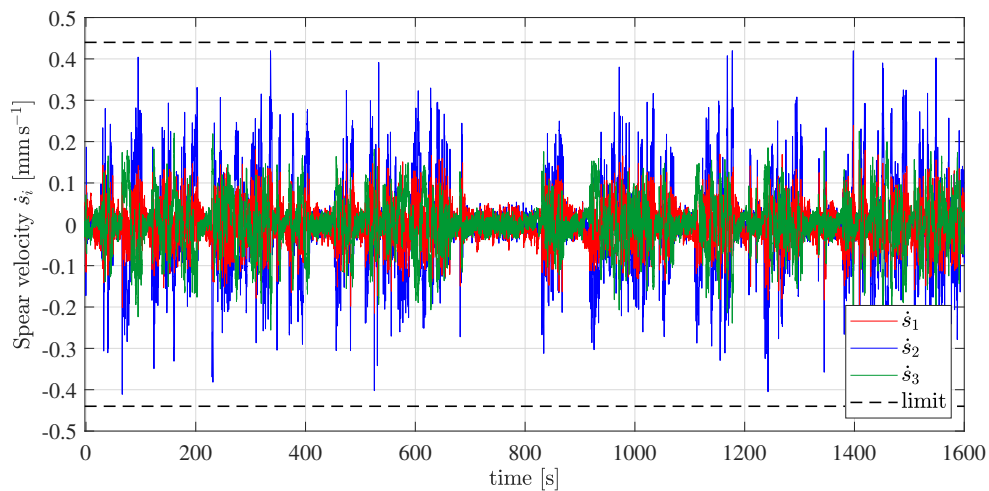


Figure 4-6: Velocities \dot{s}_i of the spears inside all three spear valves. The black dashed lines indicate the speed limits of the spears of 0.44 mm s^{-1} , both in opening and closing direction. The velocities of spear valve S_1 and S_3 do not come close to the limit. However, spear valve S_2 is operating close to its maximum capabilities.



Chapter 5

Conclusions & Recommendations

In Chapter 1 the **motivation** for this thesis was set out through stating the different problems currently encountered in the offshore wind industry. Both the rapidly-growing demand for sustainable power production and the urge towards reducing the Levelized Cost of Energy (LCoE) lead to a notable trend of wind turbines becoming larger over the past decades. Larger rotors result in increased loads affecting components both outside and inside the nacelle. This increases the risk of pre-mature failing of these components, a hassle at offshore locations and a significant contribution to the high turbine life-cycle costs.

Delft Offshore Turbine (DOT) is currently developing a radically new concept, replacing conventional drivetrain components by more robust hydraulic components. Generally, turbine operation in the below-rated operational region is controlled with generator torque control. Since the DOT concept decouples the rotor from the generator however, the **goal** of this thesis was to design a control strategy for the hydraulic DOT wind turbine, incorporating a Regenerative Power System (RPS). For the latter mentioned aspect, a feasibility analysis for self-sustainability had to be performed.

The research performed in this thesis has provided a variety of results and insights which contribute to an understanding of hydraulic turbine control, including regenerating capabilities for self-sustainability. This chapter concludes on these results. After these results are presented, several recommendations for the future are proposed.

5-1 Conclusion

The conclusion is structured similar to the objective statements described in Chapter 1-6. First, the objective is mentioned, after which a brief conclusion follows.

1. *Make a dynamical model of the DOT drivetrain.*

Several turbine and hydraulic components, currently available for implementation in the DOT hydraulic drivetrain, have been analyzed. For the rotor, a simplified first-order dynamic rotor model is used. For the hydraulic pumps and motors, general pump equations are analyzed in the literature and supplemented with efficiency

data obtained from in-field tests or vendor specification sheets of the specific pump in question. For the pipe lines, a dynamical model is developed, incorporating inductance, resistance and capacitance of the seawater flows. The last component that is being used in the DOT drivetrain is the spear valve. As proposed by previous research, a first-order dynamical actuator model is used for movement of the spear inside the spear valve.

The model has been developed and implemented in a specialized hydraulic software package. This system is linearized at multiple operation points of interest for further system analysis and controller design.

2. *Analyze the coupling between the in- and outputs of the complete drivetrain model and make an assessment of the feasibility for a decentralized Single-Input Single-Output (SISO) control solution, or a more advanced centralized Multiple-Input Multiple-Output (MIMO) control algorithm for below-rated operation of the wind turbine.*

The degree of interaction between the various inputs and outputs of the system has been analyzed by means of the Relative Gain Array (RGA). It was concluded that by incorporating the operational speed of the pre-pressure pumps as a feedback control variable, especially the feed line pressure and the pressure differential across the rotor pumps were coupled to multiple control inputs. However, after analysis of the RPS, it was concluded that the operating range of the pre-pressure pumps is very limited due to the limited amount of attainable power regeneration by the RPS. This results in a low drivetrain efficiency and a strict operational path of the pre-pressure pumps to maximize the drivetrain efficiency. Therefore, the system coupling was again analyzed by only considering the spear position reference values of the three spear valves as feedback control variables. In this case, the input-output interaction was found to be satisfactory decoupled, especially in the low frequency domain. This created the potential for decentralized SISO control, using the most optimal input-output pairings according to the RGA.

3. *Based on the physical limitations of the individual components that are currently used in the drivetrain model, describe a feasible control strategy.*

Various control implementations for conventional wind turbines are analyzed in the literature.

Since one of the future goals of Delft Offshore Turbine is to increase the size of its hydraulic wind turbines, it is inevitable that rotor inertia's will increase.

Power generation takes place at a centralized hydro power unit at a considerable distance from one individual wind turbine and increase. Besides that, rotor sizes of future DOT concepts may increase in the foreseeable future. These two reasons invalidated the potential for Power Signal Feedback (PSF) control, the Hill Climb Search (HCS) gradient search algorithm or Extremum Seeking Control (ESC). Therefore, Optimal Torque Control (OTC) is chosen as the foundation of the DOT Maximum Power Point Tracking (MPPT) strategy. This strategy is translated to an Optimal Pressure Control (OPC) strategy, where system torque is now analogous to the pressure differential across the rotor pump. Three spear valves are used to control the rotational speed of the internal water motor that is part of the RPS, the feed line pressure and the pressure differential across the rotor pump.

To facilitate self-sustainability, the pre-pressure pumps are driven with energy re-

generated by the RPS. The maximum power generation of the RPS is limited by the pressure differential between the feed line and the discharge line of the drivetrain. An analysis of the RPS showed that the limited amount of attainable power regeneration, thus limited operational speed of the pre-pressure pumps, is the main factor that contributes to low drivetrain efficiency. To optimize drivetrain efficiency, it was found desirable to operate to rotor at its maximum torque coefficient $C_{\tau, \max}$, resulting in an increased rotor pump discharge pressure. The pre-pressure pumps are operated by feed-forward control, dependent of the rotor speed, thus the amount of power that is available. The spear valves are used for feedback control of the rotational speed of the water motor inside the RPS, the feed line pressure and the pressure differential across the rotor pump.

4. *Design a controller for the below-rated operational domain and evaluate this controller in a high-fidelity simulation environment.*

Based on the optimal input-output pairing, obtained by the RGA analysis, three decentralized SISO controllers are designed. A procedure for H_{∞} fixed-structure controller synthesis was used to tune two Proportional Integral (PI)-controllers and one Proportional Integral Derivative (PID)-controller such that desired target loop shapes were obtained. Because of the non-linear allure of the system, a rotor speed dependent gain-scheduling is implemented for different operation points of the wind turbine such that equal performance is attained throughout the whole below-rated operational domain. Robustness criteria in terms of phase margin, gain margin and modulus margin are met for all operation points.

The controller was evaluated by means of two simulation cases. Simulation results of multiple step inputs and a wind signal input with realistic turbulence showed that all control requirements were met. The actuation speed of the spear valves turned out to be sufficient.

5-2 Recommendations

1. *Rotor to pump transmission and dimensions of the internal water motor.*

It was found that power regeneration with the RPS is limited by the pressure differential across the rotor pump. Since the maximum attainable power regeneration is quite low, the pre-pressure pumps cannot be fully operated in the whole below-rated operational domain. Less flow entering the wind turbine drivetrain results in equally less flow leaving the drivetrain, heading towards the external hydro-power unit. Therefore, very low drivetrain efficiencies were obtained. Being able to fully operate the pre-pressure pumps throughout the complete (or wider range of the) below-rated operational domain would therefore result in higher drivetrain efficiencies.

An analysis showed that drivetrain efficiency would increase significantly by only decreasing the transmission ratio between the rotor and the pump shaft. For operation of the DOT according to the same OPC strategy as presented in this thesis, higher pressure differentials across pump should be attained, together with lower flow rates. Higher pressure differentials across the rotor pump result in the ability of regenerating more electrical power with the RPS. Besides that, a lower seawater flow rate needed by the rotor pump, decreases the need for flow compensation through

the internal spear valve. Implementation of this improvement would result in an enormous increase of drivetrain efficiency. However, a pump being able to handle these high pressures and lower flow rates has to be designed still.

Another possibility is increasing the volumetric displacement of the internal water motor. This allows the pre-pressure pumps to be fully operated over a wider range of rotor speeds. However, the amount of flow that has to be compensated for by the internal spear valve remains equal for turbine operation at full load. Therefore, drivetrain efficiency at full load remains equal, but shows a slightly higher peak halfway of the below-rated operational domain. Accordingly, this is not recommended as a long term solution.

2. *Self-sustainability through power regeneration at centralized hydro-power unit.*

In addition to the previous recommendation, future research could be performed on complete elimination of the RPS inside the wind turbine drivetrain (or at least multiple wind turbines within the wind farm). It could be an option to use the electrical energy, generated by the external hydro-power unit to operate the pre-pressure pumps. Engineering wise, this results in a less complex system due to a smaller amount of hydraulic components per individual wind turbine. Besides that, the pre-pressure pumps could be designed such that they can supply a sufficient flow of seawater for the rotor pump in the whole below-rated operational domain.

3. *Derivation of an analytical drivetrain model.*

Since almost no literature currently elaborates on the modeling of hydraulic networks comparable to the DOT hydraulic drivetrain, it was found to difficult to derive an analytical dynamical drivetrain model. Therefore, a high-fidelity modeling environment was used for this purpose instead. Future research could be done on derivation of such a model.

Appendix A

Appendix A

A-1 Particle Swarm Optimization

The Particle Swarm Optimization (PSO) algorithm is a population based stochastic optimization technique developed by Eberhart & Kennedy in 1995, inspired by social behavior of bird flocking or fish schooling.

PSO shares many similarities with evolutionary techniques such as Genetic Algorithms (GA). The system is initialized with a population of random solutions and searches for optima by updating generations. However, unlike GA, PSO has no evolution operators such as crossover and mutation. In PSO, the potential solutions, called particles, fly through the problem space by following the current optimum particles.

Each particle keeps track of its coordinates in the search space which are associated with the best solution (fitness) it has achieved so far itself. (The fitness value is also stored.) This value is called *pbest* (particle's best). Another "best" value that is tracked by the particle swarm optimizer is the best value, obtained so far by any particle in the neighbors of the particle. This location is called *lbest* (local best). However, when a particle takes the total population as its topological neighbors, the best value is a global best and is called *gbest*.

The PSO concept consists of, at each time step, changing the velocity of each particle toward its *pbest* and *lbest* locations (local version of PSO, otherwise *gbest*). Acceleration is weighted by a random term, with separate random numbers being generated for acceleration toward *pbest* and *lbest* locations.

Code box A.1 on the next page shows the pseudo code of the PSO algorithm. During the initialization, the particles are assigned random initial positions and they change their position iteratively to reach the global optimal solution. The direction of position change is influenced by both particle's own experience and the knowledge the particle acquires from the flock. Each particle is evaluated using a fitness function, which indicates how close the particle is to the optimal solution. A particle i has a memory to store the knowledge of position $pbest_{id}$, which is defined as the position at which the particle had best fitness. Besides, the best of $pbest_{id}$ of all particles, called $gbest_d$, is stored too. At each iteration

k , PSO modifies each dimension of the position x_{id} in a particle by adding a velocity v_{id} and moves the particle towards its $pbest_{id}$ and $gbest_d$ using Equations A-1 and A-2.

$$v_{id}(k+1) = w \cdot v_{id}(k) + c_1 rand_1(p_{id} - x_{id}) + c_2 rand_2(p_{gd} - x_{id}) \quad (A-1)$$

$$x_{id}(k+1) = x_{id}(k) + v_{id}(k+1) \quad (A-2)$$

where v_{id} and x_{id} are the respective velocity and position of particle i in direction of dimension d . Furthermore, p_{id} is the position of particle i with fitness value $pbest_{id}$, and p_{gd} is the position of particle i with fitness value $gbest_{id}$.

The coefficients w , c_1 and c_2 represent the particle's inertia, the 'Self-Adjustment-Weight' and the 'Social-Adjustment-Weight'. The self-adjustment-weight c_1 makes the particle head more toward the best place it has visited in the past. The social-adjustment-weight c_2 makes the particle head more toward the best place, known in the current neighborhood. The vectors $rand_1$ and $rand_2$ are randomly (0,1) uniformly distributed vectors with length d . The

In the Optimization Toolbox [49] of MATLAB [94], the default values of these weights were used, as proposed by Pedersen [50] and Mezura-Montes et al. [48].

```

FOR each particle  $i$ 
  FOR each dimension  $d$ 
    Initialize position  $x_{id}$  randomly within permissible range
    Initialize velocity  $v_{id}$  randomly within permissible range
  END FOR
END FOR

Iteration  $k=1$  DO

  FOR each particle  $i$ 
    Calculate fitness value
    IF the fitness value is better than  $pbest_{id}$  in history
      Set current fitness value as the  $pbest_{id}$ 
    END IF
  END FOR

  Choose the particle having the best fitness value as the  $gbest_d$ 

  FOR each particle  $i$ 
    FOR each dimension  $d$ 
      Calculate velocity according to the equation
       $v_{id}(k+1) = wv_{id}(k) + c_1rand_1(p_{id} - x_{id}) + c_2rand_2(p_{gd} - x_{id})$ 
      Update particle position according to the equation
       $x_{id}(k+1) = x_{id}(k) + v_{id}(k+1)$ 
    END FOR
  END FOR

   $k = k + 1$ 
WHILE maximum iterations or minimum error criteria are not attained

```

Code Box A.1: Particle Swarm Optimization (PSO) algorithm represented as pseudo code. Since the code is represented as pseudo code, the code describes itself.

A-2 Simplified SimScape model for Simulink

Figure A-2 showcases a simplified version of the SimScape model used for this thesis. Only the SimScape component blocks are presented. All components are located in a similar fashion compared to all other drivetrain schematics in this thesis report. All blocks are described in Section 2-6, except for those illustrated in Figure A-1.

Figure A-1a illustrates the 'Solve Configuration'-block and is needed to solve the SimScape specific differential equations. Figure A-1b illustrates the 'Hydraulic Fluid'-block which is used for defining hydraulic fluid characteristics. Figure A-1c illustrates the 'PS-Simulink Converter'-block which allows SimScape components blocks to communicate towards conventional Simulink blocks. Figure A-1d illustrates the 'Simulink-PS Converter'-block which allows conventional Simulink blocks to communicate towards SimScape component blocks.

Furthermore, rotor pump P_r communicates with the rotor model (Section 2-2) by means of the pressure differential across the rotor pump and its rotational speed. The position input ports S of all three spear valves communicate with the transfer function outputs s_i , as described in Section 2-5. Rotational motions of the rotor pump P_r and pre-pressure pump P_{pp} are measured with respect to the green 'Mechanical rotational reference'-blocks, described in Section 2-6. The torque excited on the internal water motor M_1 is relative with respect to such a 'Mechanical rotational reference'-block as well, described in Section 2-6. Pressure sensors measure the pressure relative compared to the 'Hydraulic reference'-blocks (atmospheric pressure), described in Section 2-6.

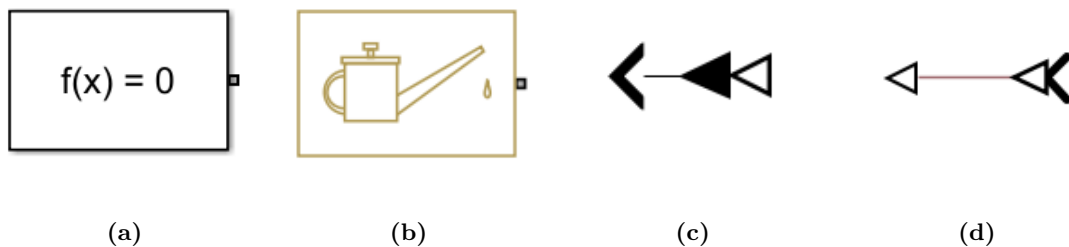


Figure A-1: (a) illustrates the 'Solve Configuration'-block and is needed to solve the SimScape specific differential equations. (b) illustrates the 'Hydraulic Fluid'-block which is used for defining hydraulic fluid characteristics. (c) illustrates the 'PS-Simulink Converter'-block which allows SimScape components blocks to communicate towards conventional Simulink blocks. (d) illustrates the 'Simulink-PS Converter'-block which allows conventional Simulink blocks to communicate towards SimScape component blocks.

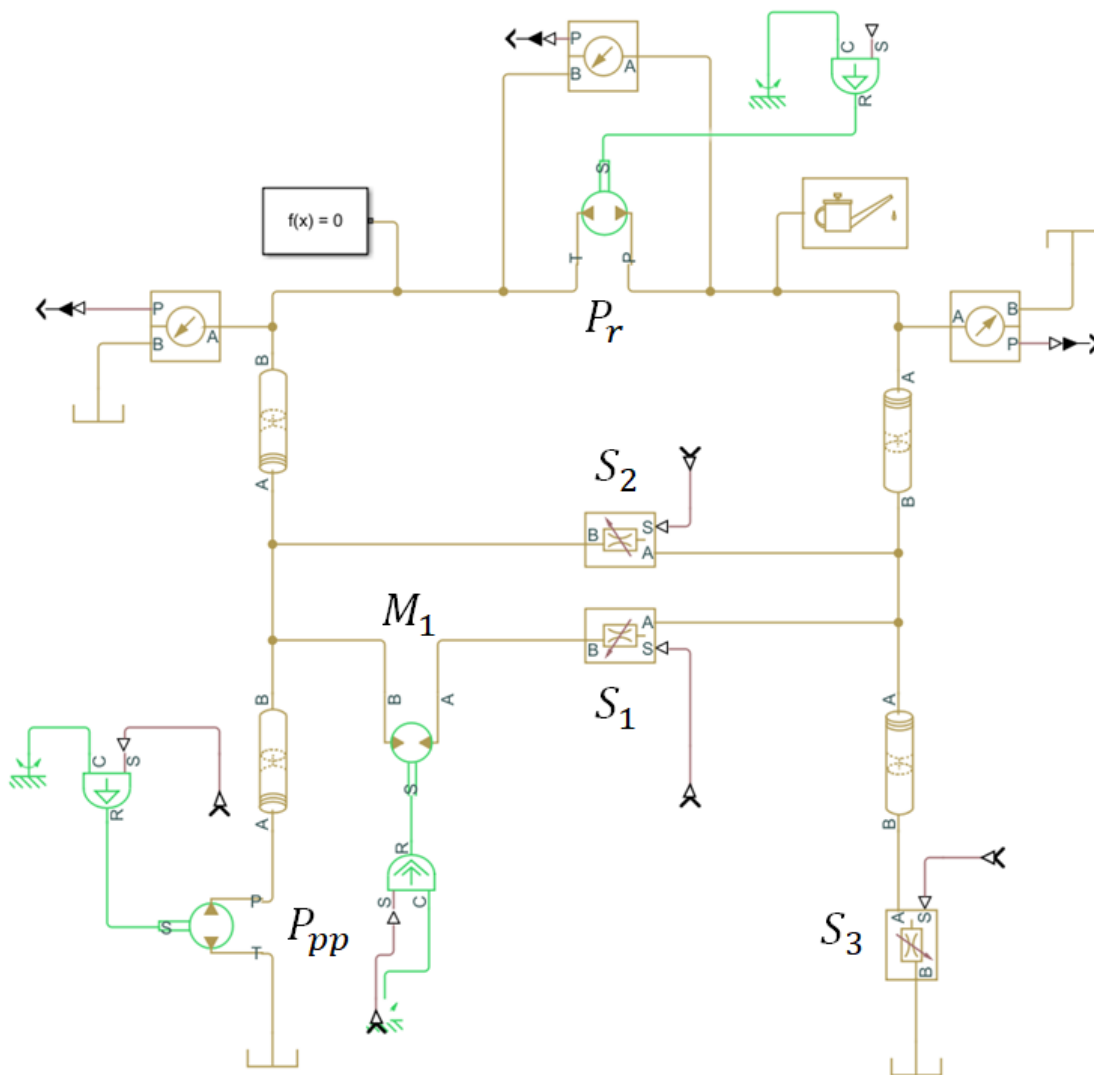


Figure A-2: Simplified version of the SimScape drivetrain model used for this thesis. Only the SimScape component blocks are presented. Rotor pump P_r communicates with the rotor model (Section 2-2) by means of the pressure differential across the rotor pump and its rotational speed. The position input ports S of all three spool valves communicate with the transfer function outputs s_i , as described in Section 2-5. Rotational motions of the rotor pump P_r and pre-pressure pump P_{pp} are measured with respect to the green 'Mechanical rotational reference'-blocks, described in Section 2-6. The torque excited on the internal water motor M_1 is relative with respect to such a 'Mechanical rotational reference'-block as well, described in Section 2-6. Pressure sensors measure the pressure relative compared to the 'Hydraulic reference'-blocks (atmospheric pressure), described in Section 2-6.

Glossary

List of Acronyms

BEM	Blade Element Momentum
CPC	Collective Pitch Control
DDP	Digital Displacement Pump
DOT	Delft Offshore Turbine
ESC	Extremum Seeking Control
GA	Genetic Algorithms
HAWT	Horizontal-axis wind turbine
HCS	Hill Climb Search
LCoE	Levelized Cost of Energy
LPV	Linear Parameter-Varying
LQR	Linear Quadratic Regulator
LTI	Linear Time Invariant
LWK	Landwirtschaftskammer
MIMO	Multiple-Input Multiple-Output
MPPT	Maximum Power Point Tracking
MSE	Mean Squared Error
OPC	Optimal Pressure Control
OTC	Optimal Torque Control
P&O	Perturb and Observe
PI	Proportional Integral
PID	Proportional Integral Derivative
PSF	Power Signal Feedback

PSO	Particle Swarm Optimization
RGA	Relative Gain Array
RPS	Regenerative Power System
SCE	Southern California Edison
SISO	Single-Input Single-Output
SPG	Super Positioned Gear
TSR	Tip-Speed Ratio
WEG	Wind Energy Group
WMEP	Wissenschaftliches Mess- und Evaluierungsprogramm

Bibliography

- [1] F. Spinato, P.J. Tavner, G.J.W. van Bussel, E. Koutoulakos, *Reliability of Wind Turbine Subassemblies*, IET Renewable Power Generation Group, Vol. 3, Iss. 4, pp. 387-401, 2008
- [2] A. Ragheb, M. Ragheb, *Wind Turbine Gearbox Technologies*, Nuclear & Renewable Energy Conference (INREC), 2010 1st International, pp. 1-8, IEEE, 2010
- [3] L.Y. Pao, K.E. Johnson, *Control of Wind Turbines, approached, challenges and recent developments*, IEEE Control Systems Magazine, 16 March, 2011
- [4] T. Burton, N. Jenkins, E. Bossanyi, *Wind Energy Handbook*, John Wiley & Sons, 2011
- [5] M.N. Kotzalas, G.L. Doll, *Tribological advancements for reliable wind turbine performance*, Philosophical Transactions of the Royal Society A, 2010
- [6] C.J. Crabtree, D. Zappala, S.I. Hogg, *Wind energy: UK experiences and offshore operational challenges*, Journal of Power and Energy, Vol. 229(7), pp. 727-746, 2015
- [7] J.K. Lee, J.Y. Park, K.Y. Oh, S.H. Ju, J.S. Lee, *Transformation algorithm of wind turbine blade moment signals for blade condition monitoring*, Renewable energy 79, 209-218, 2015
- [8] L. Fingersh, M. Hand, A. Laxson, *Wind Turbine Design Cost and Scaling Model*, Technical Report, NREL, 2006
- [9] N.F.B. Diepeveen, *On the Application of Fluid Power Transmission in Offshore Wind Turbines*, PhD thesis, Delft University of Technology, 2013.
- [10] H. Polinder, A. Abrahamsen, K. Atallah, *Trends in Wind Turbine Generator Systems*, IEEE Journal of emerging and selected topics in power electronics, Vol.1, No.3, September 2013
- [11] E. Hau, *Wind Turbines. Fundamentals, Technologies, Application, Economics*, Third, translated edition, 2013.

- [12] Website Wind Energie Nieuws, *Siemens - Gamesa concentreert zich offshore op direct-drive windturbines*, <https://www.windenergie-nieuws.nl/15/siemens-gamesa-concentreert-zich-offshore-op-direct-drive-windturbines/>, January 2018
- [13] H.E. Merrit, *Hydraulic control systems*, John Wiley & Sons, 1967
- [14] B. Nesbitt, *Handbook of pumps and pumping: Pumping manual international*, Elsevier, 2006
- [15] C. Ai, W. Bai, Y. Zhang, X.D. Kong, *Active Control of Pressure Resonance in Long Pipeline of Bottom Founded Hydraulic Wind Turbines Based on Multi-Objective Genetic Algorithm*, IEEE Access, October 2018
- [16] S. Rybak, *Description of the 3MW SWT-3 Wind Turbine at San Geronio Pass, California*, technical report, The Bendix Corporation Energy, Environment and Technology Office, 1982
- [17] E. Hau, J. Langenbrinck, W. Palz, *Large Wind Turbines*, Springer-Verlag Berlin Heidelberg GmbH, ISBN: 978-3-642-52129-4, 1993
- [18] R.J. Hicks, F. Cunliffe, U. Giger, *Optimized Gearbox Design for Modern Wind Turbines*, European Wind Energy Conference and Exhibition (EWEC 2004), pp. 1-8, 2004
- [19] H. Müller, M. Pöller, A. Basteck, M. Tilscher, J. Pfister, *Grid Compatibility of Variable Speed Wind Turbines with Directly Coupled Synchronous Generator and Hydro-Dynamically Controlled Gearbox* Sixth International Workshop on Large-Scale Integration of Wind Power and Transmission Networks for Offshore Wind Farms, Delft University of Technology, Delft, the Netherlands, 307–315, 2006
- [20] L. Pengfei, W. Wang, *Principle, structure and application of advanced hydrodynamic converted variable speed planetary gear (Vorecon and WinDrive) for industrial drive and wind power transmission*, Sinopec Engineering Incorporation Beijing, China, 2011
- [21] P. Chapple, O. Dahlhaug, P. Haarberg, *Turbine driven electric power production system and a method for control thereof*, Patent US007863767B2, 2011
- [22] K.E. Thomsen, O. Dahlhaug, M. Niss, S. Haugset, *Technological advances in hydraulic drive trains for wind turbines*, Energy Procedia 24, 76-82, 2012
- [23] B. Skaare, B. Hörnsten, F.G. Nielsen, *Modeling, simulation and control of a wind turbine with a hydraulic transmission system*, Wind Energy, 16, pp. 1259-1276, 2012
- [24] D. Buhagiar, T. Sant, M. Bugeja, *A Comparison of Two Pressure Control Concepts for Hydraulic Offshore Wind Turbines*, Journal of Dynamic Systems, Measurement, and Control, ASME, 2016
- [25] W. Rampen, *Gearless transmissions of large wind turbines - The history and future of hydraulic drives*, Artemis IP Ltd, Midlothian, UK, 2006
- [26] , Artemis Intelligent Power, <http://www.artemisip.com/sectors/wind/>, November 2018

- [27] M. Sasaki, A. Yuge, T. Hayashi, H. Nishimo, M. Uchida, T. Noguchi, *Large Capacity Hydrostatic Transmission with Variable Displacement*, 9th International Fluid Power Conference, Vol. 9, RWTH Aachen University, Aachen, Germany, 2014
- [28] S.P. Mulders, N.F.B. Diepeveen, J.-W. van Wingerden, *Control design, implementation and evaluation for an in-field 500kW wind turbine with a fixed-displacement hydraulic drivetrain*, September, 2018.
- [29] J. van der Tempel, *Systeem en werkwijze voor energiewinning*, Octrooicentrum Nederland, aanvraagnummer: 2001663, February 2010.
- [30] A. Pusha, M. Deldar, A. Izadian, *Efficiency Analysis of Hydraulic Wind Power Transfer System*, 2013
- [31] S.P. Mulders, N.F.B. Diepeveen, J.W. van Wingerden, *Control and system design of a regenerative power loop for the hydraulic DOT500 wind turbine*, 2017
- [32] B. Dolan, H. Aschermann, *Control of a Wind Turbine with Hydrostatic Transmission - an Extended Linearisation approach*, University of Rostock, Germany, 2012
- [33] , M. Vaezi, A. Izadian, *Control of a Hydraulic Wind Power Transfer System under Disturbances*, 3rd International Conference on Renewable Energy Research and Applications, October 2014
- [34] F.D. Bianchi, R.S. Sánchez-Peña, M. Guadayol *Gain scheduled control based on high fidelity local wind turbine models*, Renewable Energy 37 2012.
- [35] *Quituplex Plunger Pump K80000-5G* <https://www.kamat.de/en/plunger-pumps/k-80000-5g.html>
- [36] JANUS MOTORS, The Water Hydraulics Co. Ltd., Vendor Specification sheet.
- [37] Pleuger Water Solutions, The source of every solution *Pompen en onderwatermotoren*, Brochure
- [38] *Vestas V44* <https://en.wind-turbine-models.com/turbines/272-vestas-v44>
- [39] R.F. Mikkelsen, J.N. Sørensen, *Actuator Disc Methods Applied to Wind Turbines*, (MEK-FM-PHD; No. 2003-02), 2004
- [40] J.F. Manwell, J.G. McGowan, A.L. Rogers. *Wind Energy Explained - Theory, Design and Application*, John Wiley & Sons Ltd. ISBNs: 0-471-49972-2 (Hardback); 0-470-84612-7 (Electronic), 2002
- [41] R.E. Wilson, P.B.S. Lissaman, S.N. Walker, *Aerodynamic Performance of Wind Turbines*, National Renewable Energy Laboratory, 1976
- [42] F.D. Bianchi, H. Battista, R.J. Mantz, *Wind Turbine Control Systems. Principles, Modelling and Gain Scheduling Design*, Springer Science & Business Media, 2007.
- [43] S.P. Mulders, N.F.B. Diepeveen, J.-W. van Wingerden, Data set: *Control design, implementation and evaluation for an in-field 500kW wind turbine with a fixed-displacement hydraulic drivetrain*, <https://doi.org/10.5281/zenodo.1405387>, 2018

- [44] W. Leithead, B. Connor, *Control of variable speed wind turbines design task*, International Journal of Control 73(13), 1198-1212, 2000
- [45] A.G. Rodriguez, A.G. Rodriguez, M.B. Payán, *Estimating Wind Turbine Mechanical Constants*, Proc. Int. Conf. Renewable Energies and Power Quality (CREPQ'07), pp. 27-30, 2007
- [46] S. Jager, *Control Design and Data-Driven Parameter Optimization for the DOT500 Hydraulic Wind Turbine*, Master Thesis, Delft University of Technology, 2017
- [47] J. Kennedy, R. Eberhart, *Particle Swarm Optimization*, Proceedings of the IEEE International Conference on Neural Networks, Perth, Australia, pp. 1942-1945, 1995
- [48] E. Mezura-Montes, C.A. Coello Coello, *Constraint-handling in nature-inspired numerical optimization: Past, present and future*, Swarm and Evolutionary Computation, pp. 173-194, 2011
- [49] Optimization Toolbox, MATLAB 2018b, Mathworks, <https://nl.mathworks.com/products/optimization.html>
- [50] M.E. Pedersen, *Good Parameters for Particle Swarm Optimization*, Luxembourg: Hvass Laboratories, 2010
- [51] H. Brekke, *Hydraulic Turbines - Design, Erection and Operation*, June 2001
- [52] J.A. Laguna, *Centralized electricity generation in offshore wind farms using hydraulic networks*, PhD thesis, Technical University of Delft, 2017
- [53] S. Skogestad, I. Postlethwaite, *Multivariable Feedback Control - Analysis and Design*, 2nd Edition, John Wiley & Sons, August 2001
- [54] E.W.E. Association, S. Krohn, P.E. Morthorst, S. Awerbuch, *The Economics of Wind Energy: A report of European Wind Energy Association*, EWEA, March 2009
- [55] F.M. White, *Fluid Mechanics, 7th Edition*, McGraw-Hill, New York, 2011.
- [56] F.M. White, *Viscous Fluid Flow*, McGraw-Hill, New York, 1991.
- [57] S. Bragg, *Effect of compressibility on the discharge coefficient of orifices and convergent nozzles*, Journal of Mechanical Engineering 2 (1) 35-44, 1960.
- [58] G.F. Franklin, J.D. Powell, A. Emami-Naeini, *Feedback Control of Dynamic Systems*, Seventh Edition, Pearson, August 2014
- [59] J.Schmitz, M. Vukovic, H. Murrenhoff, *Hydrostatic Transmission for Wind Turbines - An Old Concept, New Dynamics*, RWTH Aachen University, ASME, October 2013
- [60] H. Murrenhoff, *Grundlagen der Fluid, Teil 1: Hydraulik*, Institut für fluidtechnische Antriebe und Steuerungen, RWTH Aachen University, 2016
- [61] A. Akers, M. Grassman, R. Smith, *Hydraulic power system analysis*, CRC press, 2006
- [62] R.K. Bansal, *A Text Book of Fluid Mechanics and Hydraulic Machines, SI Units*, 10th Edition, LAXMI Publications (P) Ltd., New Delhi, 2010

- [63] S.E. Haaland, *Simple and Explicit Formulas for the Friction Factor in Turbulent Pipe Flow*, J. Fluids Eng., pp. 89-90, March 1983
- [64] M.R. Harris, *Orifice Plates and Venture Tubes*, Springer, Experimental Fluid Dynamics, Switzerland, 2015
- [65] F. Spinato, *The Reliability of Wind Turbines*, Energy Group, Durham University, England, Thesis presented for the degree of Doctor of Philosophy, 2008
- [66] The WindPower, Wind Energy Market Intelligence, website, https://www.thewindpower.net/turbine_en_570_wikov_w2000-86.php, May 2018
- [67] H. Schulte, S. Georg, *Nonlinear Control of Wind Turbines with Hydrostatic Transmission Based on Takagi-Sugeno Model*, Journal of Physics: Conference Series 524, 2014
- [68] D. Rajabhandharaks, P. Hsu, *Optimal Aerodynamic Energy Capture Strategies for Hydrostatic Transmission Wind Turbine*, IEEE Conference on Technologies for Sustainability (SusTech), 2014
- [69] Dr. H. Schlichting, *Boundary-Layer Theory*, McGraw-Hill series in Mechanical Engineering, 1979
- [70] , A. Kempenaar, *A small scale Fluid Power Transmission for the Delft Offshore Turbine*, Master Thesis, TU Delft, 2012
- [71] H. HosseinNia, N. Saikumar Lecture slides on *Motion Control I*, Course ME46085, Delft Center of Systems and Control, TU Delft, 2016
- [72] The Engineering Toolbox Website, https://www.engineeringtoolbox.com/bulk-modulus-elasticity-d_585.html, 2017
- [73] D. Milborrow, *Breaking down the cost of wind turbine maintenance*, Web page, <https://www.windpowermonthly.com/article/1010136/breaking-down-cost-wind-turbine-maintenance>, 2010
- [74] Y. Xiao, Y. Li, M.A. Rotea, *Experimental Evaluation of Extremum Seeking Based Region-2 Controller for CART3 Wind Turbine*, AIAA SciTech Forum, 34th Wind Energy Symposium, San Diego, 2016
- [75] S.S. Sheng, W. Yang, *Wind Turbine Drivetrain Condition Monitoring*, National Renewable Energy Laboratory (NREL), ASME Turbo Expo, 2013
- [76] Web page on *Future Energy Industry Trends*, <https://northsearegion.eu/northsee/e-energy/future-energy-industry-trends/>, January 2019
- [77] I.G.P. Rodriguez, *Hydraulic drivetrains for wind turbines*, Msc thesis, Delft University of Technology, 2012
- [78] E.A. Bossanyi, *The Design of Closed Loop Controllers for Wind Turbines*, Wind Energy, 3:149-163, 2000
- [79] A.V. Akkaya, *Effect of bulk modulus on performance of a hydrostatic transmission control system*, Sādhanā Academy Proceedings in Engineering Sciences, vol. 31:p.543 – 556, October 2006.

- [80] A.J.N. Menezes, A.M. Araujo, N.S.B. de Silva, *A review on wind turbine control and its associated methods* Journal of cleaner Production 174, 945-953, 2018
- [81] M. Cheng, Y. Zhu, *The state of the art wind energy conversion system and technologies: A review*, Energy Conversion and Management 88 332-347, 2014
- [82] N. Manring, *Hydraulic control systems*, John Wiley & Sons, 2005
- [83] D. Wang, D. Tan, L. Liu, *Particle swarm optimization algorithm: an overview*, Springer, Soft Comput No. 22, pp. 387-408, 2017
- [84] W.E. Wilson, *Positive-displacement pumps and fluid motors*, Pitman Publishing Corporation, 1950
- [85] R. Datta, V.T. Ranganathan, *A Method of Tracking the Peak Power Points for a Variable Speed Wind Energy Conversion System*, IEEE Transactions of Energy Conversion, Vol. 18, No.1, March 2003
- [86] M.A. Abdullah, A.H.M Yatim, R. Saidur, *A review of maximum power point tracking algorithms for wind energy systems*, Renewable and Sustainable Energy Reviews 16 3220-3227, 2012
- [87] J. Yaoqin, Y. Zhongqing, C. Binggang, *A New Maximum Power Point Tracking Control Scheme for Wind Generation*, Proceedings. International Conference on Power System Technology, 2002
- [88] W.E Wilson, *Mathematical Models in Fluid Power Engineering, Hydraulic & Pneumatic Power*, 1967
- [89] W.M.J. Schlösser, *Ein mathematisches Modell für Verdrängerpumpen und motoren, Ölhydraulik und Pneumatik*, volume vol. 4/5, 1961
- [90] K.E. Rydberg, *Efficiencies for variable hydraulics pumps and motors- Mathematical models and operation conditions*, Linköpings University, Department of Management and Engineering, 2009
- [91] E. Trostmann, *Water Hydraulics Control Technology*, Technical University of Denmark, Lyngby, Denmark 1996.
- [92] T. Keviczky, Lecture slides on *Digital Control (SC42095)*, Delft Center for Systems and Control (DCSC), Technical University Delft, November 2016
- [93] N. Kelley, B. Jonkman, *NWTC Information Portal (TurbSim)*, Webpage: <https://nwtc.nrel.gov/TurbSim>, National Wind Technology Center, Last modified 14-June-2016 ; Accessed 22-April-2019
- [94] Mathworks Matlab R2018b for Windows, URL: <https://nl.mathworks.com/products/matlab.html>
- [95] Mathworks Matlab Simscape Toolbox, URL: <https://nl.mathworks.com/products/simscape.html>
- [96] MathWorks webpage about H_∞ tuning of fixed-structure controllers, <https://nl.mathworks.com/help/robust/ref/hinfstruct.html>

-
- [97] Table for surface roughness heights, URL: https://www.engineeringtoolbox.com/surface-roughness-ventilation-ducts-d_209.html
- [98] ECN webpage on '*Synthetic jets*' against fatigue <https://www.ecn.nl/nl/nieuws/newsletter-en/2010/june-2010/turbine-blades-less-fatigue/>

